

---

# Convective instability changes and tropical cyclone intensification

Seol Eun Shin

---

Dissertation  
at the Faculty of Physics  
Ludwig–Maximilians–University  
Munich

by  
Seol Eun Shin  
from Mokpo

Munich, 11 June 2007

First Examiner: Prof. Dr. Roger K. Smith  
Second Examiner: Prof. Dr. Olaf Krüger  
Date of the oral examination: 27 July 2007

# Kurzfassung

Der Einfluss von Trögen der oberen Troposphäre auf konvektive Instabilität wurde mit Hilfe von Analysen, die auf Gitterdaten des Datenarchivs des Europäischen Zentrums für mittelfristige Wettervorhersage (EZMW) basieren, untersucht. Als Maß der Instabilität wurde die sogenannte „Convective Available Potential Energy“ (CAPE) verwendet. Eine Fallstudie des *Burdekin Thunderstorm* in Australien (Januar 2001) zeigte, dass die hohe CAPE vor der Entwicklung des Gewitters von kalter Luft, die mit Trögen in Zusammenhang steht, beeinflusst wurde. Im Gegensatz dazu war in den Fällen der Australischen Tropischen Zyklone *Theodore* (Februar 1994) und *Rewa* (Januar 1994) der Einfluss der Tröge auf die CAPE minimal, wobei die Abkühlung schwächer als in dem Fall des Gewitters war.

Die Intensivierung tropischer Wirbelstürme wurde mit Hilfe von numerischen Modellrechnungen, die von der Fallstudie motiviert wurden, weiter erforscht. Ergebnisse aus einer Kontroll-Modellrechnung zeigen, dass die Intensivierung ein eigentlich nicht axial-symmetrischer Prozess ist. Kumuluskonvektion bildet sich vornehmlich in der Nähe des Radius der maximalen Windgeschwindigkeit des initialen Wirbels. Diese konvektive Zellen weisen erhöhte Rotation auf und werden daher Meso-Wirbel genannt. Die Entstehung der Meso-Wirbel ist abhängig von der CAPE, die mit Grenzschichtfeuchte verbunden ist, die wegen des Feuchteausstausches zwischen Luft und Meer bei hoher Windgeschwindigkeit zunimmt. Dennoch ist die weitere Intensivierung des Wirbelsturms als Ganzes unabhängig von der CAPE. Der wichtigste Prozess hierbei ist die Verschmelzung der Wirbel, wodurch sich der Wirbelsturm rasch verstärkt. In der Folge wurden Ensembleberechnungen mit zufälligen Störungen der Anfangsfeuchte in der unteren Troposphäre durchgeführt, um die Sensitivität der asymmetrischen Intensivierung bezüglich der Feuchte zu erforschen. Es war zu beobachten, dass die Entstehung und Verschmelzung der Meso-Wirbel von zufälligen Störungen beeinflusst wurde, wogegen sich die Intensität des vollentwickelten Wirbelsturms im Bereich der Schwankungsbreite der Kontroll-Modellrechnung bewegte.

Die Effekte einer Reduzierung der Feuchte in der mittleren Troposphäre, einer verstärkten Strahlungsabkühlung und einer oberen antizyklonalen Scherströmung, wurden ebenfalls untersucht. Es wurde belegt, dass die Entwicklung von Wirbelstürmen empfindlich von diesen drei Faktoren abhängt. Die Verschmelzung der Meso-Wirbel ist wegen der Reduzierung des Auftriebs in der Kumuluskonvektion verzögert. Ensembleberechnungen zeigen auch, dass die Vorhersagbarkeit während der Periode der Intensivierung von Wirbelstürmen gering ist. Erhebliche Schwankungen der Intensität des Wirbelsturms in den Rechnungen der einzelnen Mitglieder des Ensembles zu einem festgelegten Zeitpunkt

deuten auf die Grenzen der Vorhersagbarkeit einzelner Modellrechnungen hin.

# Contents

<b>1</b>	<b>Introduction</b>	<b>1</b>
1.1	Motivation and purpose . . . . .	1
1.2	Preliminaries . . . . .	5
1.2.1	The formation of a tropical cyclone . . . . .	5
1.2.2	The structure of a mature tropical cyclone . . . . .	6
1.2.3	Convective instability . . . . .	7
1.3	Overview of chapters . . . . .	10
<b>2</b>	<b>The Burdekin thunderstorm</b>	<b>13</b>
2.1	Introduction . . . . .	13
2.2	Data sources . . . . .	15
2.3	Synoptic situation . . . . .	15
2.4	CAPE and CIN . . . . .	20
2.5	Low-level wind shear . . . . .	25
2.6	Summary . . . . .	26
<b>3</b>	<b>Tropical cyclones Theodore and Rewa</b>	<b>29</b>
3.1	Introduction . . . . .	29
3.2	Theodore . . . . .	30
3.3	Rewa . . . . .	39
3.4	Summary . . . . .	46
<b>4</b>	<b>The control numerical experiments</b>	<b>49</b>
4.1	Introduction . . . . .	49
4.2	Model description . . . . .	50
4.3	The control run . . . . .	52
4.4	Ensemble calculations . . . . .	61
4.5	Dependence on surface fluxes . . . . .	64
4.6	Summary . . . . .	67
<b>5</b>	<b>Some factors affecting vortex intensification</b>	<b>69</b>
5.1	Introduction . . . . .	69
5.2	Radiative cooling . . . . .	70

---

5.3	Dryness in the middle-troposphere . . . . .	77
5.4	Anticyclonic upper-level shear flow . . . . .	85
5.5	Summary . . . . .	94
<b>6</b>	<b>Summary and conclusions</b>	<b>97</b>
<b>A</b>	<b>The ECMWF model and ERA-40</b>	<b>99</b>
<b>B</b>	<b>The minimal 3-D tropical cyclone model</b>	<b>105</b>
<b>C</b>	<b>List of Acronyms</b>	<b>109</b>
	<b>Bibliography</b>	<b>113</b>
	<b>Acknowledgements</b>	<b>119</b>

# Chapter 1

## Introduction

### 1.1 Motivation and purpose

Tropical cyclones rate with earthquakes as one of the most devastating types of natural phenomena and they are a regular threat to coastal communities in regions where they occur. It is essential to provide these communities with accurate forecasts of the storm track and intensity well in advance to allow actions to be taken to protect life and minimize damage to property. There are concerns also that tropical cyclones will become more destructive as a result of future global warming (Emanuel 2005, Webster *et al.* 2005) and these fears have been heightened by the increase in hurricane activity in the Atlantic basin during last few years.

There is a consensus amongst tropical cyclone researchers that the current skill in intensity forecasts lies way behind that in track forecasts. Efforts to improve intensity forecasts have focused almost exclusively on characterizing interactions between a tropical cyclone and its environment (e.g. Molinari and Vollaro 1989, 1990; Montgomery and Farrell 1993; Molinari *et al.* 1995; DeMaria and Kaplan 1999; Emanuel *et al.* 2004). The greatest potential for the interactions has been suggested to exist in the upper-troposphere, where inertial stability is generally lowest (e.g. Pfeffer and Challa 1981). Upper tropospheric influences on tropical cyclone intensification were emphasized in many studies (Colón and Nightingale 1963; Erickson 1963; Molinari and Vollaro 1989). In particular, a major effort has been made to understand the influence of an *upper-level trough*, since rapid intensification has been observed on some occasions when the trough approaches a tropical cyclone (e.g. Molinari *et al.* 1995, Bracken and Bosart 2000). An upper-level trough refers to a low pressure system that is below the tropopause, but lies in an upper half of the troposphere and is not significantly affected by friction (Bluestein 1993). Case studies of Tropical Cyclones

Irma (1987) and Jason (1987) in the Australian region showed that a transformation of tropical meso-scale convective complexes to a tropical cyclone occurred in the vicinity of an upper-level trough (Davidson *et al.* 1990). Tropical cyclones are more likely to intensify than weaken after an interaction with an upper-level trough when cyclones are moving over warm water (Hanley *et al.* 2001).

An aspect of an approaching upper-level trough that might lead to the intensification of a tropical cyclone is the convective destabilization brought about by raising isentropic surfaces throughout the troposphere. The upward displacements of the isentropes are a characteristic pattern associated with an upper-level trough, which is represented by a positive Potential Vorticity (PV) anomaly located near the tropopause in the Northern Hemisphere (Fig. 1.1). The isentropic coordinate form of PV (Ertel PV<sup>1</sup>) is defined as  $PV = -g(f + \mathbf{k} \cdot \nabla_{\theta} \times \mathbf{v}) / (\frac{\partial p}{\partial \theta})$ , where  $\mathbf{k}$  is a unit vertical vector,  $\nabla_{\theta}$  is the three-dimensional gradient operator in  $\theta$ -coordinates,  $p$  is the pressure,  $f$  is the Coriolis parameter, and  $g$  is the acceleration due to gravity. A positive PV anomaly has an associated cyclonic circulation that is most intense at the level of the anomaly and decays with height above and below the anomaly. Isentropes are raised below the anomaly, indicating reduced static stability, and are lowered above, reflecting the lowered tropopause in the vicinity of the anomaly. An important feature of the vertical structures is that they are carried along with the anomaly if it moves. If the upper-level trough advances, air below and ahead of it must ascend along the raised isentropic surfaces, while air behind it descends along the isentropes. The ascending air cools adiabatically in the atmosphere.

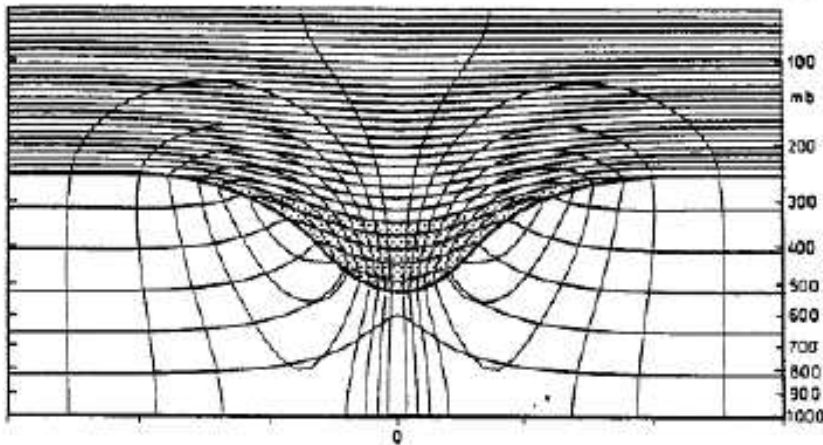


Figure 1.1: Symmetric flows induced by simple, isolated, upper-level PV positive anomaly (location stippled) in the Northern Hemisphere. The quasi-horizontal lines are the isentropes while the thinner lines are the isothachs. The thick line represents the tropopause (Hoskins *et al.* 1985).

In a theoretical calculation, the cooling associated with the approach of an upper-level trough destabilized the unsaturated atmosphere to convection (Jukes and Smith 2000). A question raised is whether convective destabilization occurs in the real atmosphere when an upper-level trough approaches. This question has motivated me to examine convective

<sup>1</sup>Named after German meteorologist Hans Ertel

instability changes in a pre-storm environment and in the tropical atmosphere in which a tropical cyclone intensifies when an upper-level trough approaches in real cases. Data from the European Centre for Medium-Range Weather Forecasts (ECMWF) are used for these diagnostic case studies. In spite of occasional errors in positioning the tropical cyclone centre, the ECMWF model analysis contains useful information to allow individual case studies of tropical-cyclone environments (Molinari *et al.* 1991). Details of the ECMWF model and data system are explained in Appendix A.

Many of the environmental factors hypothesized to influence the intensification of a cyclone have been examined in numerical models, but the effect of convective instability has been little investigated (Persing and Montgomery 2005). The key question in discussing the role of moist convection in the intensification of a tropical cyclone is how to determine the coupling between the convection and the cyclone circulation on scales greater than individual convective systems (e.g. Ooyama 1982). A vortex intensifies as a result of radial buoyancy gradients associated with convective heating in the core region. The simulations of tropical cyclone intensification have succeeded with some degree of realism irrespective of convective schemes, since the buoyancy gradients are produced by all cumulus parametrization schemes, as well as by a simple explicit moisture scheme in a tropical cyclone model (Zhu *et al.* 2001). Ooyama (1982) proposed that the presence of convective instability is essential to the deep-layer inflow toward the vortex centre for the development of an incipient vortex into a mature tropical cyclone. On the other hand, Rotunno and Emanuel (1987) demonstrated the intensification of the tropical cyclone in an environment which is in a neutral state to convection. The premise of Emanuel's (1986) theory is that the way to obtain energy from the ocean for tropical cyclone intensification is the transfer of moisture from the ocean to the atmosphere, which is dependent on wind speed and the difference of moisture content between the air and the saturation mixing ratio at the sea surface. The author suggested that initially available energy is not essential for the intensification of the cyclone. His idea is based on the analysis of a large number of soundings from several tropical stations, which shows that the tropical atmosphere is almost neutral to parcels lifted reversibly from the top of the *boundary layer*<sup>2</sup> (Xu and Emanuel 1989). Persing and Montgomery (2005) suggested also that an upper bound on tropical cyclone intensity, referred to as *potential intensity*, was independent of environmental convective instability in the axisymmetric model of Rotunno and Emanuel (1987). The potential intensity is determined by the maximum possible latent heat input from the ocean to the atmosphere through the surface heat fluxes. My study aims to examine the extent to which vortex intensification is captured when the wind-speed dependence of the surface fluxes is suppressed and to investigate the sensitivity of the intensification to the moisture content in the boundary layer after the onset of grid-scale saturation. A simple tropical cyclone model developed by Zhu *et al.* (2001) is used to model the intensification of an incipient vortex to a mature tropical cyclone. The horizontal resolution of the model is doubled (horizontal grid 10 km instead of 20 km) and the number of vertical layers is increased from 3 to 4. More details of the model are explained in Appendix B. The evolutionary processes during the early stage of cyclone intensification described in the near cloud-resolving ( $\sim 2\text{-}3$  km) simulation for tropical cyclogenesis (Montgomery *et al.* 2006) are captured in a large part

---

<sup>2</sup>The boundary layer is the part of the troposphere that is directly influenced by the presence of the earth's surface and its thickness is quite variable in time and space, ranging from hundreds meters to a few km.

by this model.

Figure 1.2 shows convectively-induced asymmetries within an intense-hurricane circulation. There is a growing emphasis on the role of the asymmetries in tropical-cyclone intensification since the asymmetries can evolve into coherent sub-system-scale vortices about the parent vortex and induce intensity changes (Montgomery *et al.* 2006). The sub-system-scale vortices are referred to as *meso-vortices* or *vortical hot towers* (Montgomery *et al.* 2006). Here, the dependency of vortex intensification on the change of an azimuthal wave-number is of special interest. The evolution to a low azimuthal-wave-number asymmetry is characterized by the subsequent merger of neighbouring meso-vortices. The formation of meso-vortices and their merging processes were observed also in the two-dimensional barotropic calculation (Kossin and Schubert 2001). They suggested that meso-vortices relaxed to a monopole or maintained an asymmetric quasi-steady state depending on the initial condition. Dramatic central pressure falls were shown when the vortices merged to form a monopole. I examine the sensitivity of the formation and subsequent merger of meso-vortices to the boundary-layer moisture content. In addition, the effects of radiative cooling rate, the humidity in the middle-troposphere, and to an upper-level, anticyclonic, shear flow on the evolutionary process are investigated.

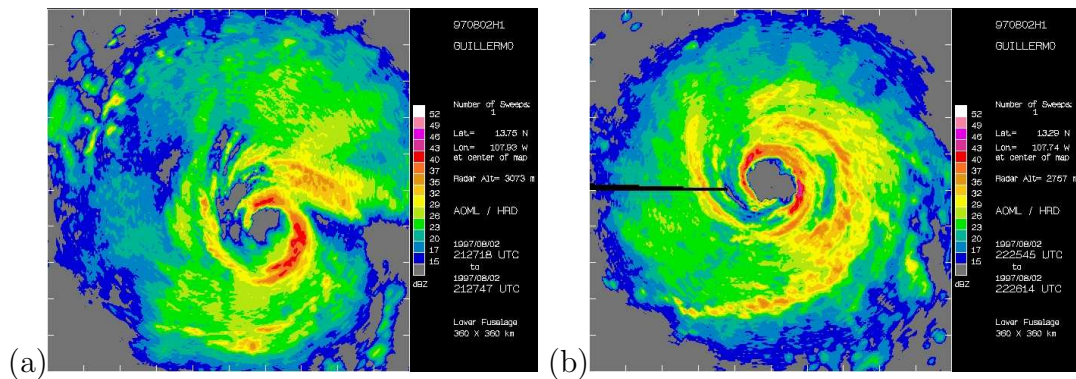


Figure 1.2: Airborne-radar reflectivity in Hurricane Guillermo at (a) 2127 UTC (GMT) and (b) 2226 UTC on 2 August 1997. Image courtesy of Hurricane Research Division (HRD).

A deterministic numerical simulation describes the future development of a single initial state that is imperfectly known. Since we cannot measure the initial state accurately, there are intrinsic uncertainties in the initial condition. Even if the single deterministic forecast is the best possible one, its reliability will be enhanced if the forecasts that begin with perturbed initial states are examined. This approach in an effort to improve the skill of weather forecasts is so called an *ensemble forecast* (Wilks 2006). The production of ensemble forecasts is based on a number of possible initial atmospheric states drawn randomly from a function of initial-condition uncertainty. Since the pattern of deep convection is strongly influenced by the low-level moisture field, which has significant variability on small space scales (Weckwerth 2000), it is appropriate to produce ensemble forecasts of tropical cyclone intensification in which the ensemble members have randomly perturbed initial moisture fields. This ensemble-approach is applied in this study using a minimal hydrostatic model. A study of this kind has been completed recently by Nguyen *et al.*

2007 (personal communication) using a multi-layer nonhydrostatic model. I will show the limitation of predictability of vortex intensity in a single deterministic calculation. Only features that survive an ensemble-average might be regarded as robust and these features characterize vortex intensification in numerical experiments.

In the forthcoming section, preliminary knowledge and terminology are provided to help readers to understand results and discussions in this study.

## 1.2 Preliminaries

### 1.2.1 The formation of a tropical cyclone

The nature of tropical cyclogenesis is not clearly understood. An incipient tropical storm arises by chance from a disturbance with organized convective activity (Ooyama 1982). Such disturbances are generally 200 to 600 km in diameter. Some disturbances progress from east to west and are known as easterly waves in the Atlantic. Satellite observations of the disturbances over the tropical oceans have shown that only 1-2 % develop into tropical cyclones (e.g. Simpson and Riehl 1981). However, there are some prerequisite conditions for the formation of a cyclone (Gray 1968). Warm ocean water of at least about 26°-27°C throughout a sufficient depth (at least on the order of 50 m) is the energy source for the development of a tropical cyclone. Background planetary vorticity should be greater than  $0.8-1.3 \times 10^{-5} \text{ s}^{-1}$ , which is the value of the Coriolis parameter ( $f$ ) at 3°-5° off the equator, to allow the low pressure of a tropical disturbance to be maintained. Vertical wind shear is the vertical gradient of the wind vector. Weak vertical wind shear is a necessary condition for the development of an incipient tropical cyclone. Having these conditions met is necessary, but not sufficient, since many tropical disturbances that appear to exist in the environment of these conditions do not develop into a tropical storm (Gray 1968).

The *intensity* of a tropical cyclone is measured conventionally in terms of the maximum wind near the surface. Once a low-pressure system over tropical or sub-tropical waters with organized convection reaches winds of at least  $17 \text{ m s}^{-1}$  it is typically called a *tropical storm* and assigned a name. If the 1 min<sup>3</sup> mean wind reaches  $33 \text{ m s}^{-1}$ , then the storm is called *severe tropical cyclone* over the Southwest Pacific Ocean west of 160°E, *Typhoon* over the Western North Pacific Ocean, and *hurricane* over the North Atlantic Ocean, the Northeast Pacific Ocean east of the dateline, or the South Pacific Ocean east of 160° E. The problem of how a synoptic-scale tropical disturbance transforms into a meso-scale tropical storm does not well known. Early works hypothesized that the deep convection cooperated with a tropical disturbance in a positive feedback process is responsible for the transformation (Ooyama 1964). Zehr (1992) suggested that the genesis of a tropical cyclone occurs if Meso-scale Convective Vortices (MCVs) develop in the region of a tropical disturbance.

---

<sup>3</sup>The National Hurricane Center of United States of America uses a 1-min averaging time for reporting the sustained surface winds in the Atlantic and Northeast Pacific tropical cyclone basins. However, in the rest of the world, a 10-min averaging time is utilized for the sustained wind. This systematic difference makes inter-basin comparison of tropical cyclones around the world problematic.

Recently, cloud-resolving model calculations proposed that *vortical hot towers* of small-scale deep convection emerged in the region of MCVs were responsible for the generation of a tropical storm (Hendricks *et al.* 2004, Montgomery *et al.* 2006).

### 1.2.2 The structure of a mature tropical cyclone

Typically the strongest winds of a mature tropical cyclone occur in a ring some tens of kilometers from the centre and there is a calm region around the centre, the *eye*, a roughly circular area within a small radius (mostly 30-60 km). The counter-clockwise tangential wind around the centre of a tropical cyclone in the Northern Hemisphere is the so-called *primary circulation*, which becomes nearly axisymmetric as the cyclone matures. The eye is normally free of deep clouds and winds are light in the region. Figure 1.3 shows the cloud-free eye surrounded by clouds of Hurricane Isabel (2003). The warmest temperatures are found in the eye due to the subsidence during the formative stage of the cyclone. The subsidence in the eye is explained by Smith (1980) by assuming that the primary circulation is in gradient wind balance:

$$\frac{v^2}{r} + fv = \frac{1}{\rho_p} \frac{\partial p}{\partial r}, \quad (1.1)$$

where  $\rho_p$  is air density,  $v$  the tangential (azimuthal) wind, and  $r$  is the radius. If Equation (1.1) is integrated with radius and then differentiated with respect to height and divided by the density, the perturbation pressure gradient per unit mass along the vortex axis is obtained:

$$-\frac{1}{\rho} \frac{\partial(p_0 - p_\infty)}{\partial z} = -\frac{1}{\rho} \frac{\partial}{\partial z} \int_0^\infty \rho \left( \frac{v^2}{r} + fv \right) dr, \quad (1.2)$$

where  $p_0$  is the pressure at the vortex axis and  $p_\infty$  is the environmental pressure. Observations in tropical cyclones show that the tangential wind speed decreases with height above the boundary layer and the radius of the maximum tangential wind speed increases with height. Then Equation (1.2) indicates that the perturbation pressure gradient force directs downward along the vortex axis. This gradient force leads to subsidence along and near the axis, which allows the air to be buoyant relative to the ambient air at the same level outside the eye. The upward buoyancy approximately balances the downward-directed perturbation pressure gradient force so that a small residual force acts to drive the actual subsidence (Smith 1980). As the vortex strengthens, the downward pressure gradient must increase and the residual force directs downwards to drive further subsidence. If the vortex weakens, the residual force directs upwards, allowing the air to ascend in the eye.

The eye is surrounded by a ring of deep convective *eye-wall* cloud that slopes outwards with height. The primary circulation is strongest at low-levels in the eye-wall cloud region and decreases in intensity with both radius and height. The cyclonically spiraling air near

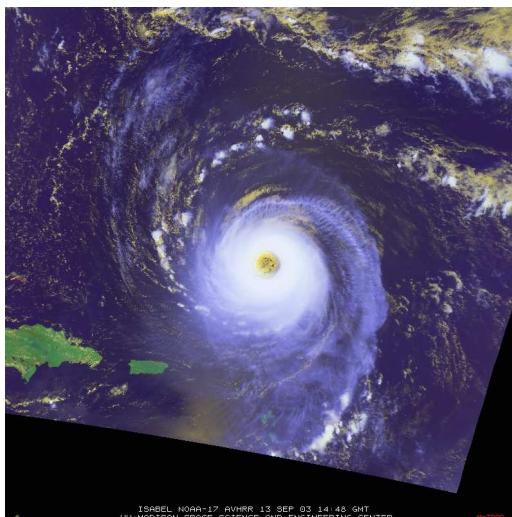


Figure 1.3: Satellite imagery at 1448 GMT on 13 September 2003, showing the clear eye of the intense Tropical Cyclone, Isabel. Image courtesy of National Oceanic Atmospheric Administration (NOAA) hurricane research division.

the surface converges towards the centre of low pressure due to the surface friction in the boundary layer. The spiraling motions are often evident in cloud patterns with low cloud-top temperature seen in satellite imagery. The converged air is forced upwards out of the boundary layer so that it experiences cooling associated with adiabatic expansion and latent heating released through condensation. While most of the latent heat is balanced by the adiabatic cooling, a small fraction of the heat released appears as an elevated temperature perturbation at a particular height. The updrafts rise as high as the tropopause and then diverge outward and descend either in the eye or at outer radii. The circulation outside a radius of a few hundred kilometers in the upper-troposphere is anticyclonic. The radial inflow toward the vortex axis, updraft, and outflow comprise the *secondary circulation* (Fig. 1.4).

### 1.2.3 Convective instability

Tropical soundings frequently indicate that the atmosphere is stable to small vertical displacements, but unstable to large vertical displacements, especially upward displacements of low-level air parcels.

The buoyancy of an air parcel in a density-stratified atmosphere is defined as the difference between the weight of air displaced by the parcel and the weight of the parcel itself. If an isolated air parcel of density  $\rho_p$  is displaced in an environment of density  $\rho_a$ , the buoyancy force per unit mass is

$$B = -g\left(\frac{\rho_p - \rho_a}{\rho_p}\right), \quad (1.3)$$

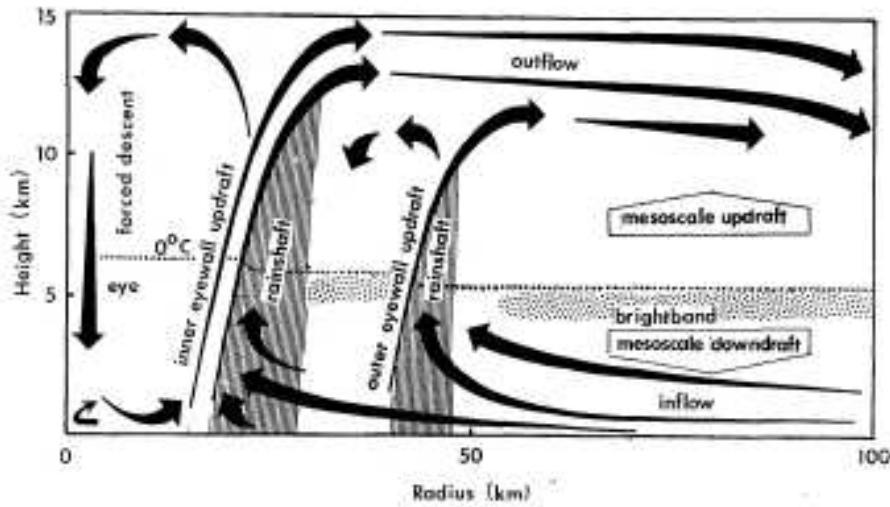


Figure 1.4: Schematic of secondary circulation and precipitation distribution for a tropical cyclone similar to Hurricane Gilbert (1988) (Willoughby 1988).

where  $g$  is the gravitational acceleration. The calculation assumes that pressure within the air parcel is the same as that of its environment at the same level. This assumption is not valid for air parcels in an intense vortex in which the central pressure is much less than that in the environment at the same level. An air parcel experiences not only the gravitational force, but also a centrifugal force ( $v^2/r$ ) and Coriolis force ( $f v$ ), where  $v$  is the tangential wind at a radius  $r$  and  $f$  is the Coriolis parameter (Fig. 1.5). Subsequently, isobaric surfaces have a vertical slope that is normal to the effective gravity,  $\mathbf{g}_e = (v^2/r + f v, g)$  (Smith *et al.* 2005). The radial component of buoyancy makes a negligibly small contribution to the toroidal vorticity<sup>4</sup> generation in a tropical cyclone, but is significant in tornadoes.

The mixing ratio ( $r$ ) is a useful measurement of amount of water in the atmosphere. This is defined as the mass of water vapour per unit mass of dry air. An almost equivalent measurement of water content is the specific humidity ( $q$ ), which is the mass of water vapour per unit mass of air including the vapour. The saturation mixing ratio ( $r^*$ ) and saturation specific humidity ( $q^*$ ) represent the maximum amount of water that the air can hold at the same pressure ( $p$ ) and temperature ( $T$ ). The vapour pressure is the partial pressure of water vapour and defined by  $e = r p / (\epsilon + r)$ , where  $\epsilon$  is the ratio of the specific gas constant for dry air  $R_d$  to the constant for water vapour  $R_v$ . The relative humidity  $RH = 100 \times e/e^*$ , where  $e^* = e^*(T)$  is the saturation vapour pressure.

The volume per unit mass of moist air is defined as

$$\alpha = R' \frac{T}{p}. \quad (1.4)$$

<sup>4</sup>The toroidal vorticity is defined by  $\eta = \partial u / \partial z - \partial w / \partial r$ , where  $u$  and  $w$  is the radial and vertical wind component.

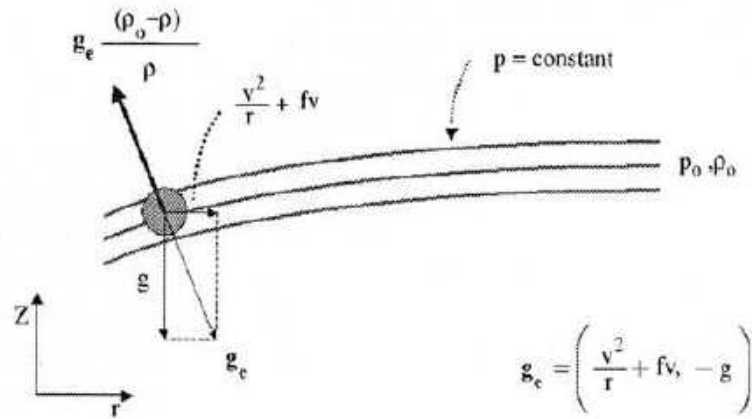


Figure 1.5: Schematic radial-height cross-section of isobaric surfaces showing the forces on an air parcel including the gravitational force and the centrifugal and Coriolis forces (Smith *et al.* 2005). Refer to more details in text.

The effective gas constant  $R'$  is defined by

$$R' = R_d \frac{1 + r/\epsilon}{1 + r}. \quad (1.5)$$

The effective gas constant  $R'$  is larger than  $R_d$  because  $\epsilon$  is less than 1. Thus, the volume of moist air is larger than that of dry air and varies with water vapour content. Consequently, the density of moist air is lower than that of dry air and this should be considered in the estimation of buoyancy. The virtual temperature ( $T_v$ ) is defined as the adjusted temperature that dry air would have to yield the same density as moist air at the same pressure. Thus the relation between temperature and the virtual temperature is defined by

$$R'T \equiv R_d T_v. \quad (1.6)$$

Convective Available Potential Energy (CAPE) is a thermodynamic parameter of convective instability. The CAPE represents a measure of energy available to a rising cloud parcel and in conjunction with wind shear has been used to determine the nature of the resulting convective meso-scale systems (Weisman and Klemp 1982). An air parcel is negatively buoyant until it is displaced to the level of free convection (LFC) from which it becomes unstable. The CAPE is measured by integrating the vertical component of buoyancy of an air parcel lifted upwards from a level to the level of neutral buoyancy (LNB):

$$CAPE = \int_Z^{Z_{LNB}} B dz, \quad (1.7)$$

where  $Z$  is the height of a certain level where a parcel is lifted and  $Z_{LNB}$  is the height

of LNB. It is convenient to estimate buoyancy  $B$  using the virtual temperature ( $T_v$ ) instead using density as in Equation (1.3). Assuming the environment to be in hydrostatic equilibrium and using the ideal gas law, CAPE is

$$CAPE = \int_{p_{LNB}}^{p_z} R_d(T_v - T_{v_a}) d \ln p, \quad (1.8)$$

where  $T_{v_a}$  is virtual temperature of the environment at the same pressure level as a lifted air parcel. An air parcel should be lifted above the LFC otherwise it cannot reach its LNB by consuming its CAPE through deep convection. The energy needed to lift the parcel from the surface to the LFC is called the Convective Inhibition (CIN) and calculated in a similar way to CAPE,

$$CIN = - \int_{p_{LFC}}^{p_z} R_d(T_v - T_{v_a}) d \ln p. \quad (1.9)$$

CAPE and CIN are useful measures of convective instability of the atmosphere. Large values of CAPE are a predictor of the severity of convection and CIN is an index for predicting whether convection will form (Colby 1984).

There are two approximations for a moist adiabatic process, a reversible-adiabatic and a pseudo-adiabatic process. In the reversible process, all the condensed water is assumed to be carried along by the ascending air. On the other hand, all the condensed water is assumed to be immediately and irreversibly removed from the system. As a result, the reversibly lifted air parcel has the higher density due to the condensate than the parcels in the pseudoadiabatic ascent through most of the troposphere. The condensed water will tend to reduce the buoyancy of a rising parcel. Moreover, some latent heat has to go into heating the condensate in the reversible process.

### 1.3 Overview of chapters

The convective instability changes during the approach of an upper-level trough in a thunderstorm case are examined in chapter 2<sup>5</sup>. This investigation attempts to estimate the convective destabilization by an upper-level trough in the absence of a tropical cyclone. In chapter 3, the influence of an approaching upper-level trough on convective instability is examined in two cases of a rapidly-intensifying tropical cyclone. The skill of the ECMWF model in capturing the cyclones is discussed and synoptic conditions during the approach of the upper-level trough are examined. A control experiment using a simple model is discussed in chapter 4, in which the intensification of a tropical-cyclone-like vortex is comprehensively described. The sensitivity of the vortex intensification to the perturbation of

---

<sup>5</sup>This work has been published (Shin et al. 2005) and the content of this chapter is nearly the same as the paper.

the boundary-layer mixing ratio is explored with ensemble calculations. In chapter 5, some factors that affect vortex intensification are investigated and the predictability of intensity is discussed. In chapter 6, a summary of the results and conclusions are presented.



# Chapter 2

## The Burdekin thunderstorm

### 2.1 Introduction

On 19 January 2001, a band of severe thunderstorms moved through the Burdekin (Ayr-Home Hill) area of northern Queensland just after 0800 Greenwich Mean Time (GMT) (6 pm local time) causing widespread damage. Two houses were demolished, six caravans were destroyed and power lines were downed. Established trees were uprooted and stripped of leaves and there was widespread crop damage. A number of reports of hail were received. More than 26,200 lightning strikes were recorded in one hour, which is an Australian record. This was an unusual event as severe thunderstorms are almost unheard of in this area. A sequence of enhanced infra-red satellite images at selected times during the event is shown in Fig. 2.1. The early echoes appeared over the Great Dividing Ranges to the west of Townsville at 0330 GMT, but the cells that affected the Ayr-Home Hill area developed from a further group of cells that formed to the southeast of Townsville (Fig. 2.1a). By 1130 GMT the cells had developed further and merged to cover a large region inland from the coast and a second storm complex had formed to the south of the Gulf of Carpentaria (Fig. 2.1d). This study investigates the meteorological circumstances that lead to the formation of the Burdekin storms and, in particular, examines the possible role of an upper-level trough and a surface heat low in the vicinity.

The severity and type of thunderstorm that develops in a particular location is thought to be strongly influenced by the amount of CAPE, by the strength of the low-level vertical shear, and by the change in the wind direction with height (see e.g. Weisman and Klemp 1982, 1984, 1986; Bluestein and Jain 1985; Weisman and Rotunno 2004, and references therein). On the other hand, the initiation of storms depends strongly on the CIN. Specifically, CAPE is a measure of the energy that can be released when an air parcel ascends from its current position up to the level of neutral buoyancy, while CIN is a measure of the work that is required to lift an air parcel to its level of free convection (see e.g. Emanuel, 1994). It is usual to calculate the CAPE and CIN for air parcels lifted from the surface or for hypothetical parcels with the mean properties of the lowest few hundred meters. Typically, CAPE is a strongly decreasing function and CIN is a strongly increasing function of

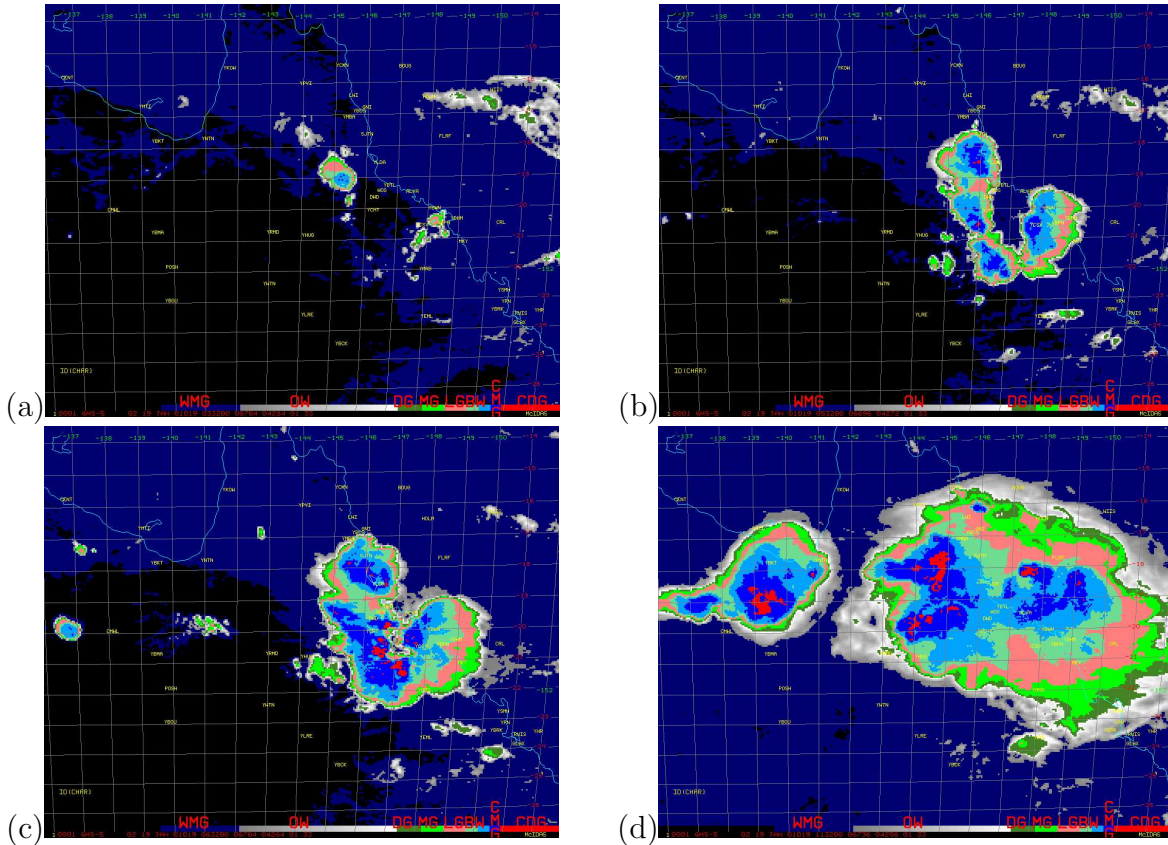


Figure 2.1: Enhanced infrared satellite imagery at (a) 0330 GMT, (b) 0530 GMT, (c) 0630 GMT, and (d) 1130 GMT on 19 January, showing the evolution of the severe thunderstorms from the early cells.

the altitude of the lifted parcel.

In this study we calculate the spatial distributions of CAPE and CIN prior to the development of the Burdekin thunderstorms. We examine also the low-level shear in the vicinity of the storms and estimate the bulk Richardson number for the storm environment from upper-air data at Townsville. This study uses mainly ECMWF analysis data. Protat and Lemaître (2001) used similar data sets to examine the synoptic-scale environment of meso-scale convective systems observed during Tropical Ocean Global Atmosphere Coupled Ocean-Atmosphere Response Experiment (TOGA COARE) and, in particular, the CAPE distribution. They found, *inter alia*, that the evolution of convective systems was generally controlled by the time evolution of CAPE and the synoptic-scale low-level convergence.

The layout of this chapter is as follows. Section 2.2 provides a brief description of the ECMWF data sets. Then, in section 2.3 we examine the synoptic situation prior to and during the evolution of the Burdekin thunderstorms, focusing on the presence of an upper-level trough and a shallow heat low that was connected to a frontal-like trough over the Tasman Sea. In section 2.4 we present analyses of CAPE and CIN as well as the short range convective precipitation forecasts of the ECMWF model. The low-level wind shear is examined in section 2.5 and the conclusions are given in section 2.6.

## 2.2 Data sources

Hourly Japanese Geostationary Meteorological Satellite (GMS) imagery is used to examine the evolution of the thunderstorms. The other main data source is the ECMWF operational analyses, which provide data on 60 vertical layers with a  $1^\circ \times 1^\circ$  horizontal resolution. The domain of interest here extends zonally from  $130^\circ\text{E}$  to  $170^\circ\text{E}$  and meridionally from  $0^\circ\text{S}$  to  $40^\circ\text{S}$ , an area that includes the eastern part of the Australian continent and part of the Southwest Pacific Ocean. The orography used in the ECMWF model is shown in Fig. 2.2 together with locations mentioned in the text. Short-range accumulated convective precipitation forecasts are examined to see how well the model captured the storms. Comparisons are made between data from the ECMWF analyses and from the Townsville radiosonde sounding at 2300 GMT on 18 January and the rawinsonde sounding at 0500 GMT on 19 January.

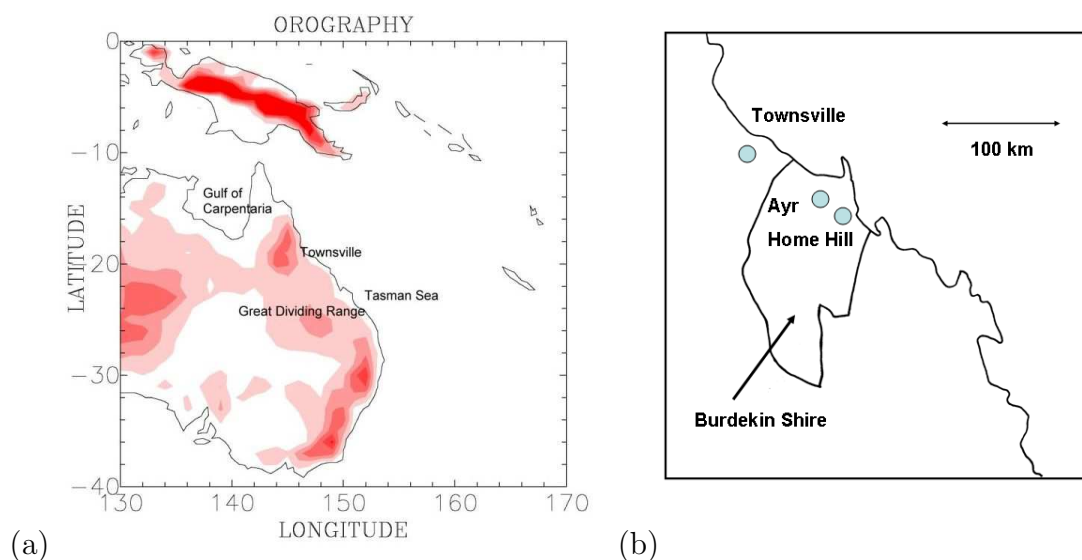


Figure 2.2: (a) Orography used in the ECMWF model. The shading starts from the 200 m-height contour and the contour interval is 200 m. Places mentioned in this study are referred to this figure. (b) the Burdekin area of northeastern Australia.

## 2.3 Synoptic situation

Figure 2.3 shows the mean sea level pressure distribution over eastern Australia at 1800 GMT on 17 and 18 January 2001 and at 0000 and 0600 GMT on 19 January. The chart for 1800 GMT on 17 January shows a trough system with three separate lows located over the central and eastern parts of Australia and over the Tasman Sea. One day later, at 1800 GMT on 18 January, the two lows had amalgamated to cover a broad area of central Queensland while the low over the Tasman Sea had moved eastwards. Both lows deepened by over 3 hPa during this 24 h period, while a ridge formed between them over the Great

Dividing Range. A similar type of shallow ridge influenced by orography was analysed in a study of the interaction of an extra-tropical cyclone with coastal orography in the Pacific Northwest of the United States by Steenburgh *et al.* (1996).

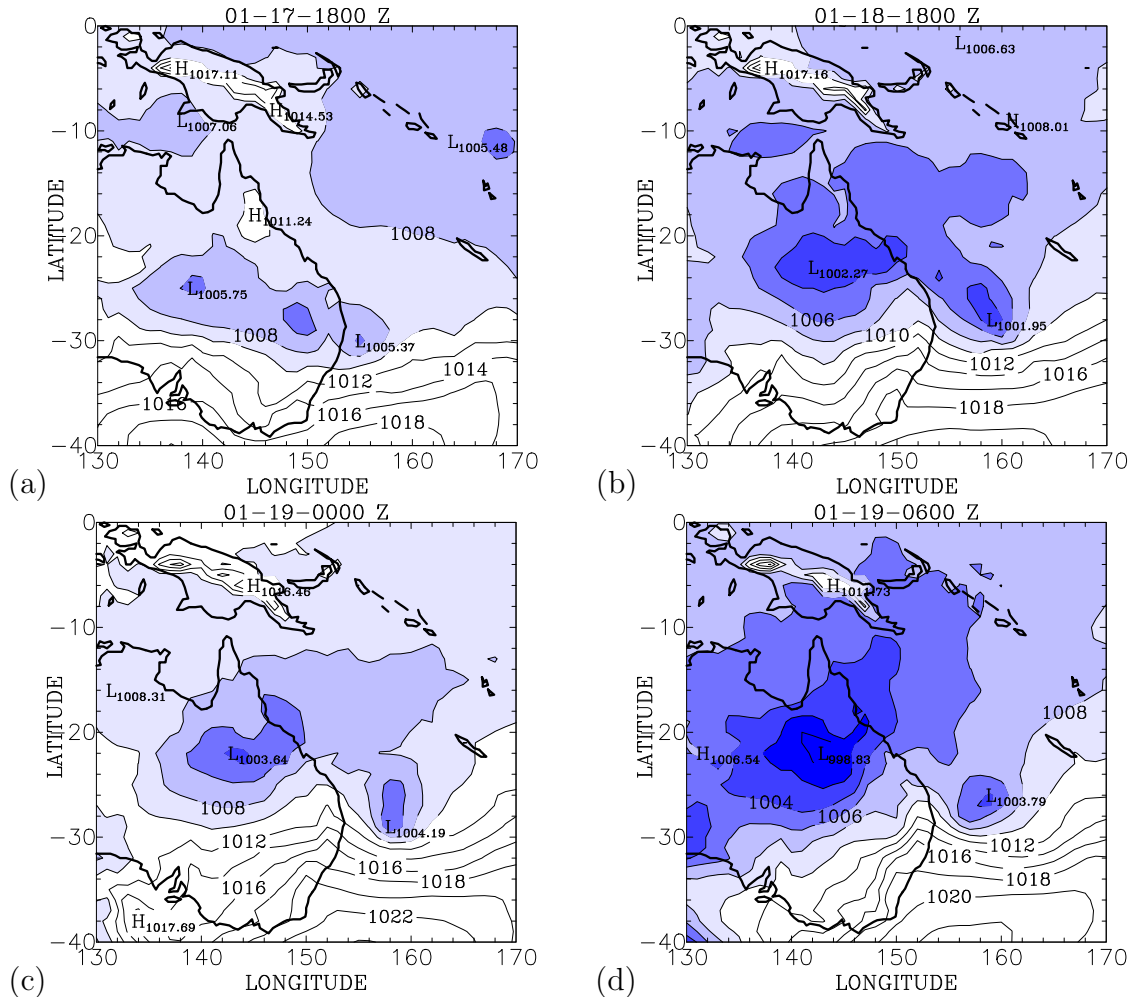


Figure 2.3: Mean sea level pressure over eastern Australia at: 1800 GMT on (a) 17 January 2001 and (b) 18 January; (c) 0000 GMT and (d) 0600 GMT on 19 January. Pressure values lower than 1008 hPa are shaded with darker shading at intervals of 2 hPa.

The low over the continent filled by about 1.5 hPa to 0000 GMT, presumably on account of the semi-diurnal pressure wave, which had a local maximum near this time. However it deepened during the daytime so that by 0600 GMT the minimum surface pressure over northern Queensland had fallen from nearly 1004 hPa at 0000 GMT to around 998 hPa. A fraction of this decline can be attributed to the normal diurnal variation which has a mean fall of about 2.5 hPa during this time. A meridional-vertical cross-section of potential temperature through the centre of low over Queensland at 0600 GMT on 19 January shows that this system had the structure of a heat low, with the warmest air and deepest mixed layer near the centre (Fig. 2.4). The warm anomaly was confined to pressures higher than about 600 hPa. The Burdekin thunderstorms formed first on the northeastern side of this low pressure region. Later, another thunderstorm complex developed about 400 km to the northwest of it.

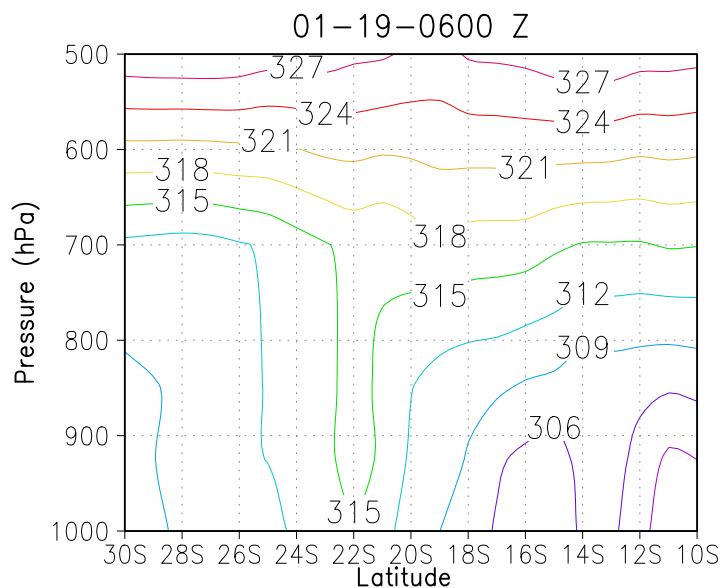


Figure 2.4: Meridional-height cross-section of potential temperature at a longitude of  $143^{\circ}\text{E}$ , approximately through the centre of the heat low over northern Queensland, at 0600 GMT on 19 January.

The evolution of the divergent component of the low-level airflow over northeastern Queensland leading to the formation of the Burdekin thunderstorms is characterized by the ageostrophic wind at 925 hPa at 6-hourly intervals from 1800 GMT on 18 January to 1200 GMT on 19 January shown in Fig. 2.5. At 1800 GMT on 18 January, there were three prominent low-level airstreams feeding into the heat low and leading to ascent along the trough line; one was a northerly airstream originating from the gulf on the western side of the heat low; another was a southerly airstream on the southern side of the low; and the third was a northeasterly airstream from the ocean on the northeastern side of the low. Figure 2.5 shows also the distribution of vertical velocity at 850 hPa, which at the foregoing time indicated an extensive strip of enhanced ascent stretching zonally along the inland trough through the low centre and connecting to the trough trailing from the low over the Tasman Sea (see Fig. 3). Enhanced convergence in the trough during the night is associated with the low-level nocturnal jet (see e.g. Reeder and Smith, 1998; Spengler *et al.* 2005).

By 0000 GMT on 19 January the ascent along the trough line over the continent had all but disappeared, presumably a result of the breakdown of the low-level jet following renewed dry convective heating. However, the convergent region associated with the trailing trough had moved a little northwards and had extended westwards. The first convective cells of the Burdekin storm system occurred about two hours later near this region.

At 0630 GMT on 19 January, half an hour after the next analysis time, the storms already covered a large area (Fig. 2.1c) and broadly coincided with a region of enhanced ascent centred at about  $21^{\circ}\text{S}$ ,  $148^{\circ}\text{E}$  (Fig. 2.5c) at 0600 GMT. A second band of enhanced ascent at this time lay in the vicinity of the heat low centre, stretching southeastwards from about

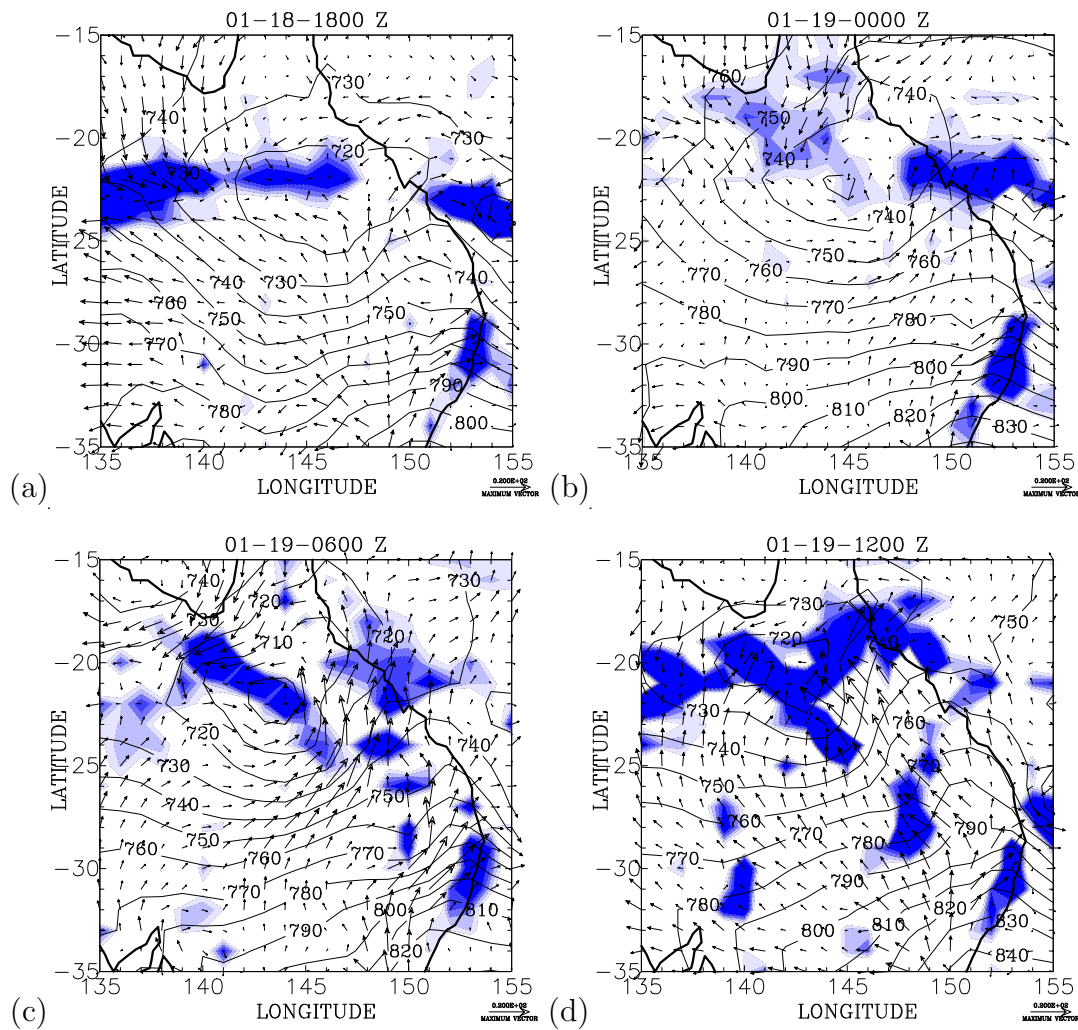


Figure 2.5: Ageostrophic wind at 925 hPa (in  $\text{m s}^{-1}$ ) and 850 hPa vertical velocity at (a) 1800 GMT on 18 January, (b) 0000 GMT, (c) 0600 GMT, and (d) 1200 GMT on 19 January as indicated. The geopotential heights at 925 hPa-level are also plotted. Vertical velocities less than  $-0.1 \text{ Pa s}^{-1}$  are shaded at intervals of  $0.05 \text{ Pa s}^{-1}$ .

$19^{\circ}\text{S}$ ,  $139^{\circ}\text{E}$  and further cells were developing on the westernmost end of this band at 0600 GMT (Fig. 2.5d). By 1130 GMT on 19 January, half an hour before the last analysis time, a separate storm complex had formed south of the gulf and storms to the east of it covered a very large area (Fig. 2.1d).

The situation at upper levels is exemplified by the 200 hPa wind fields, geopotential, and potential temperature distribution on the 2 PVU potential vorticity (PV) surface<sup>1</sup>, shown in Fig. 2.6. The main features at 1800 GMT on 18 January are a broad trough in the east of the region and the ridge from an anticyclone in the west. The trough axis is oriented approximately north-northwest to south-southeast. A secondary and possibly significant feature is the east-west strip of low potential temperature centered along  $20^{\circ}\text{S}$  across northern Queensland and extending eastwards over the Tasman sea, even though

<sup>1</sup>1 potential vorticity unit, or  $\text{PVU} = 1.0 \times 10^{-6} \text{ s}^{-1}$ .

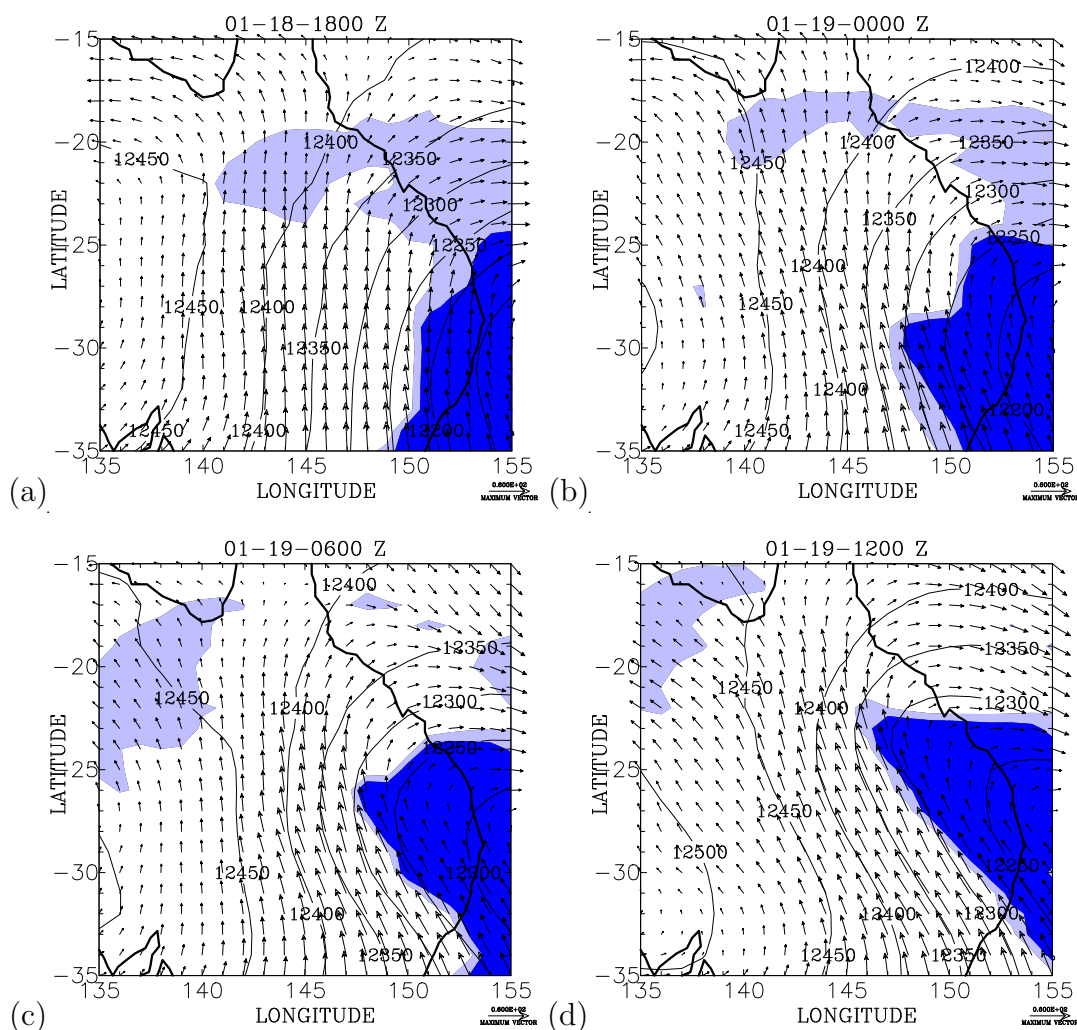


Figure 2.6: Regions of potential temperature on the 2 PVU surface less than 360 K (light shading) and less than 350 K (dark shading) at (a) 1800 GMT on 18 January, (b) 0000 GMT, (c) 0600 GMT, and (d) 1200 GMT on 19 January as indicated. The geopotential height of the 200 hPa surface (in m, contour interval 5 dm) and wind vectors on this surface are plotted also.

this has no recognizable signature in the geopotential height field at 200 hPa. The trough directs a primarily southerly airstream over the east of the continent at 200 hPa. By 0000 GMT on 19 January, the trough, as indicated by the potential temperature distribution on the  $PV = 2$  surface, had moved a little towards the northwest and the east-west strip of low potential temperature had moved equatorwards and weakened, but it lay approximately over the Burdekin region at this time. During the subsequent 12 h period the trough continued its northwestward progression as its axis rotated slightly counterclockwise and the potential temperature distribution on the  $PV = 2$  surface became elongated. Also the remnants of the east-west strip of low potential temperature on this surface moved northwestwards out of the region of interest. The evolution of the potential temperature distribution on the  $PV = 2$  surface would have been greatly influenced by the generation of anticyclonic PV at this level by the widespread convection that occurred during this period.

The upper-level situation in this case has some common features with the prototype of an anticyclonically-wrapping upper trough in the study of baroclinic wave systems (Thorncroft *et al.* 1993). The jet flow crossing the thinned upper-level trough and equatorward wave breaking are among them.

## 2.4 CAPE and CIN

CAPE and CIN are calculated at each grid point in the domain, assuming that air parcels are lifted pseudo-adiabatically from the surface. The distribution of CAPE at 1800 GMT on 18 January and at 0000 GMT, 0600 GMT and 1200 GMT on 19 January is shown in Fig. 2.7.

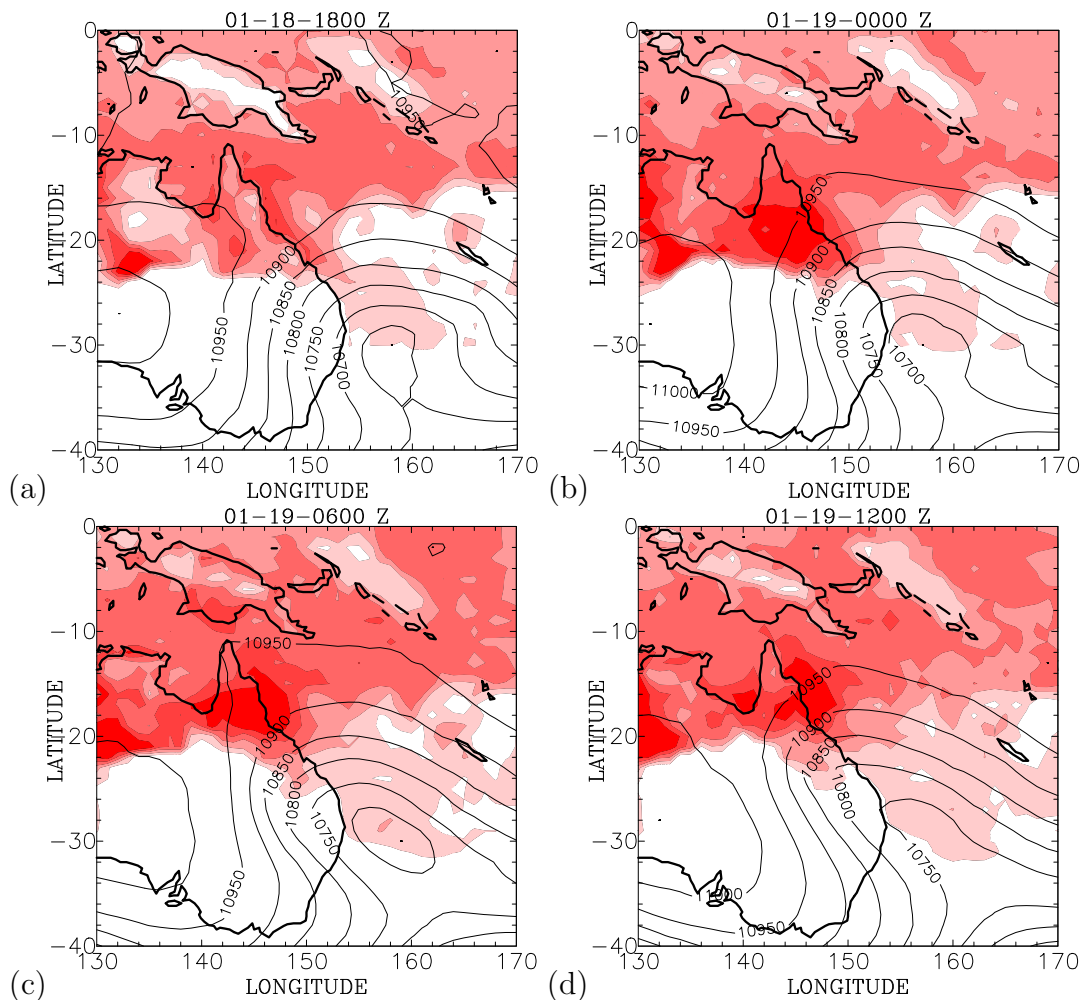


Figure 2.7: Distribution of CAPE for air parcels lifted pseudo-adiabatically from the surface at (a) 1800 GMT on 18 January, (b) 0000 GMT, (c) 0600 GMT, and (d) 1200 GMT on 19 January as indicated. The shading starts from  $1 \text{ kJ kg}^{-1}$  and increases in intervals of  $1 \text{ kJ kg}^{-1}$ .

At 1800 GMT on 18 January, which is around sunrise in the eastern part of the domain,

there are regions with significant CAPE (values over  $1 \text{ kJ kg}^{-1}$ ), mostly north of about  $23^\circ\text{S}$ , except over the ocean east of  $156^\circ\text{E}$ , where high values are mostly north of  $16^\circ\text{S}$ . There is a region with enhanced CAPE (values  $> 4 \text{ kJ kg}^{-1}$ ) along the Queensland coast at this time, one or two patches further inland with similar values and one patch near  $22^\circ\text{S}$ ,  $132^\circ\text{E}$  with values over  $5 \text{ kJ kg}^{-1}$ . South of  $23^\circ\text{S}$ , an area of high CAPE values is found on the northeastern side of the axis of the upper-level trough. By 0000 GMT on 19 January, CAPE values had increased markedly north of  $23^\circ\text{S}$ , with a significant increase over northeastern Queensland to the north and northwest of the trough axis, where values in some areas exceeded  $5 \text{ kJ kg}^{-1}$ . A contribution to this increase in CAPE south of  $16^\circ\text{S}$  arises from the further northwestward displacement of the upper-level trough that brought cold air to upper levels over northeastern Queensland (see Fig. 2.8a). The cold environmental temperature in the upper troposphere accompanying the approach of the upper-level trough is reflected in temperature fields at the 500 hPa level (Fig. 2.8). Typically an upper-level trough deeps over a region of cold advection. In fact the coldest temperatures over northeastern Queensland were seen in the 0600 GMT analyses. The situation here is a little different to that in the study by Juckes and Smith (2000), where the trough was assumed to be displaced perpendicular to its axis: here the trough was moving along its axis. By 0600 GMT on 19 January (4 pm local time), CAPE values had reached extremely large values ( $> 5 \text{ kJ kg}^{-1}$ ) over the lower half of Cape York Peninsula, the southeastern part of the gulf, and in the Burdekin region (Fig. 2.7c).

By 1200 GMT (10 pm local time), there had been a reduction in CAPE ( $\sim 1 - 2 \text{ kJ kg}^{-1}$ ) over the parts of northeastern Queensland where the storms occurred. Moreover, values of CAPE larger than  $1 \text{ kJ kg}^{-1}$  remained to about  $32^\circ \text{S}$  over the sea areas on the northeastern side of the trough (Fig. 2.7d).

The six hour time interval between analyses is too coarse to allow useful estimates to be made of the generation and consumption of CAPE by the storms in this case. However, the dramatic decrease of CAPE appears to coincide with the development of the thunderstorms and it would be reasonable to attribute the decline in CAPE to its consumption by deep convection. We show below that the ECMWF model did forecast convective precipitation in the region.

A question that remains is: how reliable are the CAPE values derived from the ECMWF analyses? The nearest radiosonde station to the Burdekin region is that at Townsville where a sounding was made at 2300 GMT on 18 January. The CAPE evaluated from this sounding is  $5.3 \text{ kJ kg}^{-1}$ , which compares with an average of  $5.1 \text{ kJ kg}^{-1}$  for the two grid points closest to Townsville in the ECMWF analysis at 0000 GMT on 19 January (Townsville lies almost equidistant from these grid points, where the CAPE values were  $4.7 \text{ kJ kg}^{-1}$  and  $5.4 \text{ kJ kg}^{-1}$ , respectively). The closeness of the potential temperature and moisture structure at Townsville in the model and in the observed sounding are indicated in Fig. 2.9a. The model was marginally warmer throughout much of the troposphere, but also a little drier, especially in the height range between 3 km and 4.8 km, factors that would oppose each other in the calculation of CAPE. In view of the known sensitivity of CAPE calculations to various factors, especially the low-level moisture content (e.g. Mapes and Houze, 1992, section 4a), we consider the agreement between the model and the observations at Townsville to be quite acceptable in this case.

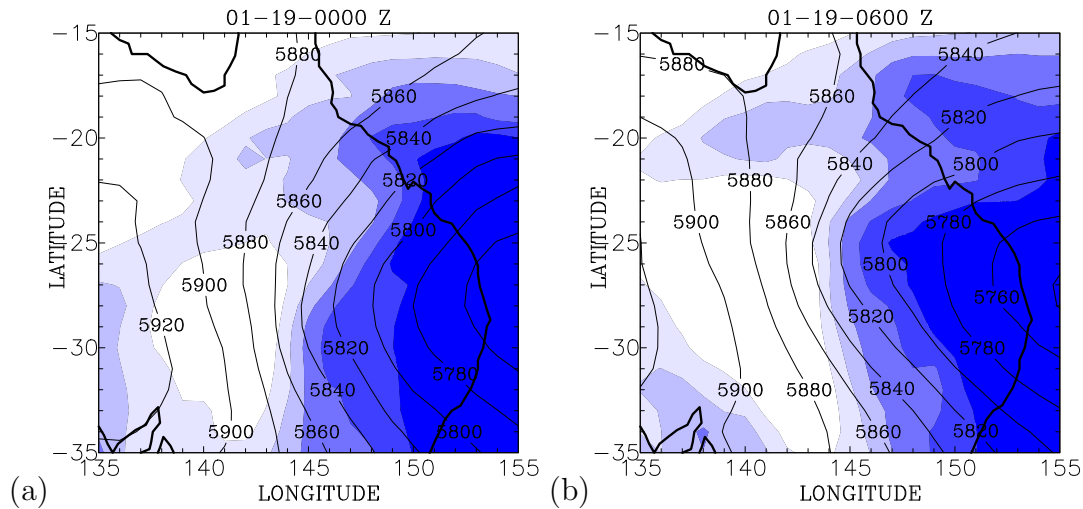


Figure 2.8: Temperature and geopotential height analyses at 500 hPa at (a) 0000 GMT and (b) 0600 GMT on 19 January. The shading starts from the value of 269 K and decreases in intervals of 1 K. Geopotential height is in m.

Regions of high CAPE do not necessarily lead to the occurrence of deep convection. First of all, air parcels must be lifted to their level of free convection against the CIN. In a case study in western Kansas, Colby (1984) found that deep convection occurred in a region where earlier the CIN was lowest. It is therefore of interest to examine the distributions of CIN prior to and following the onset of the Burdekin thunderstorms. However, in doing this it should be born in mind that the vertical resolution of the analyses may not be totally adequate to properly resolve strong inversion layers that might make a significant contribution to the CIN. One check that can be made is a comparison of CIN calculated from the Townsville radiosonde sounding at 2300 GMT on 18 January ( $26 \text{ J kg}^{-1}$ ) with those calculated at the nearest grid points to Townsville in the ECMWF analysis at 0000 GMT on 19 January ( $51 \text{ J kg}^{-1}$  and  $40 \text{ J kg}^{-1}$ , respectively). Based on these comparisons the model would appear to overestimate the CIN by a factor of about two. Since CIN is determined by the profile below the level of free convection (0.6 km for the observed profile and 0.8 km, 1.4 km for the grid point on  $146^\circ\text{E}$  and  $147^\circ\text{E}$  respectively), the dry slot in the ECMWF analysis referred to above would not affect the calculation of CIN.

The horizontal distributions of CIN at the same times as in Fig. 2.7 are shown in Fig. 2.10. At 1800 GMT on 18 January, there was significant inhibition (greater than  $100 \text{ J kg}^{-1}$ ) over much of the eastern and central part of the Australian continent and in a strip extending over the ocean between  $16^\circ\text{S}$  and  $20^\circ\text{S}$ . Six hours later, at 0000 GMT on 19 January, the CIN over much of central and southeastern Australia had been removed, while values over northeastern Queensland were significantly reduced, presumably because of strong surface heating during this period. The area of high CIN values ( $>100 \text{ J kg}^{-1}$ ) over the ocean had declined also. However, a region of significant inhibition remained in a region south of the gulf. The persistence of CIN north of about  $22^\circ\text{S}$  is probably because the soil is moist in this region in January. At 0600 GMT, areas with positive CIN persisted north of about  $21^\circ\text{S}$  and would have been enhanced by the low-level outflow from the storms in that region. In the evening (1200 GMT), CIN had again increased over the whole continent

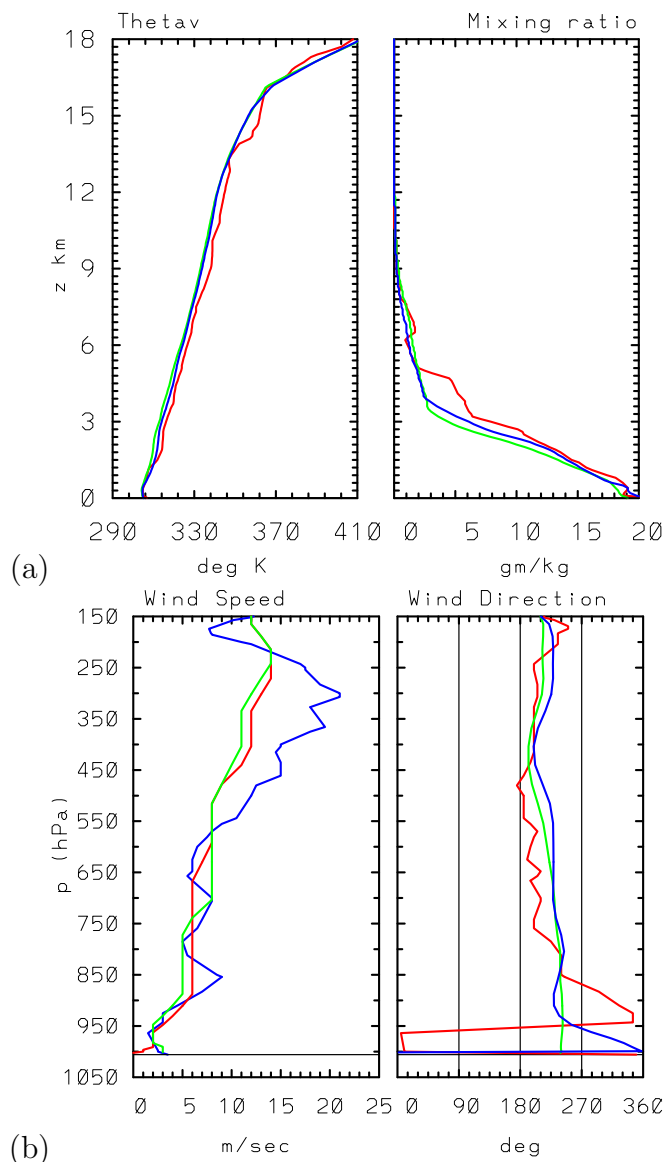


Figure 2.9: Comparison between the profiles of (a) virtual potential temperature, (b) water vapour mixing ratio, (c) wind speed, and (d) wind direction from the Townsville radiosonde sounding at 2300 GMT on 18 January 2001 (red line) and the nearest grid points to Townsville in the ECMWF analysis at 0000 GMT on 18 January 2001 (green line for the grid point on 146°E and blue line for that on 147°E.)

except, notably, in a region along the east coast of Queensland along the trough axis (Fig. 2.10d). Jukes and Smith (2000) showed that upper troughs can reduce the CIN in addition to enhancing the CAPE.

As noted above, the ECMWF model appears to overestimate the CIN, at least in this case, so that the presence in Fig. 2.10 of positive CIN values over the region where the storms developed must be seen as a deficiency of the model, suggesting that forecasts of CIN may not be accurate enough to be useful in indicating regions favourable to thunderstorm formation. Despite this, the model did forecast the existence of convective precipitation

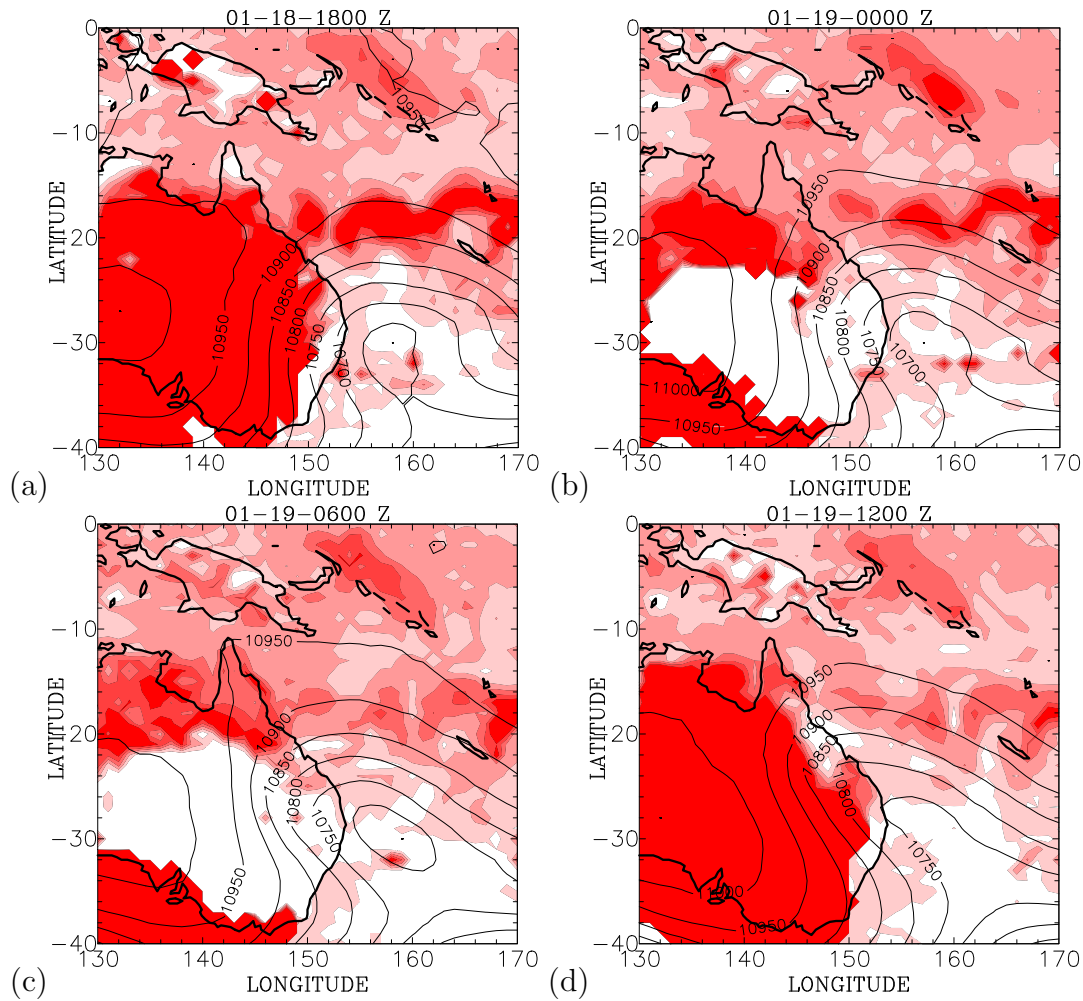


Figure 2.10: Distribution of CIN for air parcels lifted pseudo-adiabatically from the surface at (a) 1800 GMT on 18 January, (b) 0000 GMT, (c) 0600 GMT, and (d) 1200 GMT on 19 January as indicated. The shading starts from values exceeding  $20 \text{ J kg}^{-1}$  and becomes darker at intervals of  $20 \text{ J kg}^{-1}$ .

in the region of the thunderstorms (see Fig. 2.11), so that the CIN must have been removed in the region at some time between the six-hourly analysis times available for our study. We examined the ECMWF convective precipitation forecasts to determine the extent to which the model forecasts captured the storm systems. Figure 2.11 shows the predicted distribution of the 3-hourly accumulated convective precipitation at 0600 GMT and 0900 GMT, which should be compared with the storm locations in Fig. 2.1. Bearing in mind that the satellite imagery sees the upper-level cloud produced by the storms and that the convective precipitation represents a cumulative amount, there is a broad correspondence between the two figures except that the model did not capture the storm system immediately to the south of the gulf seen in Fig. 2.1d.

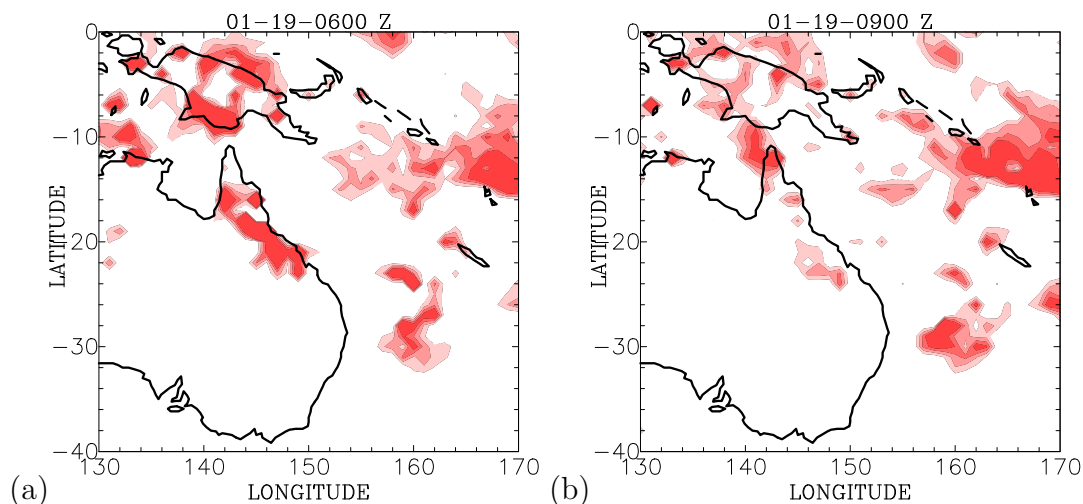


Figure 2.11: The 3-hourly accumulated convective precipitation forecasts from the ECMWF operational model at (a) 0600 GMT, and (b) 0900 GMT on 19 January. Precipitation amounts greater than 0.5 mm are shaded in an interval of 0.5 mm.

## 2.5 Low-level wind shear

It is well known that the development of severe thunderstorms is favored not only by high values of CAPE, but also by strong low-level wind shear. In a series of idealized numerical model calculations, Weisman and Klemp (1982, 1984) showed that the intensity and type of storm that develops in a particular environment depends on a convective parameter in the form of a bulk Richardson number,  $R$ , which they defined as the ratio of CAPE to  $0.5\bar{u}^2$ , where  $\bar{u}$  represents a difference between the density-weighted mean wind calculated over a 6 km depth and a representative surface layer (500 m) wind. This difference is a measure of the vertical wind shear in the lower half of the troposphere. Weisman and Klemp (1982) evaluated CAPE based on a 500 m mean temperature and moisture value for the particular sounding, but did not appear to include the effects of moisture on the buoyancy of an air parcel. They found that the optimal conditions for split storms occurred for values of  $R$  between 15 and 35. For  $R < 10$ , the shear is too strong to permit storm growth, while for  $R > 50$ , buoyancy is too strong relative to the shear to allow the necessary balances which produce strong split storms. Super-cell storms developed for values of  $R$  between 15 and 45, with the strongest storms measured by the ratio of maximum updraft in their model calculations to  $\sqrt{2CAPE}$  occurring at about  $R=18$ , while values of  $R > 45$  favored multi-cell storms (Weisman and Klemp 1984). The pressure-weighted vertical shear as defined by Weisman and Klemp (1982) calculated from the Townsville radiosonde sounding at 23 GMT on 18 January was about  $6 \text{ m s}^{-1}$ , a little less than the unweighted shear seen in Fig. 2.12. The Townsville rawinsonde sounding at 05 GMT on 19 January, about the time that the Burdekin thunderstorms began to develop, showed that the amount of shear did not change appreciably during the subsequent 6 hours. From the earlier radiosonde sounding, we calculated the average CAPE of parcels lifted from 100 m, 200 m, 300 m, 400 m and 500 m to approximate the calculation method of Weisman and Klemp (1982), but we included the contribution of moisture to the parcel buoyancy. The value obtained,  $2.9 \text{ kJ kg}^{-1}$ , gives

a value of  $R = 161$ . This value is well outside the range for supercell storms, but within the range for multicell storms and for other observed cases in the tropics listed in the table in Fig. 15.18 in Weisman and Klemp (1986). Since the CAPE increased during the 6 hours to 05 GMT on 19 January, the value of  $R$  in the neighbourhood of the storms would have been larger than 161, but still within the range for multicell storms. This value of  $R$  would explain the observed longevity and severity of the Burdekin storms.

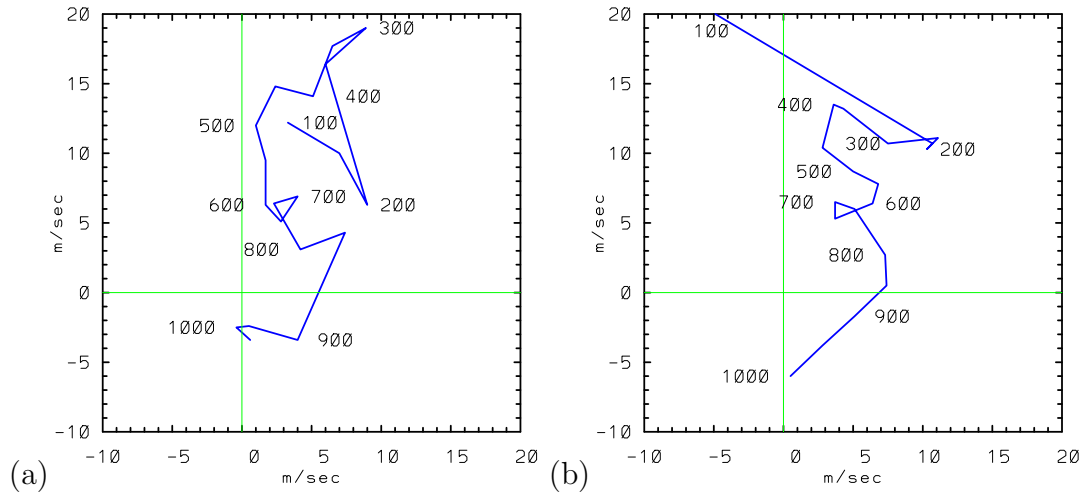


Figure 2.12: Wind hodographs based (a) on the Townsville radiosonde sounding at 2300 GMT on 18 January 2001, and (b) on the Townsville rawinsonde sounding at 0500 GMT on 19 January 2001. The numbers indicate the isobaric height in hPa. Data are plotted at the surface (1006 hPa in panel (a), 1000 hPa in panel(b)) and at 100 hPa intervals between 1000 hPa and 100 hPa.

## 2.6 Summary

Favourable conditions for the initiation of thunderstorms are known to be high CAPE, low CIN and strong low-level wind shear. The ECMWF analyses showed relatively high values of CAPE (values  $> 5 \text{ kJ kg}^{-1}$  for air parcels lifted from the surface) in the region where the Burdekin storms developed, but relatively low values of wind shear. The pressure-weighted wind shear at Townsville was less than  $10 \text{ m s}^{-1}$  in the lowest 6 km, near the time of the explosive development of thunderstorms, but the wind direction turned cyclonically with height. The high values of CAPE were clearly influenced by the cooling that accompanied the approach of an upper-level trough. The 0600 ECMWF analyses showed values of positive CIN in the region where the storms developed, but a comparison of the analyzed 0000 GMT CIN value at Townsville with the earlier 2300 GMT radiosonde sounding there showed that the ECMWF analysis overestimated the CIN by about a factor of two. The existence of ageostrophic low-level convergence towards an equatorward-moving trough over the Burdekin area would have contributed to a reduction of CIN before the generation of thunderstorms and would have indicated the potential for storm initiation in the region.

The bulk Richardson numbers of the storm environment, based on the 2300 GMT ra-

---

diosonde sounding at Townsville and that together with the 0500 GMT rawinsonde sounding, were well outside the range for supercell storms, but within the range for multicell storms and for other observed cases in the tropics (Weisman and Klemp 1986, Fig. 15.18). Thus, availability of these quantities to forecasters would have given an indication of the longevity and possible severity of the storms.

Despite analyzing positive values of CIN at 0600 GMT about the time that the storms developed, the ECMWF model did forecast convective precipitation in the general region of the storms at later times. Again, had these forecasts been available to forecasters, they would have given reasonable guidance about the occurrence of the Burdekin storms, but not of the storms that developed later to the south of the gulf.



# Chapter 3

## Tropical cyclones Theodore and Rewa

### 3.1 Introduction

If an upper-level trough advances, air below and ahead of it must ascend along raised isentropic surfaces and the ascending air cools adiabatically. In a theoretical calculation, the cooling associated with the approach of an upper-level trough increases convective instability (Juckes and Smith 2000). The purpose of this chapter is to investigate whether convective destabilization occurs in cyclone environment when an upper-level trough approaches a tropical cyclone. Two Australian tropical cyclones Rewa (January 1994) and Theodore (February 1994) are selected, since each tropical cyclone intensified rapidly as an upper-level trough approached them.

The data source for the synoptic analyses and for the calculation of the CAPE is the ECMWF reanalysis (ERA40), details of which are given in Appendix A. Data on the track and intensity of the cyclone are taken from the Australian Bureau of Meteorology's best track data set. Hourly Japanese Geostationary Meteorological Satellite (GMS) images are used to display the spatial distribution of cloud top temperature. The satellite images are utilized for a qualitative comparison between the observations of cloud-top temperature and the convective precipitation forecasts by the ECMWF model. The sea surface temperature (SST) was between 28.5°C and 29.5°C. The tracks of Rewa and Theodore are shown in Figure 3.1 during their intensification phase (red) and steady or decay phases (black).

This study focuses on the CAPE changes and the synoptic situation during the period of rapid intensification. Figure 3.2 shows time-series of minimum surface pressure and maximum 10-min sustained wind speed near the surface which characterizes the evolution of Theodore and Rewa. For the comparison, the abscissa shows the time elapsed from 1800 GMT on 23 February, which is 2 h after Theodore was named<sup>1</sup>, and from 0000 GMT on

---

<sup>1</sup>Since the intensity information at 1800 GMT does not exist in the Australian Bureau of Meteorology's best track data set, the information at this time is taken from Joint Typhoon Warning Centre's best track

14 January when Rewa began to re-intensify.

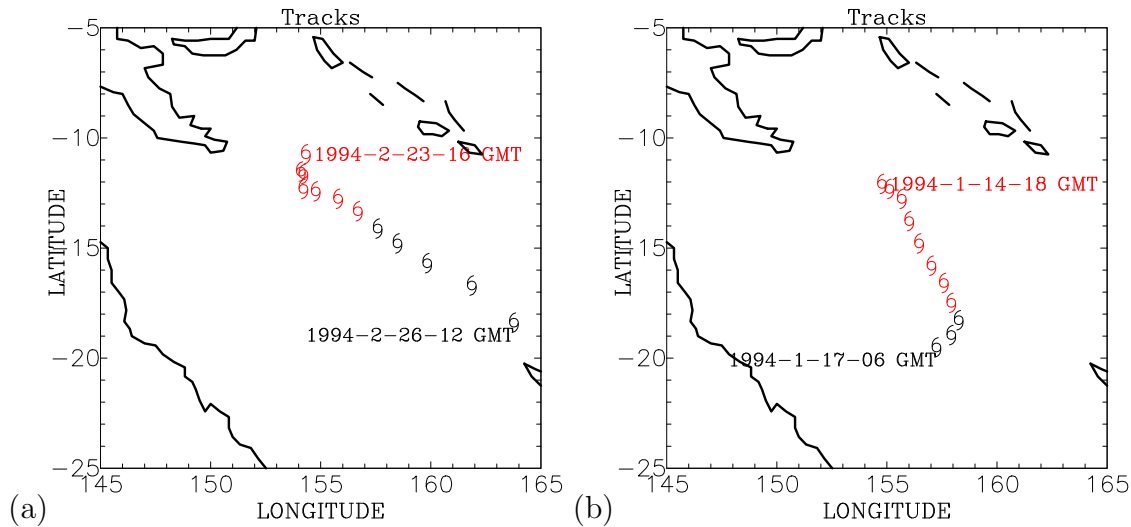


Figure 3.1: Track of Tropical Cyclone (a) Theodore and (b) Rewa depicted by the cyclone symbol. The time near the first symbol written in red is when Theodore was first named at 1600 GMT on 23 February 1994. The next symbol indicates the location of Theodore at 0000 GMT on 24 February 1994 and symbols are depicted every six hours thereafter. The track of Rewa is denoted by the cyclone symbol every six hours from 1800 GMT on 14 January 1994.

The layout of this chapter is as follows. In section 3.2, the quality of the model analysis is assessed in comparison to the best track and the satellite observation for Theodore. Synoptic conditions and changes of CAPE are discussed during the period of intensification. Likewise, convective instability changes and synoptic conditions in the case of Rewa are investigated in section 3.3. A summary of the results and conclusions of these case studies are presented in section 3.4.

## 3.2 Theodore

Theodore intensified during a 12-h period after it was named and reached hurricane intensity ( $> 33 \text{ m s}^{-1}$ ) at 0000 GMT on 24 February. It maintained a quasi-steady intensity of about  $45 \text{ m s}^{-1}$  for 12 h and then further intensified between 1800 GMT on 24 and 0600 GMT on 25 February. This study focuses on the CAPE changes and the synoptic situation between 0000 GMT on 24 and 0600 GMT on 25 February when the cyclone intensified rapidly and an upper-level trough approached the cyclone.

The skill of the ECMWF model in capturing the cyclone is assessed by examining the spatial distribution of MSLP (Fig. 3.3). At 0000 GMT on 24 February, there is a trough system with three separate lows located in the region 10-15°S, 135-150°E (Fig. 3.3a).

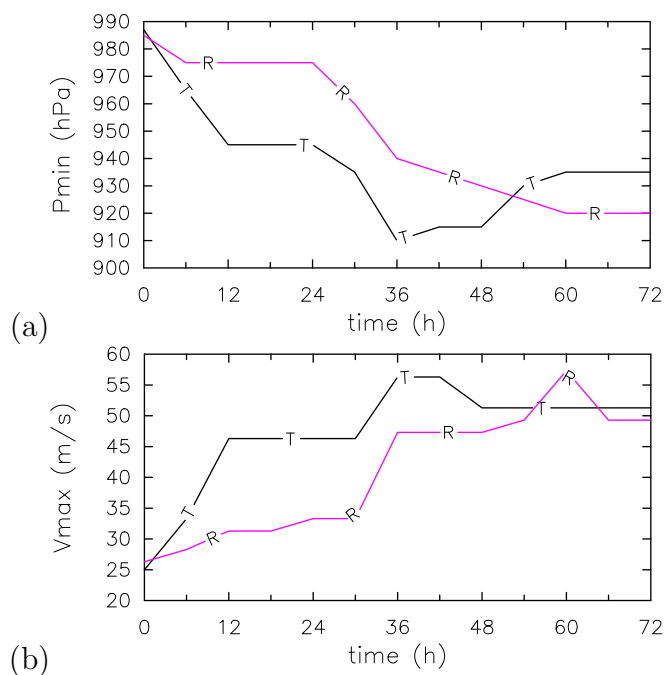


Figure 3.2: Time-series of (a) surface pressure minimum and (b) wind speed maximum. Theodore is denoted by T and Rewa by R. Details of this figure are explained in text.

The westernmost one is over the Australian continent, the second is over the Gulf of Carpentaria, and the third is about 300 km away from the cyclone position over the South Pacific Ocean. The error in positioning the cyclone at this time is larger than the horizontal grid size of the model. However, after 1800 GMT on 24 February, an MSLP minimum is collocated with the cyclone position within the error of the grid size of  $1^\circ$  ( $\sim 100$  km) (Fig. 3.3b, c, d). This indicates that the ECMWF analysis adequately captured the position of the tropical cyclone after Theodore reached hurricane intensity.

Convective precipitation forecasts from the ECMWF model are examined to assess the model's ability to represent the observed pattern of convection in the area of interest (Fig. 3.5). The forecasted precipitation pattern is compared with the satellite image in Figure 3.4, which shows the spatial distributions of cloud-top temperature at 0000 GMT on 24 and 25 February. The first satellite image shows that there are two prominent areas of low cloud-top temperature below  $-81^\circ\text{C}$ , to the east of Cape York peninsula (Fig. 3.4a). The right one coincides with the position of Theodore while the left one represents cloud clusters, which are related to a monsoon trough system (Hanstrum et al. 1996) (see Fig. 3.3). A local convective precipitation maximum is forecasted between those two prominent areas of low cloud-top temperature at 0000 GMT 24 February (Fig. 3.5a). As there is considerable error in positioning the cyclone at this time (see Fig. 3.3a) the convective precipitation forecast maximum is not collocated with the cyclone position. However, at 0000 GMT on 25 February the forecasted precipitation is concentrated in a broad area around the cyclone centre and its maximum is nearly collocated with the centre (Fig. 3.5b). The satellite image at this time shows that a spiral convective cloud band surrounds the cyclone, while the cloud top temperature minimum above the cyclone has decreased, consistent with the intensification of the cyclone (Fig. 3.3b). The comparisons between

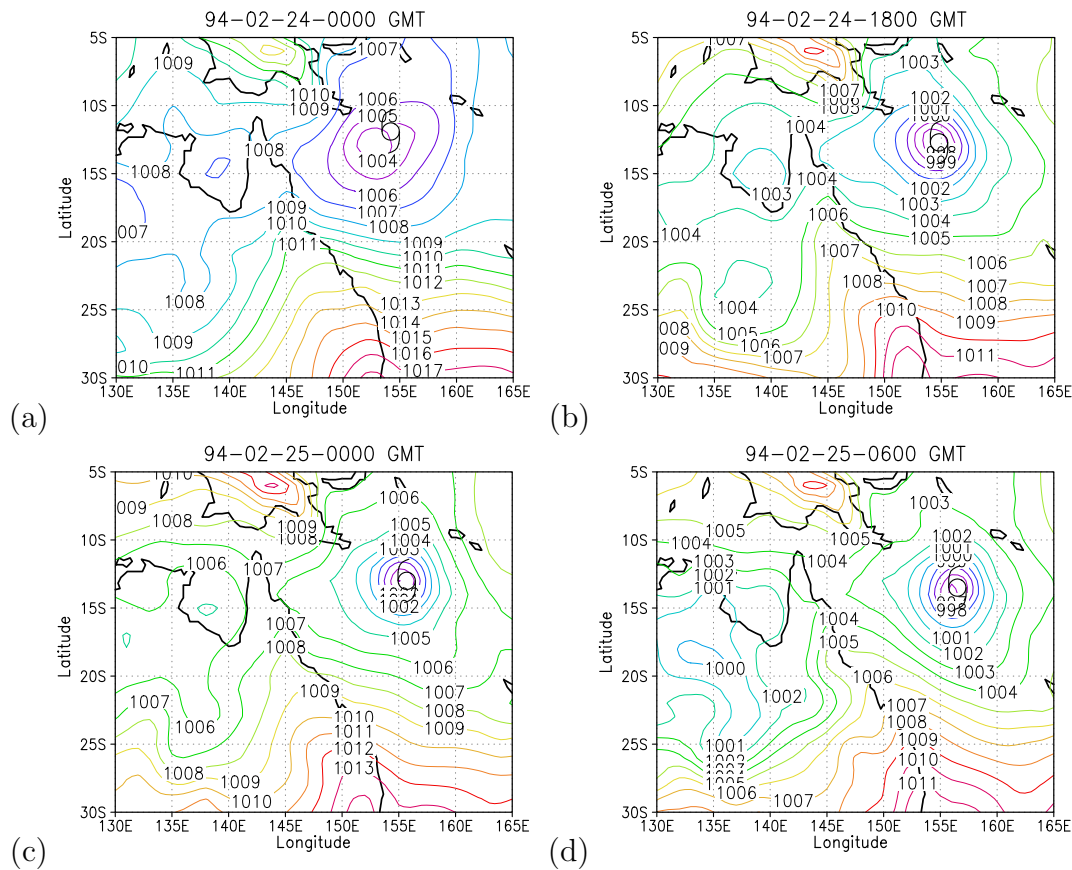


Figure 3.3: Mean sea level pressure over the Coral Sea at: (a) 0000 GMT and (b) 1800 GMT on 24 February 1994; (c) 0000 GMT and (d) 0600 GMT on 25 February. The contour interval is 1 hPa.

the forecasts and observations suggest that the model reasonably captures the observed pattern of convection around the cyclone centre. This better quality of forecasts at 0000 GMT on 25 than on 24 indicates that the model is more skillful in capturing the convective activity in the cyclone environment at this time. This improvement of the forecast quality is consistent with the decreased error in the positioning of the cyclone (see Fig. 3.3).

In order to determine how well the model captures the convective activity in the cyclone environment the convective scheme in the ECMWF model is examined. The scheme determines whether a grid point contains deep or shallow convection, based on the depth of the convectively-unstable layer. If the convective cloud depth exceeds 200 hPa, the convection is deemed to be deep convection, while shallow convection has depth lower than this threshold (Gregory *et al.* 2000). The convective mass flux at cloud base is estimated by a *closure* assumption. The closure for the deep convection is based on the concept that convection acts to reduce CAPE towards zero over a certain time-scale. This closure was suggested first in the context of cumulus parametrization for use in meso-scale models (Fritsch and Chappell 1980), but it works reasonably at the much coarser resolution of the ECMWF model (Gregory *et al.* 2000). Gregory *et al.* suggested that this closure gives smoother rainfall patterns in the tropics with less peak rainfall amount and that the area of precipitation is more extensive than that produced by a moisture convergence closure.

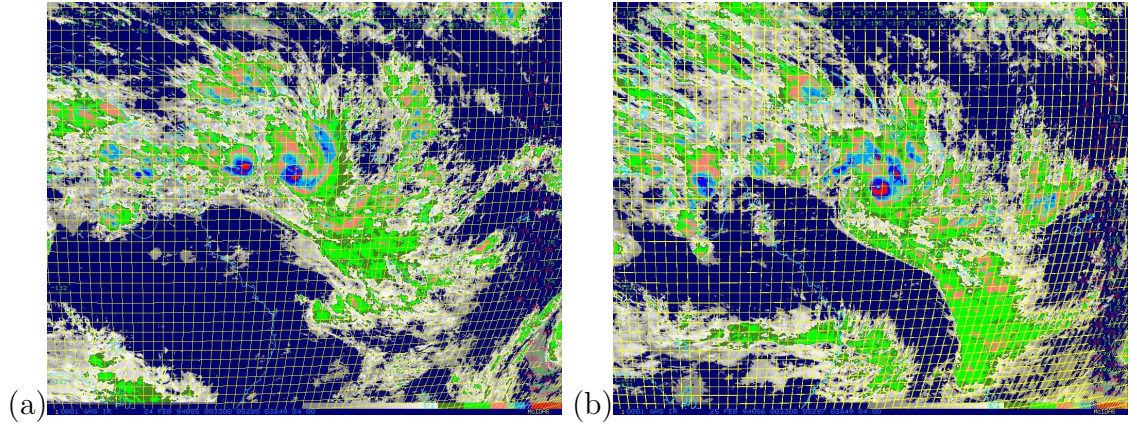


Figure 3.4: Enhanced infrared satellite imagery at (a) at 0000 GMT on 24 February, (b) 0000 GMT on 25 February, showing the evolution of the severe thunderstorms from the early cells. The color shading codes are 1)  $-31$  to  $-41^\circ\text{C}$  dark green; 2)  $-42$  to  $-53^\circ\text{C}$  light green; 3)  $-54$  to  $-63^\circ\text{C}$  pink; 4)  $-64$  to  $-69^\circ\text{C}$  cyan; 5)  $-70$  to  $-75^\circ\text{C}$  light blue; 6)  $-76$  to  $-80^\circ\text{C}$  dark blue; 7)  $\leq -81^\circ\text{C}$  red. The map projection is the Lambert conformal conic projection, approximately ranging from  $3^\circ\text{N}$  to  $37^\circ\text{S}$  and from  $131^\circ\text{E}$  to  $182^\circ\text{E}$ .

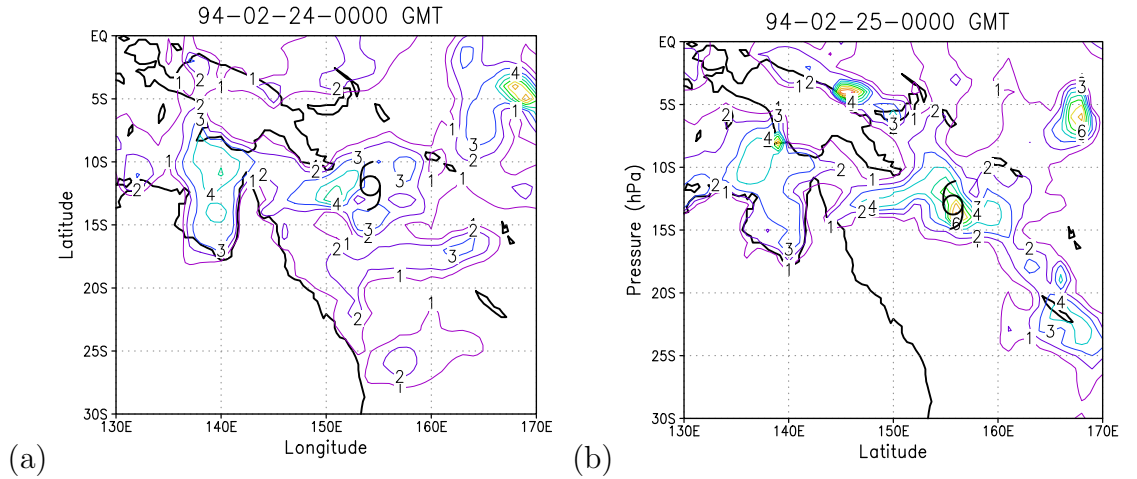


Figure 3.5: The 3-hourly accumulated convective precipitation forecasts from the ECMWF model at: (a) 0000 GMT on 24 and (b) 0000 GMT on 25 February. The contour interval is 1 mm.

The CAPE consumption is related to upward mass fluxes in the ECMWF model by

$$M_B^{UD} = \frac{\frac{CAPE}{\tau}}{\int g(\eta^{UD} - \alpha\eta^{DD}) \left\{ \frac{1}{T} \left( \frac{\partial T}{\partial z} + \frac{g}{c_p} \right) + \frac{0.608}{(1+0.608\bar{q})} \frac{\partial \bar{q}}{\partial z} \right\} dz} \quad (3.1)$$

where  $M_B^{UD}$ ,  $c_p$ ,  $g$ ,  $\tau$ ,  $\alpha$ ,  $\eta^{UD}$ , and  $\eta^{DD}$  are the mass flux at the base of the updraft, specific heat at constant pressure, the acceleration due to gravity, the time scale of the CAPE consumption, the amount of dilution of the updraft, and functions that describe variation

of mass flux with height in the updraft ( $UD$ ) and downdraft ( $DD$ ), respectively (Gregory *et al.* 2000). The variation of the mass fluxes are derived from an entraining/detraining plume model of convection. The initial mass flux at the top of the downdraft is taken to be proportional to the mass flux at the base of the updraft ( $M_T^{DD} = -\alpha M_B^{UD}$ ), where  $\alpha$  is 0.3. The over-bar denotes an average value of cumulus elements. Equation (3.1) indicates that the upward mass flux for convection increases with increasing CAPE, or with decreasing  $\tau$ . The value of  $\tau$  is related to the vertical velocity while tendency of CAPE can be estimated by

$$\frac{\partial CAPE}{\partial \tau} \simeq (T - T_{LNB}) \frac{\partial s}{\partial \tau} - \int_Z^{Z_{LNB}} \left( \frac{g\dot{Q}}{c_p T} - \frac{g}{\theta} V_r \cdot \nabla \theta - N^2 \omega \right) dz, \quad (3.2)$$

where  $N$ ,  $\dot{Q}$ ,  $\theta$ ,  $V_r$ ,  $s$ , and  $\omega$  are the buoyancy frequency of unsaturated air, radiative cooling rate, potential temperature, horizontal velocity, moist entropy<sup>2</sup> in the boundary layer, and the large-scale vertical velocity, respectively (Emanuel 1994). This equation indicates that the CAPE increases as the moist entropy of the air in the boundary layer increases or as the temperature of the troposphere above the boundary layer decreases. The CAPE increases also if the temperature difference between the boundary layer and the level of neutral buoyancy increases.

The main interest of this study is to investigate whether the CAPE in the cyclone environment increases during the approach of the upper-level trough. The situation at upper levels is exemplified by the potential vorticity (PV) at the 200 hPa-level (Fig. 3.6). The trough is represented by the area of negative PV in the Southern Hemisphere<sup>3</sup>. The area of PV less than -0.5 PVU extends to about 14°S, where its surroundings of positive PV make it anomalous. The trough axis is oriented approximately north-northwest to south-southeast. The cyclone centre is about 500 km away from the area of PV less than -0.5 PVU, around 14°S, 150°E at 0600 GMT on 24 February (Fig. 3.6a). The PV anomaly extends northwestwards with time. By 1800 GMT on 24 February, the distance between the cyclone and the area of PV less than -0.5 PVU has decreased (Fig. 3.6c). However, the area of the PV less than -1.0 PVU has narrowed to the south of the cyclone, which indicates a decrease of the scale of the upper-level trough during the intensification phase of the cyclone. The upper-level situation in this case has some common features with the prototype of an anticyclonically-wrapping upper-level trough in the study of baroclinic wave systems (Thorncroft *et al.* 1993). The equatorward wave extension and thinning of the PV anomaly are amongst them. On the other hand, Molinari *et al.* (1995) suggested that such a scale decrease of the trough is influenced by the low PV anomaly associated with outflow from the cyclone. In the theoretical calculations of CAPE by Juckes and Smith (2000), the CAPE increases with increasing strength and width of the trough. Therefore, the decreasing scale of the PV anomaly implies that an increase of CAPE associated with the trough, if any, would be diminishing during the period of cyclone intensification.

<sup>2</sup>The moist entropy is defined by  $s = c_p \ln T + \frac{L_v r}{T} - R \ln \frac{p}{p_0}$ , where  $T$  and  $p$  are temperature and pressure,  $p_0$  a reference pressure (1000 mb),  $r$  the mixing ratio,  $L_v$  the heat of vaporization,  $c_p$  the heat capacity at constant pressure, and  $R$  gas constant.

<sup>3</sup>The sign of PV for the trough in the Northern Hemisphere is positive.

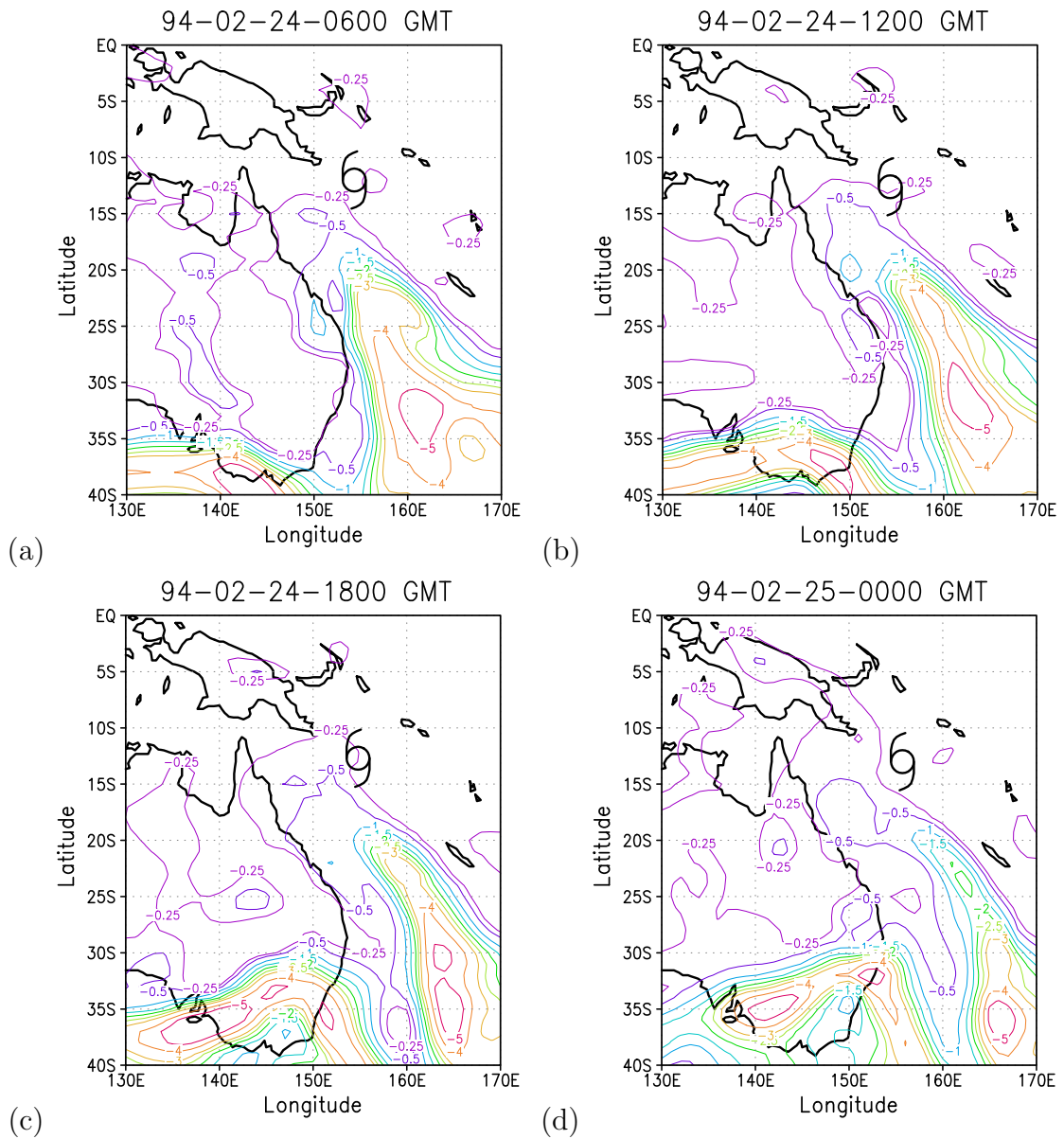


Figure 3.6: Potential vorticity (PVU) at 200 hPa at: (a) 0600 GMT, (b) 1200 GMT, (c) 1800 GMT on 24; and (d) 0000 GMT on 25 February.

The ascending air below and ahead of the upper-level trough is assumed to cool adiabatically if the atmosphere is unsaturated. At 1800 GMT on 24 February, cooler air has extended to the east of the cyclone, about 400 km away from the cyclone centre (Fig. 3.7a). However, during the next 6-h period the temperature has increased in the region and the area of cold air narrowed (Fig.3.7b). Compared to the decrease of the temperature at 500 hPa in the Burdekin thunderstorm case, the temperature decrease in the region is minimal. This difference of the temperature field between the thunderstorm and Theodore cases indicates that the influence of the cooling on the CAPE in the Theodore case is relatively small.

The middle-tropospheric moisture field is examined during the approach of the trough to

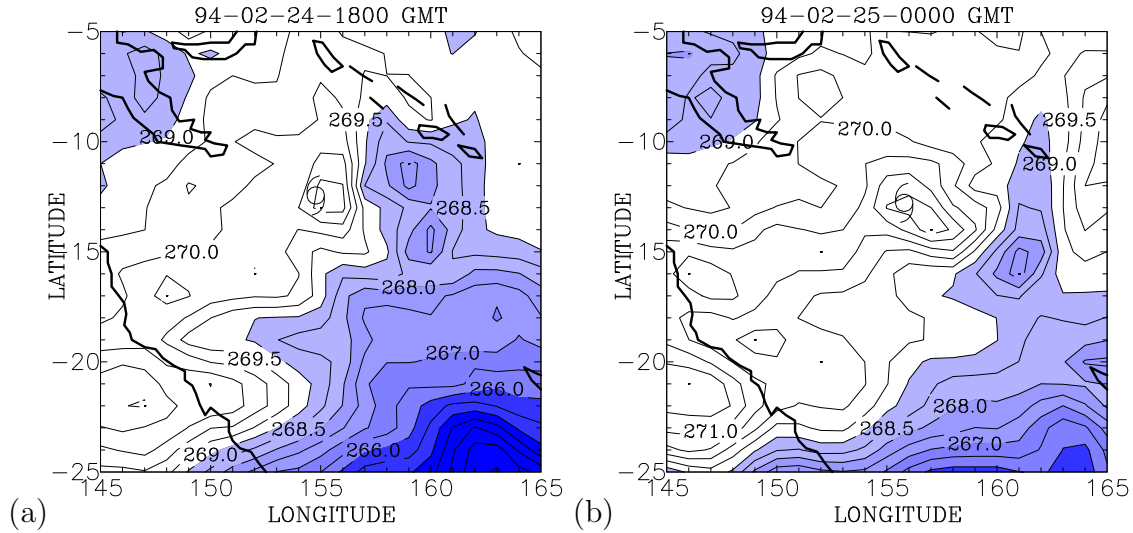


Figure 3.7: Temperature (K) at 500 hPa at: 1800 GMT (a) on 24 (b) 0000 GMT on 25 February. The area of temperature below 269 K is shaded and the contour interval is 0.5 K.

investigate whether a decrease of the moisture content in the middle troposphere might influence deep convection in the region of dry air advection. A decrease of the mixing ratio in the middle-troposphere commonly occurs when an upper-level trough turns anticyclonically and extends equatorwards, bringing stratospheric air with low water vapour into the upper-troposphere (Vaughan and Polvani 2000). If sufficient subsidence takes place and the subsiding dry air in the middle-troposphere is injected into the Tropics with a southerly wind component in the Southern Hemisphere, the intrusion of the dry air is likely to inhibit the development of deep convection (Yoneyama and Parsons 1999).

Figure 3.8 shows the spatial distribution of the mixing ratio and its advection at 500 hPa. Dry air is advected from higher latitudes towards the western side of the cyclone (Fig. 3.8b, d). The dry air advection intensifies and the mixing ratio decreases with time on the western side of Theodore. Deep convection is suppressed in the region below the extremely dry air, which is attested by the downward vertical motion in the re-analysis of the ECMWF model and the scarcity of convective clouds in the region on satellite image.

The vertical profiles of mixing ratio  $r$ , temperature  $T$ , and virtual temperature  $T_v$ , are examined to assess the effect of the dry air above the boundary layer on convective instability. Figure 3.9 shows that above 1 km in the vertical,  $r$  is much lower at  $154^\circ\text{E}$  than that at  $156^\circ\text{E}$  although the values are nearly identical below 1 km. The temperature sounding shows that the temperature between 2 and 5 km at  $154^\circ\text{E}$  is about 1-2 K lower than that in this layer at  $156^\circ\text{E}$  (Fig. 3.9b). The lower temperature at  $154^\circ\text{E}$  coincides with the lower  $T_v$  in the layer 2 km-5 km (Fig. 3.9a). However, the effect of the drier air above 1 km at  $154^\circ\text{E}$  on  $T_v$  is relatively small. For example, the difference of mixing ratio at the level 2.5 km between the two positions is  $2.3 \text{ g kg}^{-1}$  and the temperature difference is 1.2 K. This makes the 1.6 K-difference of  $T_v$  between the two positions. Only 0.4 K of the difference is attributed to the dryness. Moreover, the contribution of the dryness to the decreases of the virtual temperature diminishes with the height. The effect of the dry air on convective

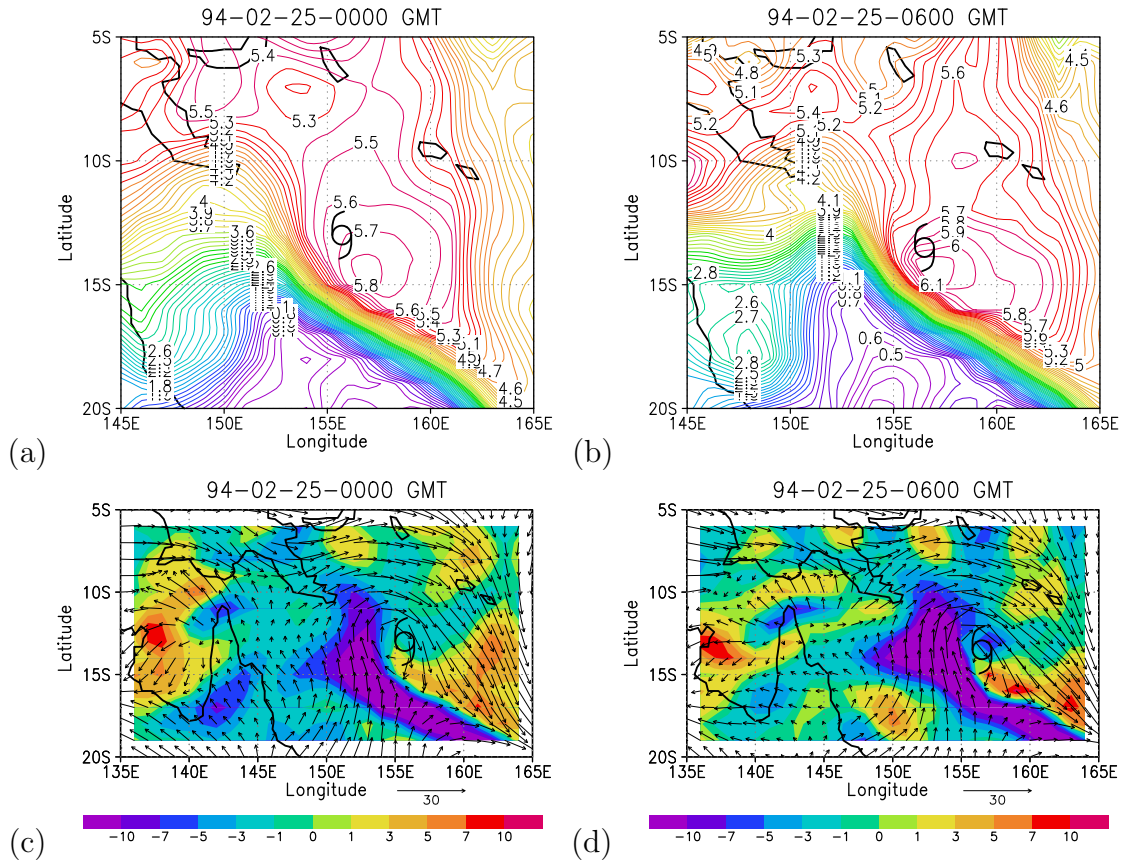


Figure 3.8: The mixing ratio ( $\text{g kg}^{-1}$ ) at 500 hPa at: (a) 1800 GMT on 24 and (b) 0000 GMT on 25 February; and horizontal mixing ratio advection ( $10^{-5} \text{ g kg}^{-1} \text{ s}^{-1}$ ) at each time (lower panels).

instability is minimal.

The boundary-layer moist entropy in Equation (3.2) is examined to assess its influence on the CAPE. The moist entropy,  $s$  is related to the equivalent potential temperature,  $\theta_e$ , by  $s = c_p \log \theta_e$ . The empirical formula used for the calculation of  $\theta_e$  by assuming a pseudo-adiabatic process is

$$\theta_e = T_k \left( \frac{1000}{p} \right)^{0.2854(1-0.28 \times 10^{-3} r)} \times \exp \left[ \left( \frac{3.376}{T_L} - 0.00254 \right) \times r (1 + 0.81 \times 10^{-3} r) \right], \quad (3.3)$$

where  $r$  is the mixing ratio at a certain level, and  $T_L$  is the absolute temperature at the LCL<sup>4</sup> (Bolton 1980). This equation indicates that  $\theta_e$  is dependent on  $r$ . Patterns of  $\theta_e$  and  $r$  are nearly identical to each other and the maximum of  $\theta_e$  and  $r$  are nearly collocated with the cyclone centre (Fig. 3.10). The mixing ratio and  $\theta_e$  increase with time within a radius of about 300 km, while there is no discernable increase beyond this radius (Fig.

<sup>4</sup>Altitude at which saturation occurs through adiabatic expansion.

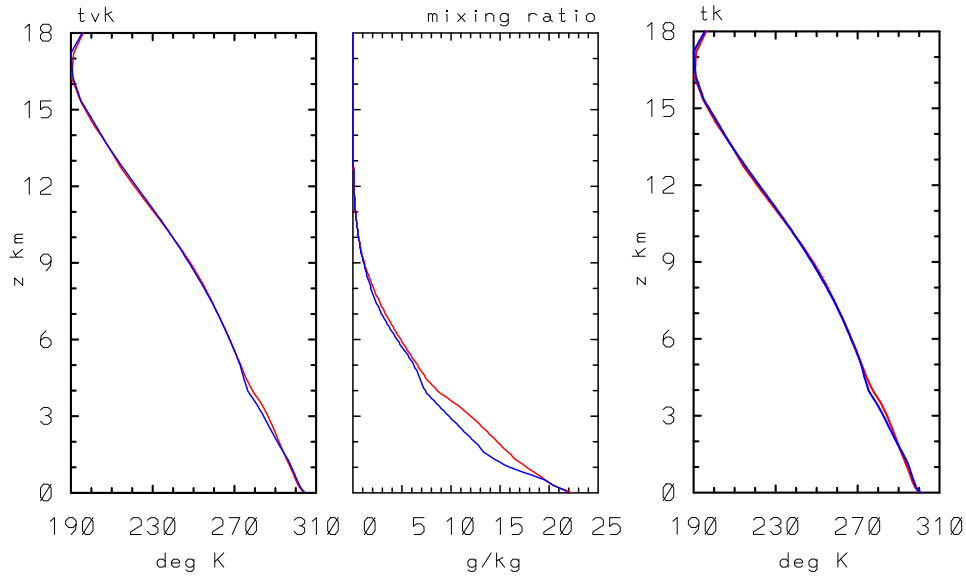


Figure 3.9: The vertical sounding of (a) virtual temperature (K), mixing ratio ( $\text{g kg}^{-1}$ ) and (b) temperature (K) at:  $13^{\circ}\text{S}$ ,  $154^{\circ}\text{E}$  (blue line) and  $13^{\circ}\text{S}$ ,  $156^{\circ}\text{E}$  (red line) at 0000 GMT on 25 February.

3.10b, d). This increase of the mixing ratio would contribute to an increase of the CAPE in the region assuming Equation (3.2).

The spatial distribution of the CAPE in the cyclone environment is shown in Figure 3.11. CAPE is calculated at each grid point in the domain on the assumption that air parcels are lifted pseudo-adiabatically from the surface since the model forecasts precipitation in the area of interest. The distribution of the CAPE is similar to that of the boundary-layer mixing ratio and equivalent potential temperature (see Fig. 3.10). The CAPE is persistently large ( $> 3 \text{ kJ kg}^{-1}$ ) in the vicinity of the cyclone during the intensification phase. At 0000 GMT on 25 February, CAPE becomes more than  $4 \text{ kJ kg}^{-1}$  within a radius of about 300 km, consistent with the increase of the boundary-layer mixing ratio and  $\theta_e$  in the region (Fig. 3.11c). The similar distribution of the CAPE to that of the boundary-layer mixing ratio indicates that the tendency of moisture content in the boundary layer dominates over other terms in Equation (3.2). The boundary layer mixing ratio is related to  $\theta_e$  in Equation (3.3) so that the CAPE distribution is also similar to that of the boundary-layer  $\theta_e$ . Mapes and Houze (1992) examined the sensitivity of CAPE to boundary-layer  $\theta_e$  and they suggested the importance of the boundary-layer  $\theta_e$  on the CAPE. Williams and Renno (1993) proposed that there is a linear relationship between boundary-layer  $\theta_e$  and CAPE for tropical soundings.

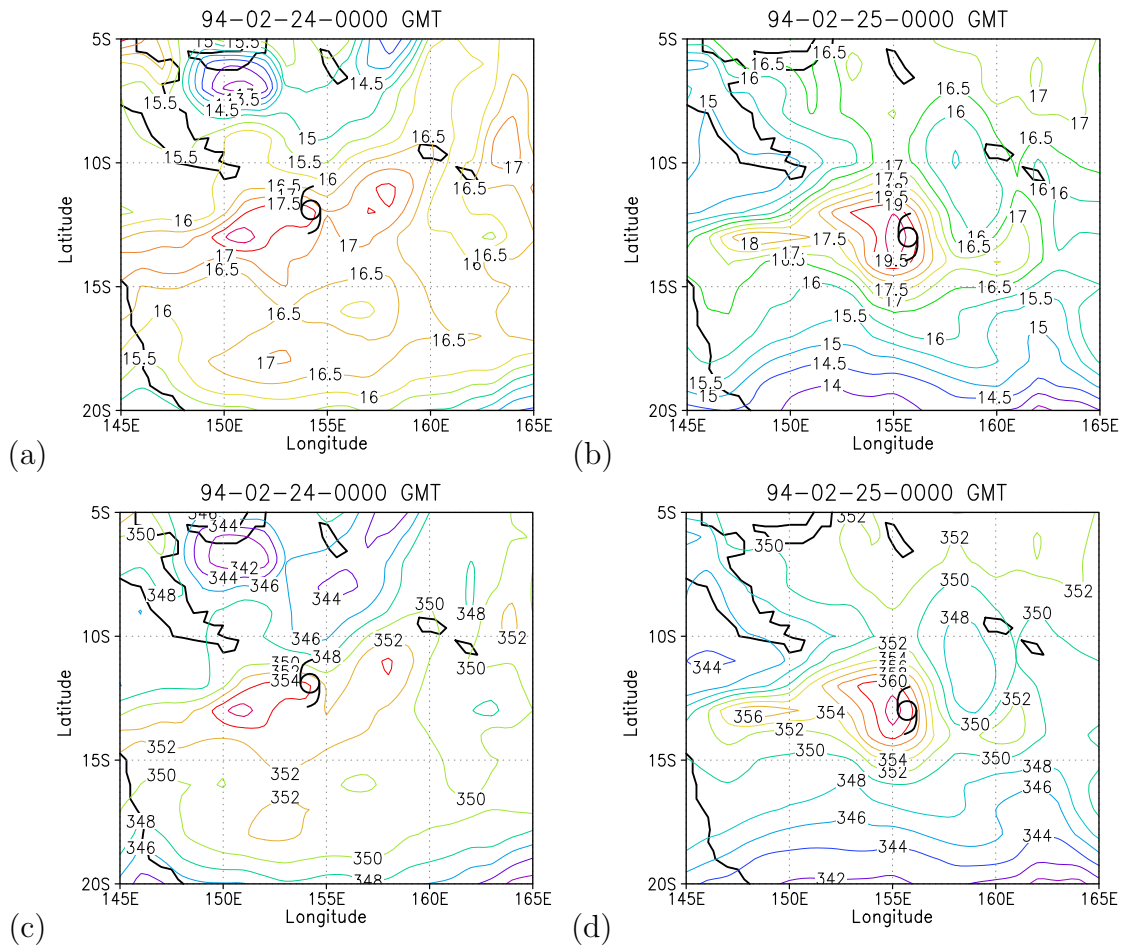


Figure 3.10: The mixing ratio ( $\text{g kg}^{-1}$ ) at 925 hPa at 0000 GMT on (a) 24 and (b) 25 February; and equivalent potential temperature (K) at the same level and time (lower panels).

### 3.3 Rewa

The investigation of the Rewa case aims to examine whether the influence of the upper-level trough on CAPE in the cyclone environment is minimal as in the Theodore case.

A brief overview of the evolution of Rewa is as follows. Rewa intensified gradually and reached hurricane intensity at 0600 GMT on 15 January (Fig. 3.2b). Then it intensified rapidly and the wind speed maximum reached  $45 \text{ m s}^{-1}$  at 1200 GMT on 15 January. The wind speed peaked at  $55 \text{ m s}^{-1}$  at 1200 GMT 16 January, 60 h after the state of re-intensification. During this intensification period, an upper-level trough approached from the west towards the cyclone (see Fig. 3.14). This study focuses on convective instability changes and synoptic conditions when the cyclone intensified rapidly between 0600 GMT on 15 and 0600 GMT on 16 January (see Fig. 3.2).

The skill of the ECMWF model in capturing Rewa is assessed by comparing the spatial distribution of the cloud-top temperature in infra-red satellite images (Fig. 3.12) and the

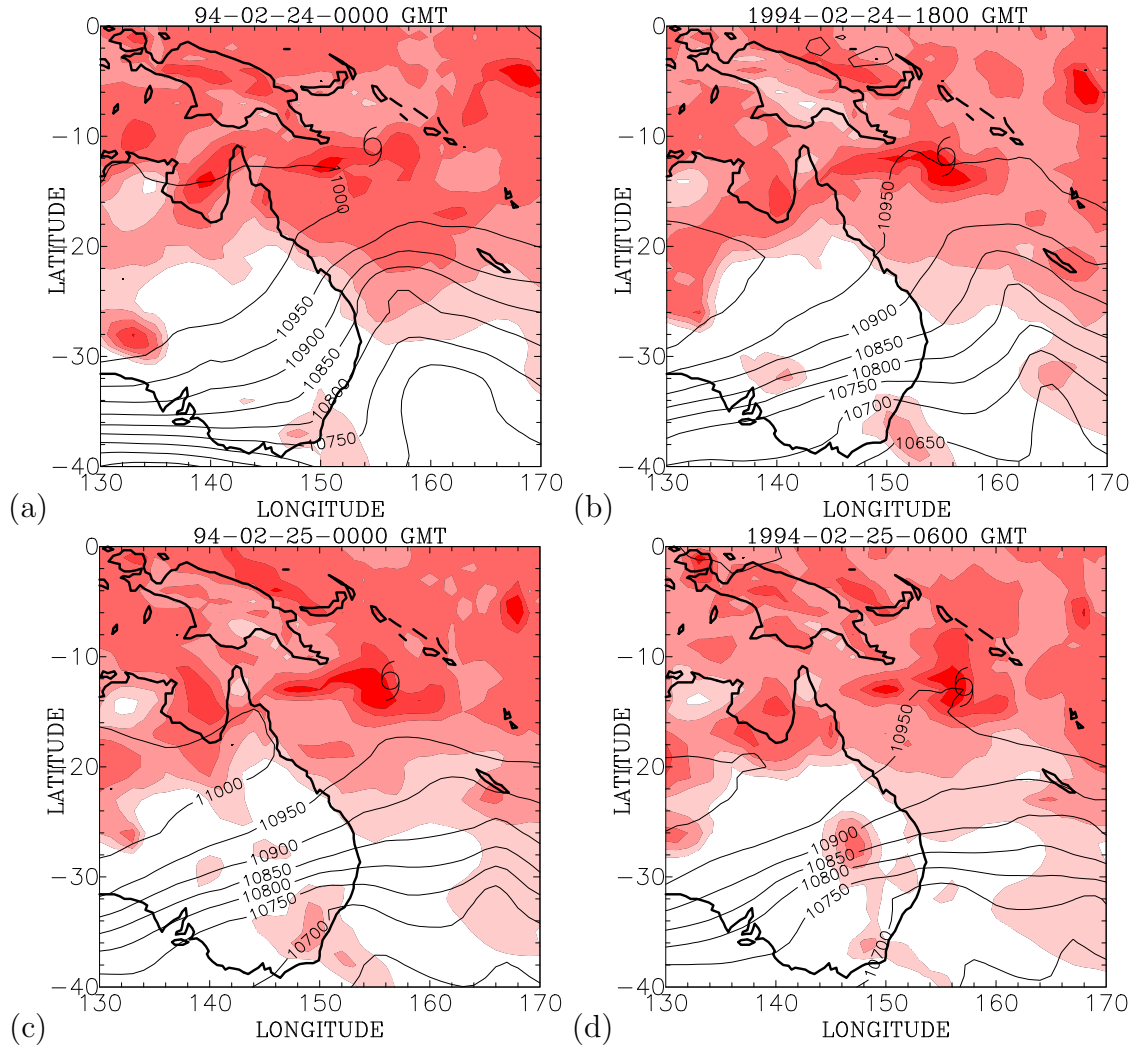


Figure 3.11: Distribution of CAPE for air parcels lifted pseudo-adiabatically from the surface at times as indicated on panels. The shading starts from  $1 \text{ kJ kg}^{-1}$  and increases in intervals of  $1 \text{ kJ kg}^{-1}$ .

convective precipitation forecasts from the ECMWF model (Fig. 3.13). In the first image (Fig. 3.12a) there are clusters of convective clouds to the north of the Cape York Peninsula and in the area around the tropical cyclone centre, which was located at  $13^\circ\text{S}$ ,  $156^\circ\text{E}$  at 0600 GMT on 15 January. On the other hand, the convective precipitation forecast at this time shows that there is little precipitation in the region of the cloud clusters to the north of the Peninsula. Instead, a local maximum precipitation is forecasted about 250 km away to the west of the position of Rewa and convective precipitation is distributed in a broad area around the cyclone (Fig. 3.13a). The second satellite image shows that the cloud-top temperature has decreased around the cyclone centre as Rewa has intensified between 0600 GMT on 15 and 16 January (Fig. 3.12b). The local maximum precipitation is forecasted to the northwest of the cyclone, about 250 km away from the centre, and the amount of the forecasted convective precipitation has increased in a broad area around the cyclone (Fig. 3.13b). In the Theodore case, the distance between the position of forecasted maximum convective precipitation and the cyclone was smaller than the model grid-size,

about 100 km. However, the maximum convective precipitation is located about 250 km ( $\sim$  twice of the grid size) away from the cyclone centre in the Rewa case. The larger error of the ECMWF forecasts in positioning Rewa than Theodore indicates that convective activity in the case of Rewa is not captured by the ECMWF model as skillfully as in the Theodore case. Despite the error in positioning Rewa, the ECMWF model analysis still contains useful information about the broad-scale synoptic conditions to allow the analysis of CAPE in the cyclone environment.

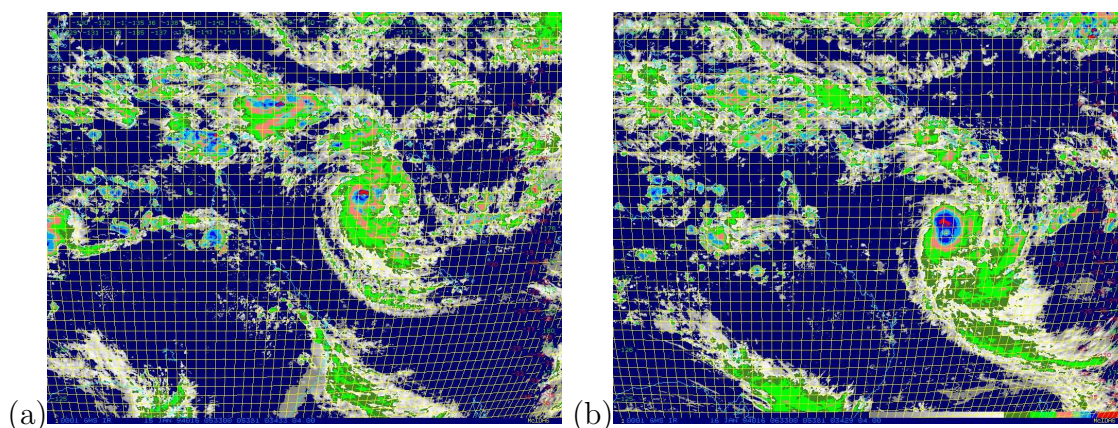


Figure 3.12: Enhanced infrared satellite imagery at (a) at 0600 GMT on 15 January, (b) 0600 GMT on 16 January, showing the evolution of the severe thunderstorms from the early cells. The color shading codes are 1)  $-31$  to  $-41^{\circ}\text{C}$  dark green; 2)  $-42$  to  $-53^{\circ}\text{C}$  light green; 3)  $-54$  to  $-63^{\circ}\text{C}$  pink; 4)  $-64$  to  $-69^{\circ}\text{C}$  cyan; 5)  $-70$  to  $-75^{\circ}\text{C}$  light blue; 6)  $-76$  to  $-80^{\circ}\text{C}$  dark blue; 7)  $\leq -81^{\circ}\text{C}$  red. The map projection is the Lambert conformal conic projection, approximately ranging from  $3^{\circ}\text{N}$  to  $37^{\circ}\text{S}$  and from  $131^{\circ}\text{E}$  to  $182^{\circ}\text{E}$ .

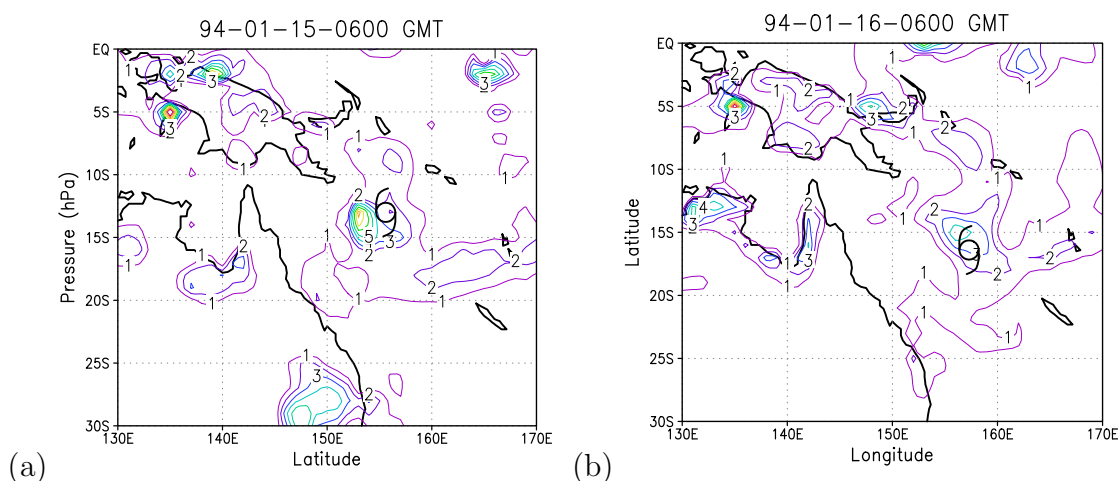


Figure 3.13: The 3-hourly accumulated convective precipitation forecasts from the ECMWF model at (a) 0600 GMT on 15, and (b) 0600 GMT on 16 January. The contour interval is 1 mm.

Figure 3.14 shows the situation at the upper levels exemplified by the potential vorticity (PV) at the 200 hPa-level. The area of PV less than  $-0.5$  PVU extends to the Gulf of

Carpentaria and is about 1800 km away from the cyclone at 0000 GMT on 15 February (Fig. 3.14a). The trough axis is oriented approximately north-northwest to south-southeast. The PV anomaly extends equatorward with time as in the Theodore case (Fig. 3.14b). The PV anomaly approaches Rewa, while the cyclone moves southwards (Fig. 3.14c, d). The area of PV less than  $-0.5$  PVU is about 500 km away from the cyclone centre, around  $17^{\circ}\text{S}$ ,  $156^{\circ}\text{E}$  at 0600 GMT on 16 January (Fig. 3.14d). The strength and scale of the PV anomaly decreases during the period of cyclone intensification as observed in the Theodore case (see Fig. 3.6).

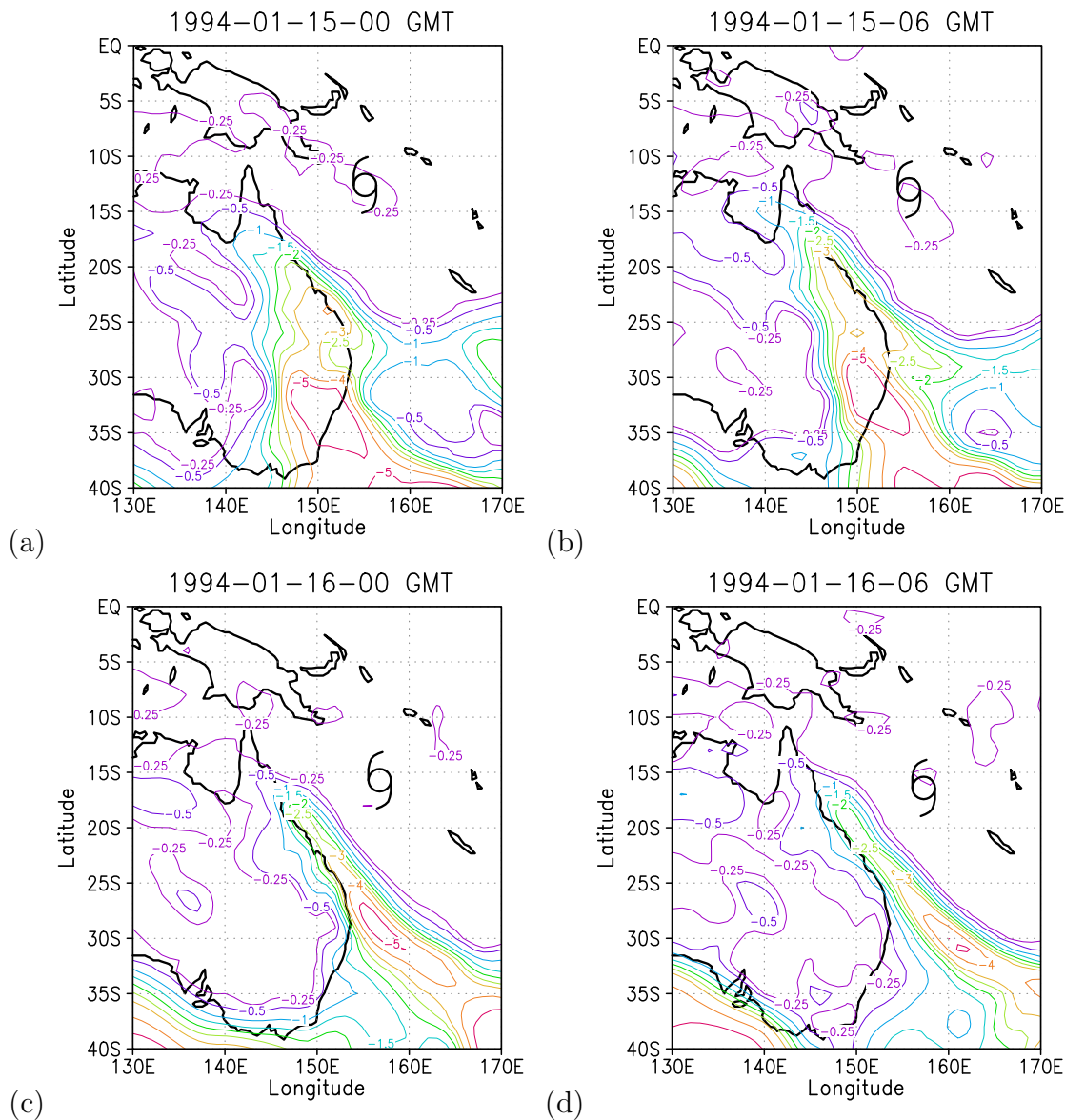


Figure 3.14: Potential vorticity (PVU) at 200 hPa at: (a) 00000 GMT, (b) 0600 GMT on 15 January; (c) 0000 GMT, and (d) 0600 GMT on 16 January.

It is examined whether the temperature decreases ahead of the upper-level trough as the upper-level trough advances towards the tropical cyclone. The temperature field at 500 hPa shows that at 0600 GMT on 15 January, an area of locally high temperature larger

than 270.5 K is approximately collocated with the cyclone position, 13°S, 155°E (Fig. 3.15a). To the south of the cyclone, the temperature decreases with increasing latitude. There is no discernable cooling to the west of the cyclone, ahead of the upper-level trough at this time. At 0600 GMT on 16 January, the cyclone is located around 17°S, 158°E, but a closed area of locally high temperature larger than 270.5 K is still at around 13°S, 155°E, to the northwest of Rewa. This discrepancy is related to the error of the re-analysis in positioning Rewa. The temperature has decreased to the west of the closed area of locally high temperature. This decrease of temperature is related to the cooling associated with the approaching upper-level trough. The cooling coincides with the ascent of isentropic surfaces in the region. However, the temperature decrease does not exceed 0.5 K. Compared to the cooling associated with the upper-level trough in the Burdekin thunderstorm case, the cooling is minimal.

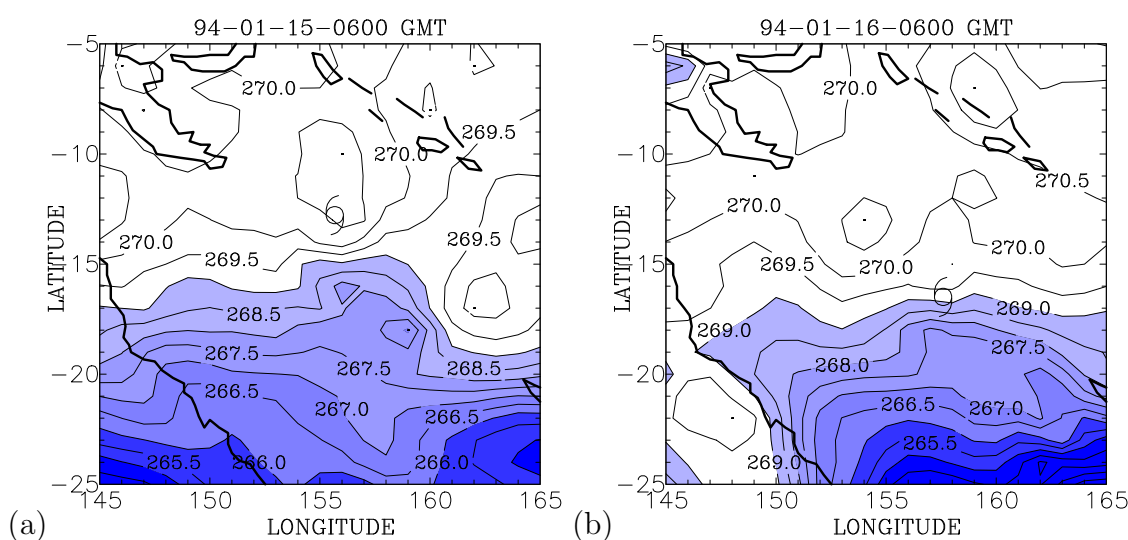


Figure 3.15: Temperature distribution (K) at 500 hPa at: (a) 0600 GMT on 15 and (b) 0600 GMT on 16 January.

As in the Theodore case, dry air from the higher latitudes is advected towards the cyclone when the upper-level trough moves equatorwards and approaches Rewa (Fig.3.16). At 0000 GMT on 16 January, the strongest dry air advection at 500 hPa is found on the northern side of the cyclone, about 400 km away from the cyclone centre (Fig.3.16c) and the mixing ratio at the 500 hPa-level is below  $3 \text{ g kg}^{-1}$  in the region, while the mixing ratio is larger than  $5 \text{ g kg}^{-1}$  within a radius of 200 km from the cyclone centre (Fig.3.16a). At 0600 GMT on 16 January, the strong dry air advection is found to be on the northeastern side of the cyclone, about 200 km away from the cyclone centre and to the southwest of the cyclone (Fig.3.16d). Consequently, the mixing ratio has decreased in these regions (Fig. 3.16b).

The vertical profiles of mixing ratio,  $r$ , temperature,  $T$ , and virtual temperature,  $T_v$ , are examined to assess the effect of the dry air above the boundary layer on the profile of  $T_v$ . Figure 3.17 shows the vertical soundings at 16°S, 154°E and at 16°S, 156°E (close to the cyclone centre) at 0600 GMT on 16 January. The mixing ratio at 154°E is 2-3  $\text{g kg}^{-1}$  lower through the troposphere than that at 156°E, while the vertical soundings of the temperature at the two positions are nearly identical (Fig. 3.17b). The dryness at 154°E

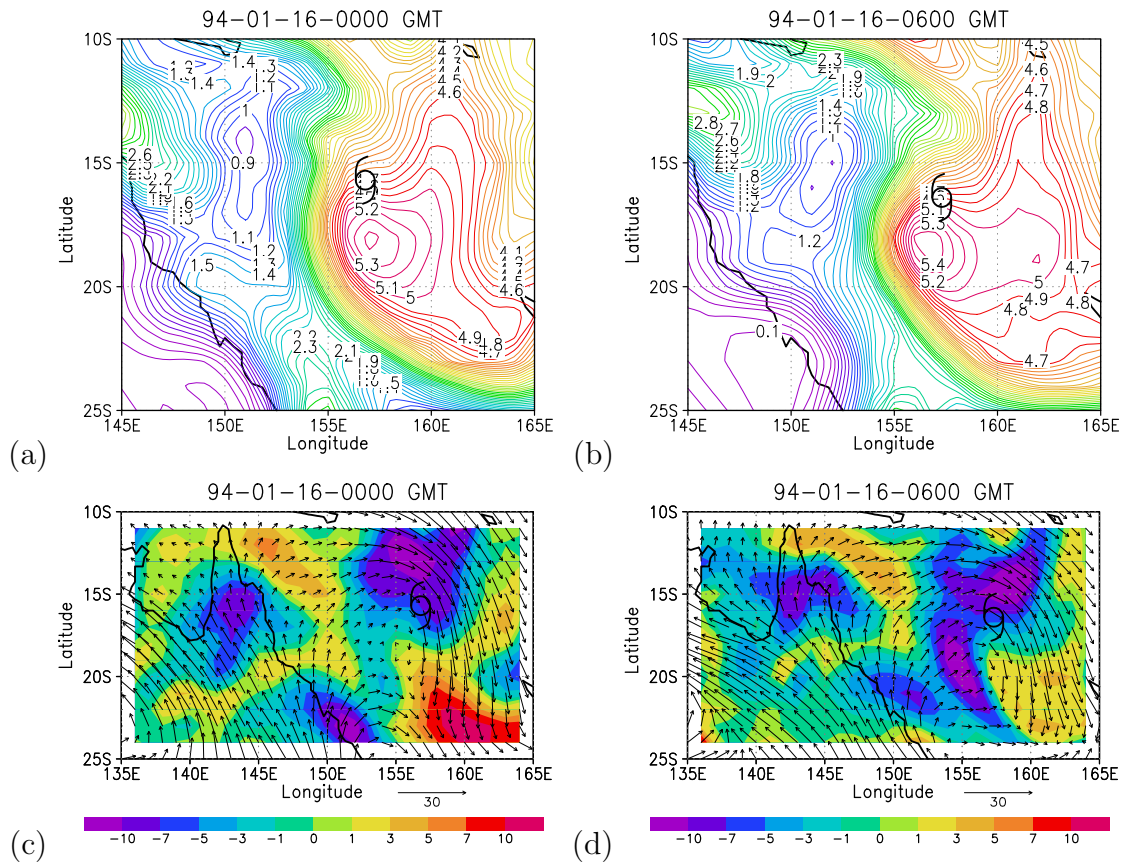


Figure 3.16: The mixing ratio ( $\text{g kg}^{-1}$ ) and its horizontal advection ( $10^{-5} \text{ g kg}^{-1} \text{ s}^{-1}$ ) at 500 hPa at: 0000 GMT (left panels) and at 0600 GMT (right panels) on 16 January.

makes a difference of 0.3 K in the virtual temperature between the two grid points. As in the Theodore case, the effect of the dryness on the value of  $T_v$  is minimal.

The upper and middle-level synoptic situations are shown to be similar to those in the Theodore case, in which the influence of the upper-level trough on the CAPE in the cyclone environment is found to be minimal. Here, it is of interest to determine whether the tendency of CAPE is dependent on that of the boundary-layer mixing ratio as in the Theodore case. Figure 3.18 shows the distribution of the boundary-layer mixing ratio at 0600 GMT on 15 and 16 January. At 0600 GMT on 15 January, the mixing ratio is larger than  $17.5 \text{ g kg}^{-1}$  on the western side of the cyclone, about 200 km away from the cyclone centre, consistent with the error in positioning Rewa. At 0600 GMT on 16 January, there is an elongated area of the mixing ratio larger than  $17.5 \text{ g kg}^{-1}$  around the cyclone (Fig. 3.18b). The distribution of the mixing ratio resembles that of the convective precipitation at each time (see Fig. 3.13). Since the model predicts the precipitation based on the CAPE closure, the region of high mixing ratio (and high precipitation) should be collocated with that of large CAPE according to Equation (3.1).

Figure 3.19 shows that the spatial distribution of the CAPE during the rapid intensification phases of Rewa. The distribution is similar to that of the boundary-layer mixing ratio (see Fig. 3.18) as in the Theodore case. The environmental CAPE is persistently large ( $> 3 \text{ kJ}$

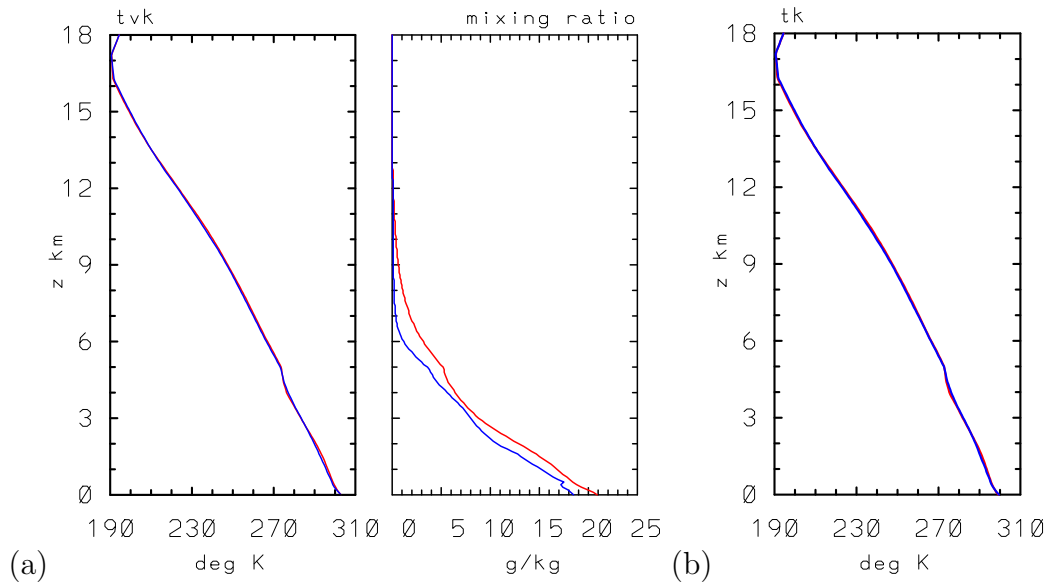


Figure 3.17: The vertical sounding of (a) virtual temperature (K), mixing ratio ( $\text{g kg}^{-1}$ ) and (b) temperature (K) at:  $16^{\circ}\text{S}$ ,  $154^{\circ}\text{E}$  (blue line) and  $16^{\circ}\text{S}$ ,  $156^{\circ}\text{E}$  (red line) at 0600 GMT on 16 January.

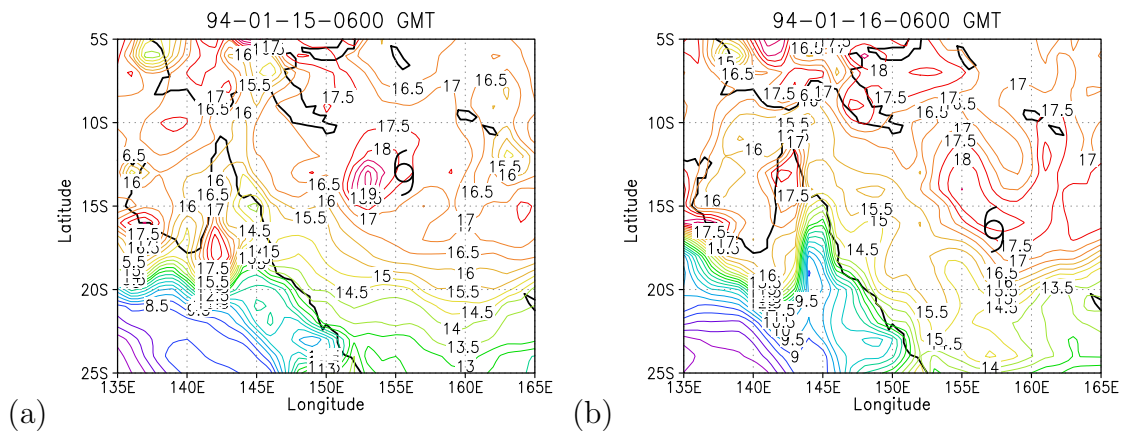


Figure 3.18: The mixing ratio ( $\text{g kg}^{-1}$ ) at 925 hPa at: 0600 GMT (a) on 15 and (b) 16 January.

$\text{kg}^{-1}$ ) during the intensification phase and there is little change of the CAPE during the approach of the upper-level trough. There is no indication of the increase of the CAPE to the west of the cyclone when the trough approaches. The results for the Rewa case show that the convective destabilization due to the approach of the upper-level trough is minimal.

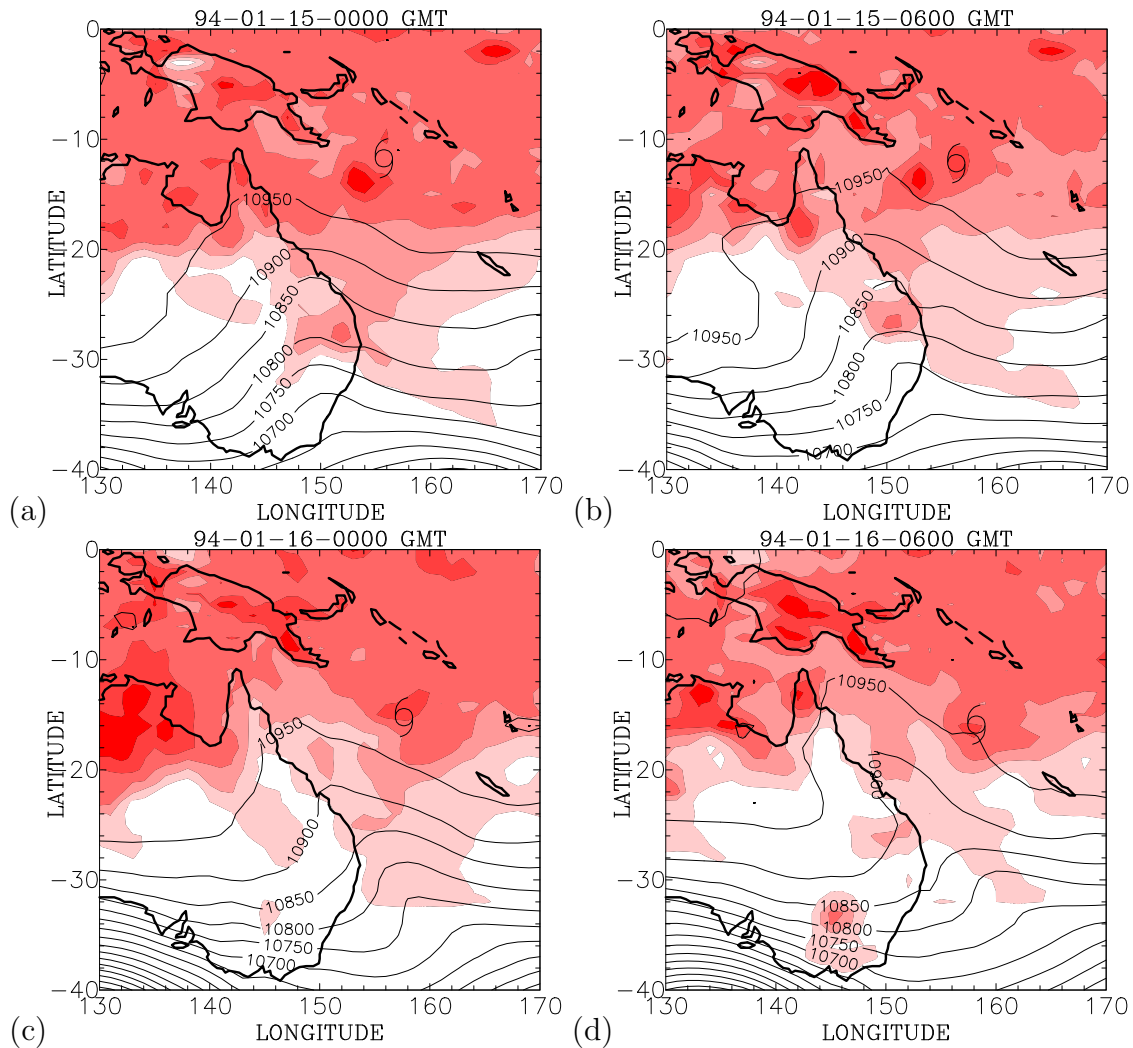


Figure 3.19: Distribution of CAPE for air parcels lifted from the surface assuming pseudoadiabatic process at (a) 0000 GMT, (b) 0600 GMT on 15 January; (c) 0000 GMT, and (d) 0600 GMT on 16 January. The shading starts from  $1 \text{ kJ kg}^{-1}$  and increases in intervals of  $1 \text{ kJ kg}^{-1}$ .

### 3.4 Summary

The possible role of the trough in bringing about convective destabilization is examined in the cases of Rewa and Theodore. The influence of the approaching trough on convective instability is found to be minimal in both the cases. The distribution of CAPE is shown to be determined largely by the boundary-layer mixing ratio. I examined other Australian Tropical Cyclones Paula (2001) and Beni (2003) that developed over the Coral Sea when an upper-level trough was located to the west of these cyclones. The approach of the upper-level trough was not accompanied by a significant change in the CAPE. Shapiro and Möller (2003) showed also that there was no indication of the contribution from an upper-level trough to Opal (1995)'s lower-tropospheric intensification. They examined whether the trough contributed to the increase of convective activity through its effect on vertical

---

motion and static stability. They suggested that the induced ascent by the trough was confined to the upper troposphere and the ascent was weak (at most  $7 \text{ cm s}^{-1}$ ). A layer between 10 km and 12 km was destabilized in the inner-core region, but it was stabilized outside of a radius of about 50 km. Shapiro and Möller (2003) proposed that the net effect of the vertical motions in the upper-troposphere on deep convection was ambiguous in the Opal case.

A remaining question is the sensitivity of vortex intensification to the boundary-layer mixing ratio. This question will be examined in numerical experiments using a simple three-dimensional model.



# Chapter 4

## The control numerical experiments

### 4.1 Introduction

Numerical models of tropical cyclones are the main tools to improve our understanding of the role of moist convection in tropical cyclone dynamics. Although computer power allows calculations of the complex models with a relatively high spatial resolution and sophisticated representations of physical processes now, we can interpret results from calculations of a simple model more easily to understand the cyclone dynamics. The monumental works by Ooyama (1969), Anthes (1972), and Emanuel (1989) provided much insight into tropical cyclone intensification by using simple cyclone models. Numerical experiments in my study are carried out using a simple three-dimensional tropical cyclone model developed by Zhu *et al.* (2001). This model is utilized to explore complex interactions between moist convection and the larger-scale vortex circulation during the intensification phase of the vortex. The model has a fully integrated, albeit highly simplified, representation of moist physics. Simplicity is achieved at the expense of accuracy in the quantification of moist process by neglecting shallow convection, downdrafts, and using a coarse vertical resolution. However, the peak intensity of the model vortex is reasonable, which implies that the buoyancy distribution produced by the simplified moist process is also within a range that is reasonable.

The purpose of the control experiment is to examine the details of the amplification of an incipient vortex into a tropical cyclone-like vortex and to investigate the sensitivity of the amplification to the boundary-layer moisture content that determines convective instability. The convective instability influences the strength of the secondary circulation after grid-scale saturation occurs. The boundary-layer moisture content increases as the surface moisture fluxes provide water vapor into the air. Intensifying vortex circulation enhances the surface moisture fluxes because the surface fluxes increases with wind speed. The enhancement of the surface fluxes is essential for the amplification of the incipient vortex in axisymmetric calculations (e.g. Rotunno and Emanuel 1987). I examine the role of the wind-evaporation feedback mechanism in the intensification of the vortex in three-dimensions by placing a cap on the wind speed in the surface-flux terms.

Details of the model used in this study is provided in Appendix B, including the governing equations and the representation of various physical processes. Some changes made in the model are introduced in section 4.2. Details of vortex intensification are described in section 4.3. Ensemble integrations are introduced and their results are discussed in section 4.4. The dependence of the vortex intensification on the surface fluxes is examined in section 4.5. The conclusions of this study are summarized in section 4.6.

## 4.2 Model description

The model is formulated in  $\sigma$ -coordinates. The configuration of sigma levels is shown in Table 4.1. The number of vertical layers is increased from three to four layers with  $\sigma$ -depths of  $\frac{1}{10}$ ,  $\frac{3}{10}$ ,  $\frac{3}{10}$ ,  $\frac{3}{10}$ , respectively, from the lowest layer to the top layer. The Charney-Phillips grid (CP-grid) is used in the vertical (Zhu and Smith 2003). The table shows the levels at which the dependent variables are calculated. The horizontal velocity and geopotential are stored at the levels,  $k = 1, 2, 3, 4$ , which correspond to  $\sigma = 0.95, 0.75, 0.45, 0.15$ , respectively. Temperature, specific humidity and vertical velocity are stored at  $\sigma_{top}$ ,  $\sigma_{sfc}$ , and  $k = \frac{1}{2}, \frac{3}{2}, \frac{5}{2}, \frac{7}{2}$ , corresponding to  $\sigma = 0.9, 0.6, 0.3, 0.1$ , respectively.

The initial axisymmetric vortex is baroclinic, with the tangential wind speed decreasing with height. The tangential wind distribution at the lowest level,  $k = 4$ , is the same as that used by Smith *et al.* (1990) and is given by,

$$v(r', 4) = \frac{av_m r'(1 + br^4)}{(1 + cr'^2 + dr'^6)^2}. \quad (4.1)$$

where  $r' = r/r_m$ ,  $r$  is the radius from the vortex center,  $r_m$  the radius of maximum tangential wind speed,  $v_m$ , and  $a, b, c,$  and  $d$  are constants, where  $a = 1.78803$ ,  $b = 4.74736 \times 10^{-3}$ ,  $c = 0.339806$ , and  $d = 5.37727 \times 10^{-4}$ . Here I choose  $v_m = 15 \text{ m s}^{-1}$  and  $r_m = 120 \text{ km}$  for an incipient vortex whose strength is weaker than that of a tropical cyclone. The wind speed decreases from  $k = 3$  upwards at the rate of the sine function given by,

$$v(r', k) = v(r', 4) \times \sin \frac{(k-1)\pi}{8}. \quad (4.2)$$

Figure 4.1 shows the height-radius distribution of the wind field at the initial instant.

The area of the computational domain is  $4000 \text{ km} \times 4000 \text{ km}$  and the horizontal grid size is increased from  $20 \text{ km}$ , used by Zhu and Smith *op cit.*, to  $10 \text{ km}$ . The far-field temperature and humidity structure are based on the mean West Indies sounding for the tropical cyclone season (Jordan 1957). The sea surface temperature is taken to be  $26.3 \text{ }^\circ\text{C}$  for all experiments in this study. The calculations are carried out on an  $f$ -plane at  $20 \text{ }^\circ\text{N}$ , where the Coriolis parameter,  $f$ , is  $5 \times 10^{-5} \text{ s}^{-1}$ .

Table 4.1: Configuration of the CP-grid

----- $\dot{\sigma}_{top} = 0, \theta_{top}, q_{top}$ -----	$\sigma_{top} = 0$
----- $\vec{V}_1, \Phi_1$ -----	$k = 1$
----- $\dot{\sigma}_{\frac{3}{2}}, \theta_{\frac{3}{2}}, q_{\frac{3}{2}}$ -----	$\sigma_{\frac{3}{2}} = 0.3$
----- $\vec{V}_2, \Phi_2$ -----	$k = 2$
----- $\dot{\sigma}_{\frac{5}{2}}, \theta_{\frac{5}{2}}, q_{\frac{5}{2}}$ -----	$\sigma_{\frac{5}{2}} = 0.6$
----- $\vec{V}_3, \Phi_3$ -----	$k = 3$
----- $\dot{\sigma}_{\frac{7}{2}}, \theta_{\frac{7}{2}}, q_{\frac{7}{2}}$ -----	$\sigma_{\frac{7}{2}} = 0.9$
----- $\vec{V}_4, \Phi_4$ -----	$k = 4$
----- $\dot{\sigma}_{sfc} = 0, \theta_{sfc}, q_{sfc}$ -----	$\sigma_{sfc} = 1$

The vortex centre at later times is obtained by calculating a centre of weighted relative vorticity defined by

$$(x_{ct}, y_{ct}) = \frac{1}{\int \int \zeta'(x, y) dx dy} \left( \int \int x \zeta'(x, y) dx dy, \int \int y \zeta'(x, y) dx dy \right), \quad (4.3)$$

where  $\zeta'$  is the perturbation of the vertical component of relative vorticity and the double integrals are evaluated over the area  $400 \text{ km} \times 400 \text{ km}$  centered on the location of maximum relative vorticity. A similar definition of the vortex centre was used by Jones (2003), where a PV-weighted centre was calculated.

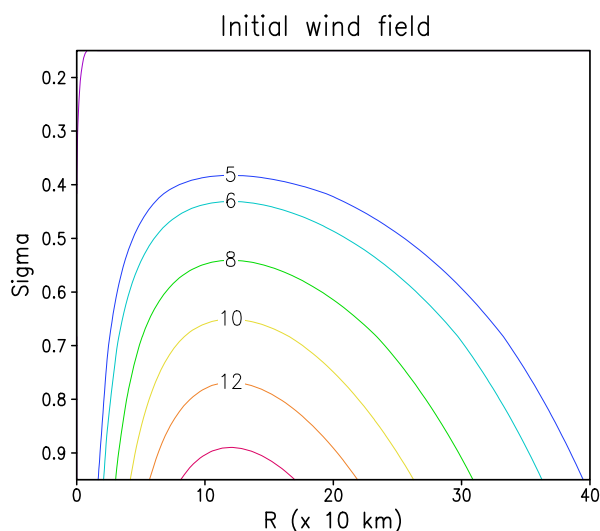


Figure 4.1: Initial height-radius of the tangential wind of the vortex.

Moist processes are calculated explicitly at each grid point, whereby specific humidity is set equal to the saturation specific humidity if the air is saturated with water vapour. Then,

excess water vapour is condensed to liquid water. This water is assumed to precipitate out while the latent heat released is added to the air. The latent heat raises the air temperature and thereby the saturation specific humidity, which requires a further adjustment of the amount of condensed water and latent heat release, and so on (Zhu *et al.* 2001). To determine the final amount of condensed water and latent heat release, a small number of iterations is necessary.

### 4.3 The control run

In this section, I describe the details of vortex intensification in the control run, E01<sub>0</sub>. Figure 4.2 shows time-series of the maximum, azimuthally-averaged, total wind speed at  $\sigma = 0.95$  ( $k = 4$ ), near the top of the boundary layer, and of the surface pressure minimum. The maximum total wind speed is taken to characterize the intensity of the vortex at a given time. The total wind is averaged azimuthally around the centre of weighted vorticity and compared with that averaged around the pressure minimum. The comparison is made in order to examine which way is adequate to find the centre of the vortex. The discussion of the definition of the centre will be given with the overview of the evolution of vortex intensity.

The period until the onset of grid-scale saturation is called the *gestation period*. During the gestation period the boundary-layer mixing ratio increases due to the surface moisture fluxes. The onset time of the grid-scale saturation at  $\sigma = 0.9$  is about 20 h. The maximum, azimuthally-averaged, total wind speed begins to rapidly increase at about 38 h. The beginning of the intensification coincides with the occurrence of grid-scale saturation in certain columns within an annular region between 60 and 80 km radius (Fig. 4.3). Riehl and Malkus (1958) suggested that deep cumulus convection, which they referred to as *hot towers*, play an important role in the vertical transportation of mass and energy in the tropical troposphere. The release of latent heat warms up the air in deep clouds, producing buoyancy. The buoyancy in the heated region leads to convergence towards the clouds and results in the spin-up of the vortex. Figure 4.4 shows that the onset of the rapid intensification coincides with the sharp increase in convergence at all model-levels below the level  $\sigma = 0.15$  ( $k = 1$ ). At this level, divergence occurs as required by continuity.

The deep-layer convergence is strongest at a radius of 80 km at 38 h, but contracts to 40 km after 42 h (Fig. 4.4). Figure 4.5 shows time-series of the mean of azimuthally-averaged convergence at radii between 40 km and 80 km during the period of the rapid intensification. The convergence begins to increase steeply at  $\sigma = 0.95$  and  $0.75$  at 38 h, and at  $\sigma = 0.45$  one hour later. The convergence is strongest at  $\sigma = 0.95$ , near the top of the boundary layer, and its magnitude decreases with height (Fig. 4.5a, b, c). The convergence at each model-level increases with time and reaches a maximum at 42 h. After this time the convergence decreases above the boundary layer, but becomes quasi-steady after 46 h, when the vortex reaches the intensity of a severe tropical cyclone ( $> 33 \text{ m s}^{-1}$ ). In the boundary layer the convergence weakens slightly and remains quasi-steady after 44 h.

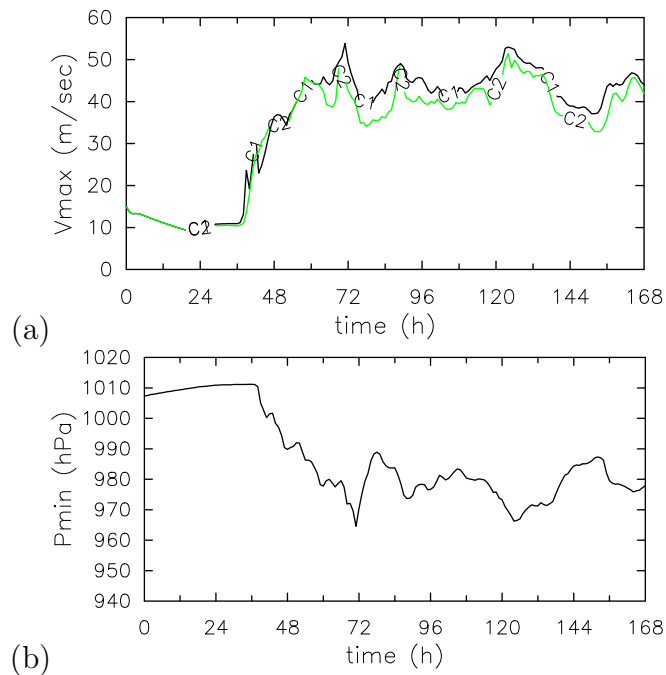


Figure 4.2: Time-series of (a) azimuthally-averaged wind speed maximum ( $V_{max}$ ) at  $\sigma = 0.95$  ( $k = 4$ ) and (b) surface pressure minimum in the calculation E01<sub>1</sub>. The C1 denotes the maximum total wind azimuthally-averaged around the surface pressure minimum and C2 around the centre of weighted vorticity.

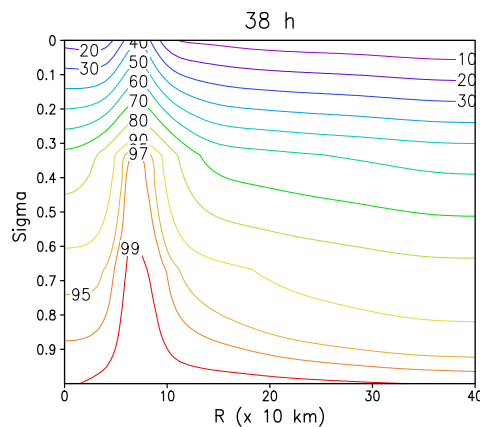


Figure 4.3: Vertical cross section of the azimuthally-averaged relative humidity (%) at 38 h.

I examine structural changes during the period of intensification to explain the evolution pattern of the deep-layer convergence described in the foregoing paragraph. Although the calculation begins with an axisymmetric vortex in an environment at rest on an  $f$ -plane the vortex intensification is found to be intrinsically non-axisymmetric. The non-axisymmetric structural change is illustrated by the vertical component of relative vorticity, total wind speed at  $\sigma = 0.95$ , and the vertical velocity at  $\sigma = 0.9$ . At 42 h, there are four convective cells at the corners of a square within a radius of 80 km (Fig. 4.8). Since these cells have

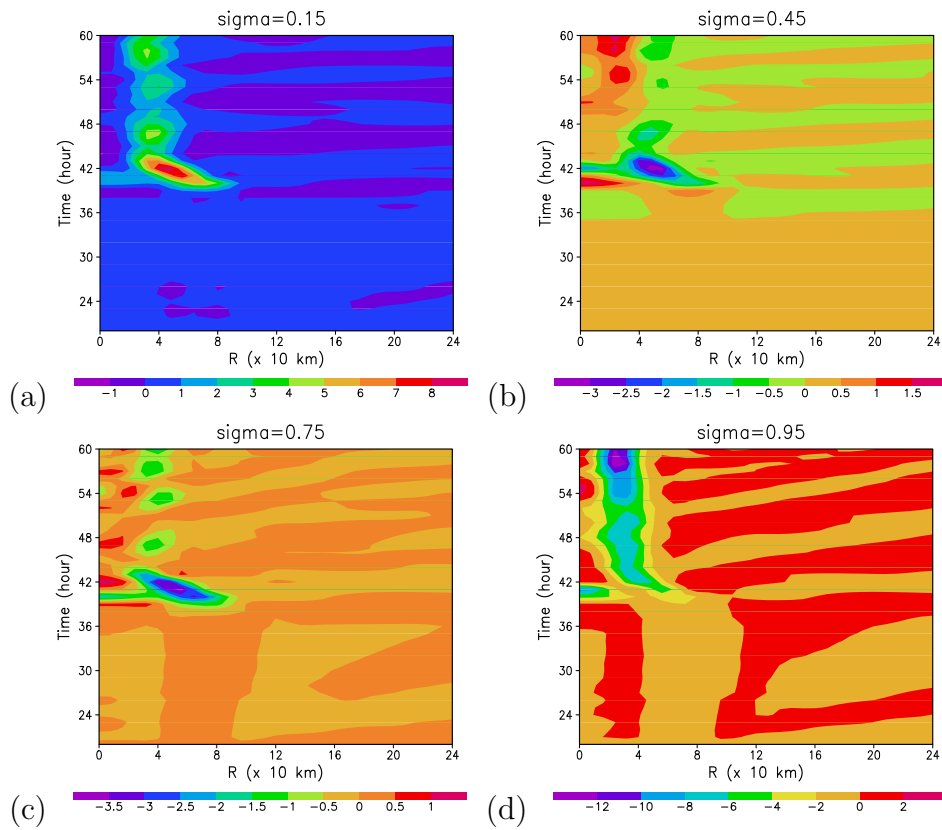


Figure 4.4: Time-radius plots of the azimuthally-averaged divergence at each model-level between 0 h and 60 h.

enhanced rotation (Fig. 4.6), they are referred to as *meso-vortices*. The evolution pattern of the vertical velocity and the total wind fields are nearly identical to that of the vorticity (Fig. 4.7 and Fig. 4.8). The meso-vortices circle around the vortex axis cyclonically and move inwards with the radial flow so that they approach each other with time (Fig. 4.6). The inward movement of the meso-vortices coincides with that of the region of strong ascent (Fig. 4.8) and thereby with the contraction of the radius of the strongest deep-layer convergence (Fig. 4.4). Meso-vortices are often observed in an intense hurricanes (Willoughby and Black 1996). The vortices appeared to be associated with local wind and pressure perturbations (Black and Marks 1991). The features shown in my calculation bear strong resemblance to those features observed in reality. A recent examination of a high-resolution cloud-resolving (3 km horizontal grid spacing) numerical simulation has shown that intense vorticity anomalies are produced by buoyant cores growing in the rotation-rich environment of an incipient storm (Hendricks, *et al.* 2004, Montgomery *et al.* 2006). These simulations showed that the production of the multiple *vortical hot towers*<sup>1</sup> is followed by their mergers and axisymmetrization. The evolutionary processes described in these simulations are captured in a large part by the hydrostatic model with coarser resolution in my study.

The non-axisymmetric vortex intensification indicates the reason for the discrepancy be-

<sup>1</sup>Hendricks *et al.* referred to convective cells possessing enhanced rotation as vortical hot towers.

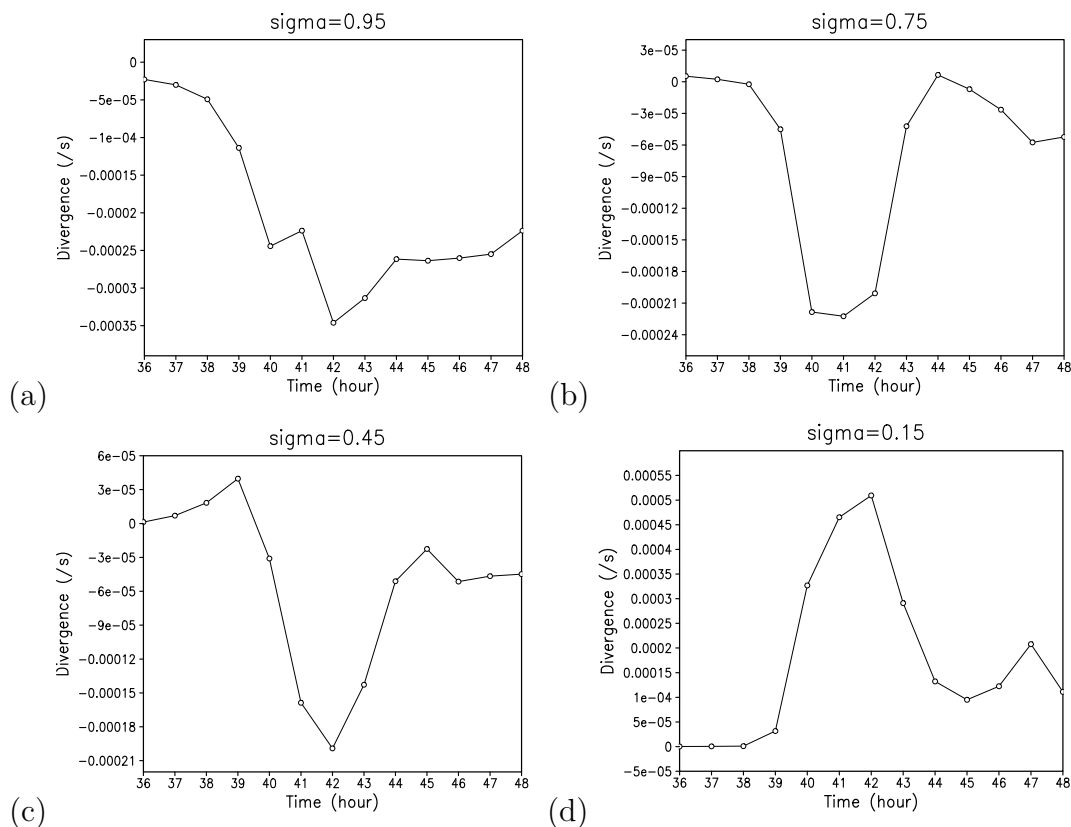


Figure 4.5: Time-series of the azimuthally-averaged divergence ( $s^{-1}$ ) at each model level between 36 and 48 h. The divergence is averaged at radii between 40 and 80 km.

tween the azimuthally-averaged total wind maximum around the surface pressure minimum and around the weighted vorticity centre. The total wind maximum at  $\sigma = 0.95$ , azimuthally-averaged around the surface pressure minimum, is nearly identical to that averaged around weighted vorticity until the meso-vortices emerge (see Fig. 4.2a). However, it changes abruptly during the intensification period because the surface pressure minimum jumps around from one meso-vortex to another (see Fig. 4.2b). On the other hand, the centre of the weighted vorticity is located at the middle of the distance between the meso-vortices (see Fig. 4.6). Therefore, it is preferable to define the vortex centre at the centre of the weighted vorticity to capture a mean state of motion around the axis of the parent vortex.

As the meso-vortices move inwards and the distance between them decreases, nonlinear interaction between them increases. Two of the meso-vortices merge between 43 h and 44 h, leaving an azimuthal wavenumber-3 asymmetry in the vorticity, vertical motion, and total wind fields (Fig. 4.6d, 4.7d, 4.8d). The maximum vorticity and the vertical velocity of the meso-vortices diminish between 42 and 44 h (Fig. 4.6 and Fig. 4.8a, b). The reduction of these quantities coincides with a decrease of the deep-layer convergence during this period. At 46 h, an azimuthal wavenumber-2 asymmetry is dominant (Fig. 4.6e). The vertical velocity field at  $\sigma = 0.9$  shows a region of subsidence around the rotation axis, indicative of an "eye", together with a surrounding annular region of strong ascent, the model analog of eye-wall convection (Fig. 4.8d, e, f). Likewise, there is a region

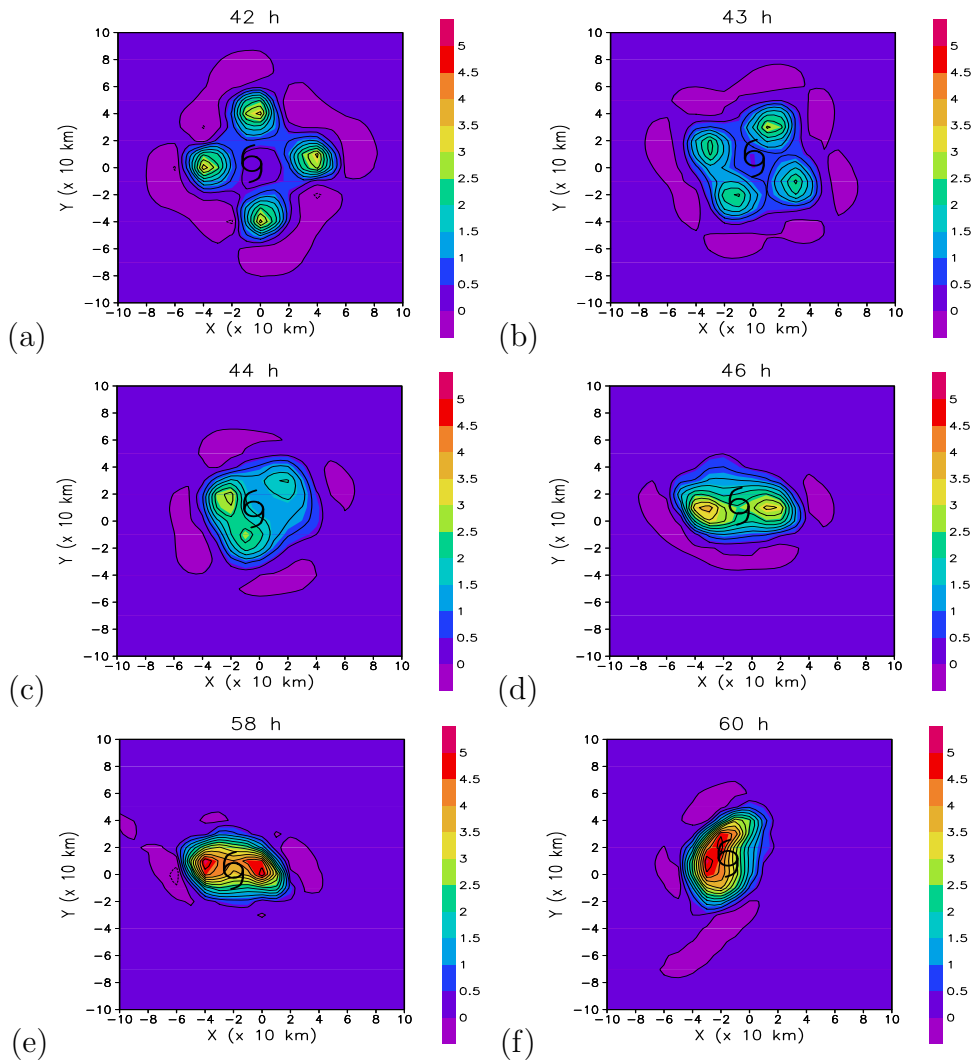


Figure 4.6: Vorticity field at  $\sigma = 0.95$  in the calculation of E01<sub>1</sub> at times indicated on the panels. The contour interval is  $0.4 \text{ s}^{-1}$ . The tropical cyclone symbol denotes the centre of the weighted vorticity.

of low wind speed in the core surrounded by an annular region of high wind speed slightly outside of the eye-wall (Fig. 4.7d, e, f). The area of subsidence and low wind speed around the vortex axis narrows and the radial gradients of vertical velocity and total wind speed increase in the core during the merging process. The frictionally-induced convergence at  $\sigma = 0.95$  maintains relatively high value independent of the merger of the meso-vortices (Fig. 4.5a). However, the convergence above the boundary layer remains minimal after the vortex reaches the intensity of a severe tropical cyclone at 46 h (Fig. 4.5b, c). The shallow convergence near the surface is one of the characteristics of a severe tropical cyclone, which is shown also in the simulations by Montgomery *et al.* (2006). An azimuthal wavenumber-1 asymmetry becomes dominant at the later stage of the intensification phase (Fig. 4.6f). The formation of a number of meso-vortices and their subsequent merger were observed also in the two-dimensional barotropic calculation (Kossin and Schubert 2001). The latter authors suggested that dramatic central pressure falls occurred if the vortices merge to form a monopole.

The merging of meso-vortices coincides with a net influx of absolute angular momentum, which accompanies the rapid intensification. The time-radius distribution of azimuthally-averaged absolute angular momentum at  $\sigma = 0.75$  shows that the angular momentum increases rapidly within a radius of about 100 km during the period of intensification (Fig. 4.9). The increase of the momentum represents the contraction of the radius of the maximum wind during the merging process.

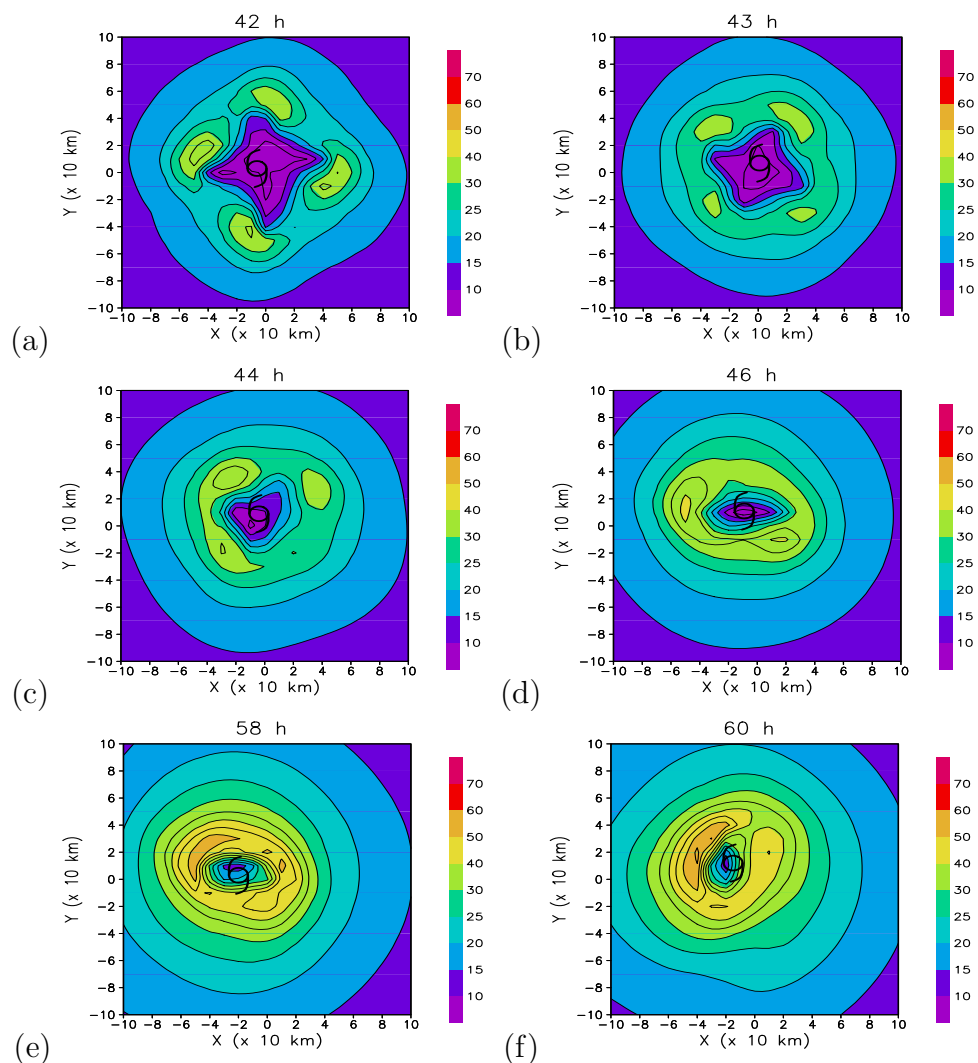


Figure 4.7: The same as Figure 4.6 except total wind fields and the contour interval is  $5 \text{ m s}^{-1}$ .

The contraction of the radius of the maximum wind resembles the response of an axisymmetric baroclinic vortex to heat and momentum sources near the radius of the maximum wind in the calculation by Shapiro and Willoughby (1982). The greatest positive wind tendency lies inside of the radius of the maximum wind of the initial vortex and so acts to contract the radius of the maximum wind as the vortex intensifies. Likewise, the largest increase of the tangential wind occurs inside the radius of the maximum wind of the initial vortex (120 km) in the calculation E01<sub>0</sub> (see Fig. 4.7). This contraction of the radius of the maximum wind is accompanied by the increase of radial gradient of the azimuthally-averaged tangential wind in the core.

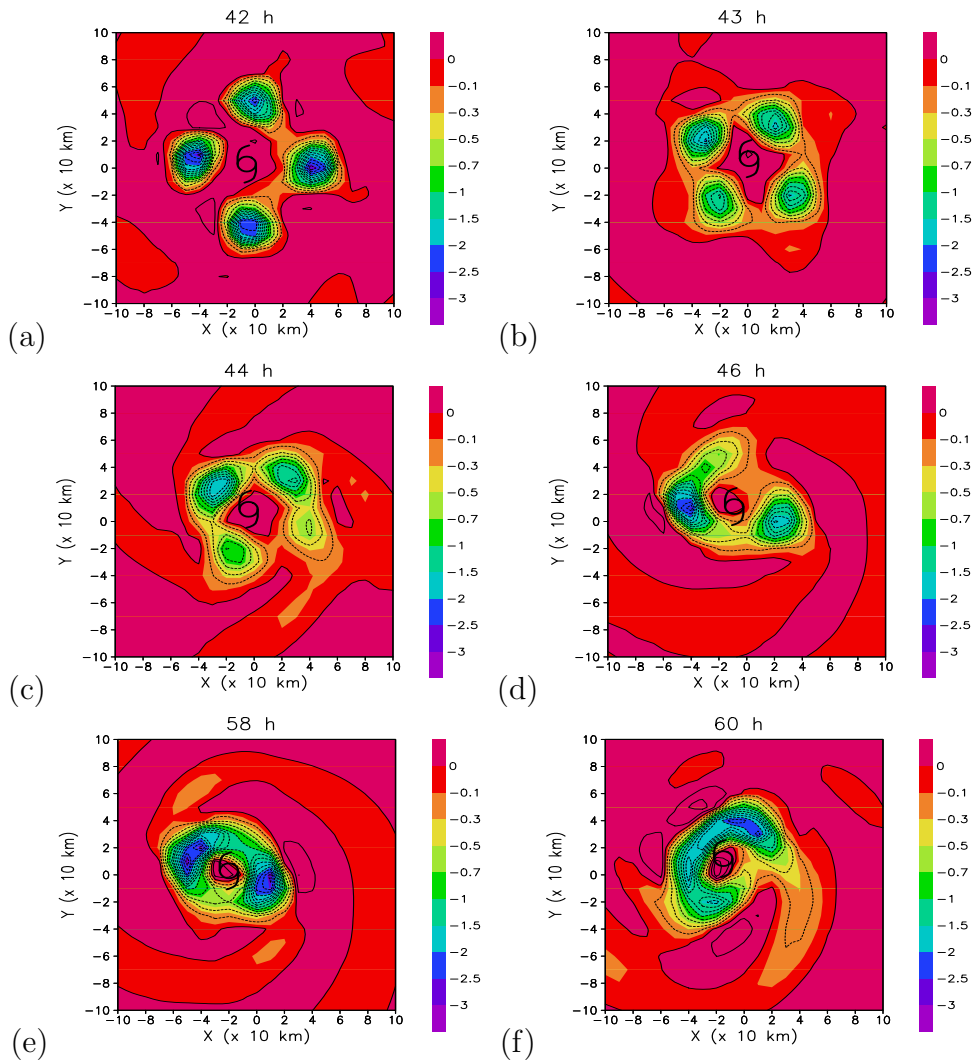


Figure 4.8: The same as Figure 4.6 except  $\dot{\sigma}$  fields at  $\sigma = 0.9$  and the contour interval is  $2 \times 10^{-2} \text{ s}^{-1}$ .

The vortex reaches the intensity of a severe tropical cyclone ( $> 33 \text{ m s}^{-1}$ ) after 46 h and further intensifies until about 60 h. During the *mature stage* (the period after 60 h) the intensity of the vortex fluctuates between about 35 and 50  $\text{m s}^{-1}$  and the intensity averaged during this stage is 40.5  $\text{m s}^{-1}$  (see Fig. 4.2).

As soon as the integration begins, the net upward surface latent and heat fluxes, which are azimuthally-averaged within a radius of 80 km, increases the boundary-layer moist entropy. The boundary-layer moist entropy is influenced greatly by the flux of latent heat, and to a lesser extent sensible heat, from the ocean. The flux is largest at the early stage of the integration and decreases as the air-sea moisture disequilibrium diminishes (Fig. 4.10). After 20 h the fluxes remain nearly zero until the wind speed begins to increase at 38 h. The surface fluxes within a radius of 80 km increase until 70 h, when the vortex attains a peak intensity (about 50  $\text{m s}^{-1}$ ). During the mature stage, the maximum total wind speed fluctuates between 35 and 50  $\text{m s}^{-1}$ , and the corresponding surface flux fluctuates as well.

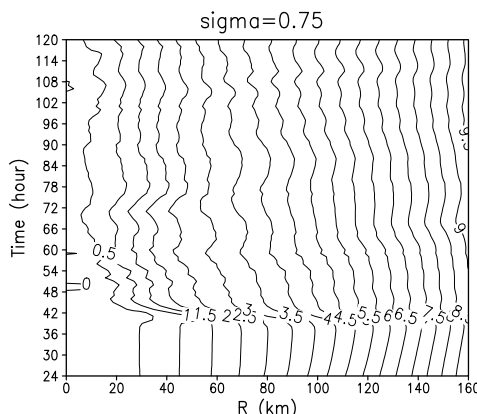


Figure 4.9: Time-radius plot of azimuthally-averaged absolute angular momentum ( $1 \times 10^7 \text{ m}^2 \text{ s}^{-1}$ ) at  $\sigma = 0.75$  between 24 h and 120 h.

The increase of the boundary layer moisture content due to the surface moisture fluxes leads to an increase of CAPE. As soon as the grid-scale saturation occurs, air parcels lifted from the boundary layer have stronger buoyancy if the boundary-layer mixing ratio is larger. Thus, the CAPE influences the secondary circulation after the onset of the grid-scale saturation. The CAPE is calculated for air parcels lifted from the 500 m-level assuming a reversible moist process<sup>2</sup>. The initial CAPE values are only about  $200 \text{ J kg}^{-1}$  (Fig. 4.11a). The CAPE is lowest at the vortex centre and increases outward. The radial distribution of the CAPE is associated with the initial temperature field of the baroclinic vortex that has a cold core at low levels, including the surface (Smith 2006). The values of CAPE increase rapidly with the net upward surface moisture fluxes that add moisture to the boundary layer (Fig. 4.11b). CAPE is larger than  $1 \text{ kJ kg}^{-1}$  within a radius of 80 km at 21 h, when the grid-scale saturation occurs at  $\sigma = 0.9$ . The increase-rate-of the CAPE is largest at the early stage of the integration and it is small after 10 h, consistent with the decrease of the surface moisture fluxes after this time. At 38 h, the meso-vortices emerge within a radius of 100 km in the region of large CAPE (Fig. 4.11c). At 42 h, the CAPE diminishes in the outer region of the meso-vortices because the adiabatic warming associated with subsidence increases the temperature above the boundary layer. On the other hand, CAPE values in the meso-vortices remain high (Fig. 4.11d) because the surface moisture fluxes continue to supply moisture to the meso-vortices (Fig. 4.12). The surface fluxes are enhanced by the locally-large wind speed in the vortices (see Fig. 4.7a). The latent heat release from the deep convection produces local buoyancy relative to the broad-scale thermal field of the parent vortex. As the meso-vortices merge to form a monopole of intense vorticity, buoyancy is largest at the vortex axis and decreases outwards. The warm core results from adiabatic warming associated with subsidence in clear-air regions inside of the eye-wall (see Fig. 4.8d, e, f). The inward increasing buoyancy is one of the characteristics of a mature tropical cyclone. This buoyancy is referred to as *system buoyancy* (Smith *et al.* 2005).

<sup>2</sup>Since the grid-boxes are not saturated at the initial time, this assumption is appropriate. As air parcels in the model are lifted from  $\sigma = 0.95$ , the level of lift is chosen to be 500 m. For the comparison with the initial CAPE, the CAPE at later integration time is calculated in the same way.

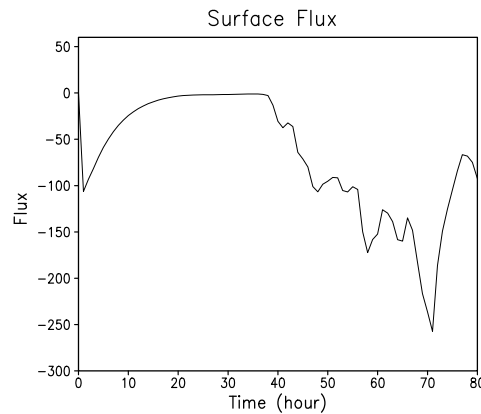


Figure 4.10: Time-series of the azimuthally-averaged surface heat fluxes ( $\text{W m}^{-2}$ ) between 0 h and 80 h. The fluxes include latent and sensible heat flux and are averaged within a radius of 80 km. The net upward surface fluxes is negative.

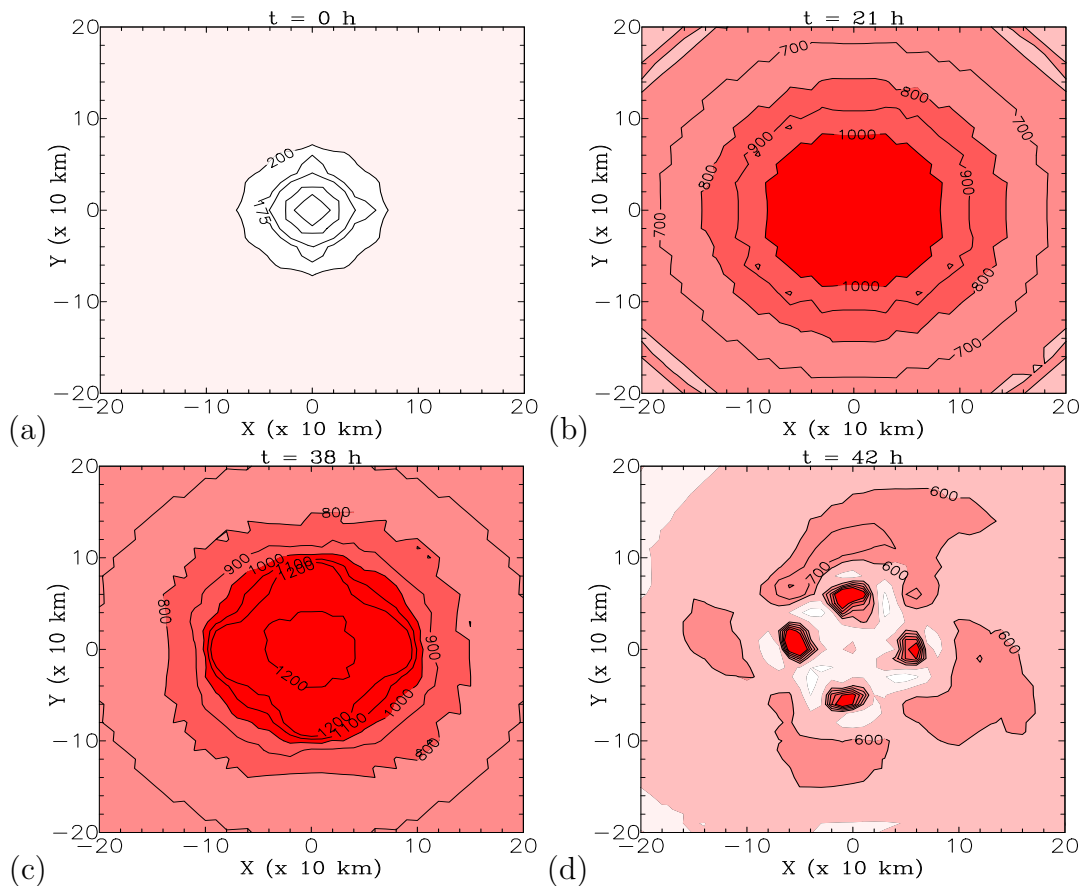


Figure 4.11: CAPE values in  $\text{E01}_1$  at (a) the initial time, (b) 21 h, (c) 38 h, (d) 42 h. The CAPE is calculated for parcels lifted from the 500 m level assuming the reversible process. The contour interval is  $25 \text{ J kg}^{-1}$  and shading starts from  $100 \text{ J kg}^{-1}$  and increases in intervals of  $100 \text{ J kg}^{-1}$  in (a). The contour interval is  $100 \text{ J kg}^{-1}$  and the shading starts from  $200 \text{ J kg}^{-1}$  and increases in intervals of  $200 \text{ J kg}^{-1}$  in (b), (c), and (d).

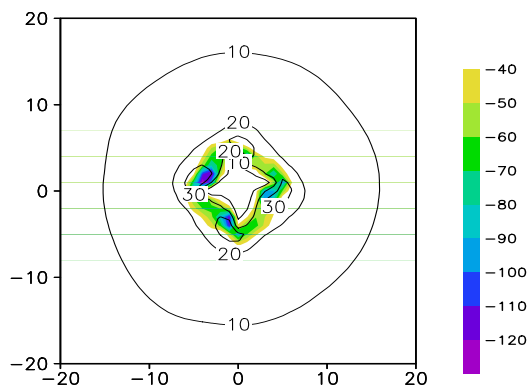


Figure 4.12: Distribution of the net upward surface latent and sensible heat fluxes ( $\text{W s}^{-1}$ ) and total wind speed ( $\text{m s}^{-1}$ ) at 42 h. The shading labels for the flux is listed in the panel and the contour interval for the wind speed is  $10 \text{ m s}^{-1}$ .

## 4.4 Ensemble calculations

Despite the fact that the initial vortex is axisymmetric and the calculations are performed on an  $f$ -plane, the vortex intensification in the calculation  $\text{E01}_0$  is intrinsically asymmetric. As described in section 4.3 meso-vortices form as coherent structures in an annular region of large boundary-layer mixing ratio near the centre of the parent vortex. In reality, The boundary-layer mixing ratio has significant variability on small spatial scales (Weckwerth 2000). It is appropriate to examine the influence of the uncertainty in the boundary-layer moisture content on vortex intensification.

In this study, there are 4 ensemble members in which a random perturbation is added to the boundary-layer moisture content at the initial time. The magnitude of the perturbation is below the accuracy with which the mixing ratio is measured in the Tropics. A sequence of random numbers can be generated from an algorithm that returns a floating-point number. Random numbers in the range of  $\pm 0.5 \text{ (g kg}^{-1}\text{)}$  are added to the mixing ratio field at  $\sigma = 0.9$  and  $\sigma = 1$  of the control run  $\text{E01}_0$  within the square area of  $500 \text{ km} \times 500 \text{ km}$  centered on the vortex axis. Each sequence of the 4 variations will be used again in ensemble integrations in chapter 5. The control calculation  $\text{E01}_0$  described in section 4.3 is one member of the ensemble so that the total number of ensemble members is 5.

Figure 4.13 shows the randomly distributed initial CAPE in the calculation  $\text{E01}_2$ , which reflects the random spatial perturbation of the boundary-layer mixing ratio. The mean value of the CAPE over the square area of  $200 \text{ km} \times 200 \text{ km}$  is  $251 \text{ J kg}^{-1}$ , which is nearly identical to the mean in the calculation of  $\text{E01}_0$  ( $254 \text{ J kg}^{-1}$ ). However, the standard deviation is  $\pm 88 \text{ J kg}^{-1}$ , while it is  $\pm 35 \text{ J kg}^{-1}$  in the control run  $\text{E01}_0$ . The difference indicates that CAPE becomes larger on scattered areas of spatially small scales due to the random perturbation of the moisture field. Subsequently, grid-scale saturation at  $\sigma = 0.9$  occurs at about 18 h, about 2 h earlier than in the control run  $\text{E01}_0$ . The maximum total wind speed begins to rapidly increase at about 36 h in the four ensemble members, compared with 38 h in the control run  $\text{E01}_0$ . This difference between  $\text{E01}_0$  and  $\text{E01}_{1,2,3,4}$

indicates that the onset of vortex intensification is sensitive to the perturbation of the moisture field.

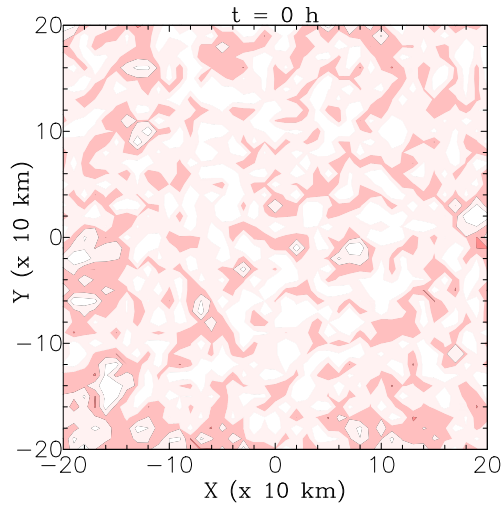


Figure 4.13: Initial CAPE values in the calculation of E01<sub>2</sub>. The CAPE is calculated for parcels lifted from the 500 m-level assuming the reversible process. The shading starts from 100 J kg<sup>-1</sup> and increases in intervals of 100 J kg<sup>-1</sup>.

Figure 4.14a shows that meso-vortices of nearly equivalent size emerge at a radius of about 80 km at 38 h in the control run. In contrast, meso-vortices of variable size and vorticity are at a radius of about 50 km at this time in the calculation E01<sub>2</sub> (Fig. 4.14b). The vorticity of the meso-vortices is stronger and is located at inner radii because the vortices have developed a few hours earlier. The earlier formation of the vortices is a common feature found also in other ensemble calculations E01<sub>1,3,4</sub>. Figure 4.15a shows that neighbouring meso-vortices begin to merge at 40 h in E01<sub>2</sub>. In one hour later an azimuthal wavenumber-2 asymmetry becomes evident (Fig. 4.15b). At 42 h, there are dipoles of intense vorticity and a monopole is the dominant structure after 48 h (Fig. 4.15c, d), which is much earlier than in the control run. The structural change in E01<sub>1</sub> resembles that in E01<sub>2</sub> until 42 h (Fig. 4.16a, b, c), but the formation of a monopole takes more time in E01<sub>1</sub> than in E01<sub>2</sub> (Fig. 4.16d). An azimuthal wavenumber-2 asymmetry is still evident at 48 h in E01<sub>1</sub>, when a monopole has already formed in E01<sub>2</sub>. The differences in the structural change between E01<sub>0</sub>, E01<sub>1</sub>, and E01<sub>2</sub> shows that the merging process is sensitive to the perturbation of the boundary-layer moisture content.

Time-series of the maximum, azimuthally-averaged, total wind speed in the ensemble integrations show that the ensemble spread in intensity arises when the meso-vortices begin to merge at about 40 h (Fig. 4.17). This spread shows that the intensity changes that accompany the merging process are sensitive to the moisture perturbation. The largest difference of intensity between ensemble members is about 18 m s<sup>-1</sup> at 51 h, during the rapid intensification phase. However, it does not exceed 15 m s<sup>-1</sup> at any given time during the mature stage and is less than the intensity fluctuations in the single deterministic integration E01<sub>0</sub>.

The mean intensity of ensemble members during the mature stage is 39.9 m s<sup>-1</sup>, which is

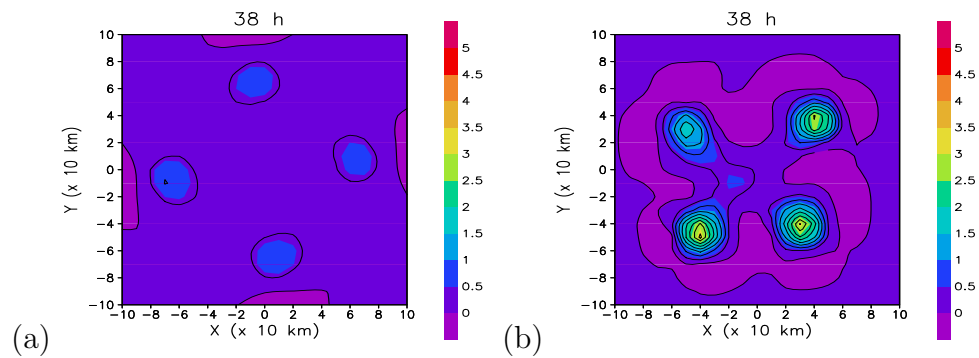


Figure 4.14: Vertical vorticity field at  $\sigma = 0.95$  at 38 h in the calculations (a) E01<sub>0</sub> and (b) E01<sub>2</sub>. The contour interval is  $0.1 \text{ s}^{-1}$ .

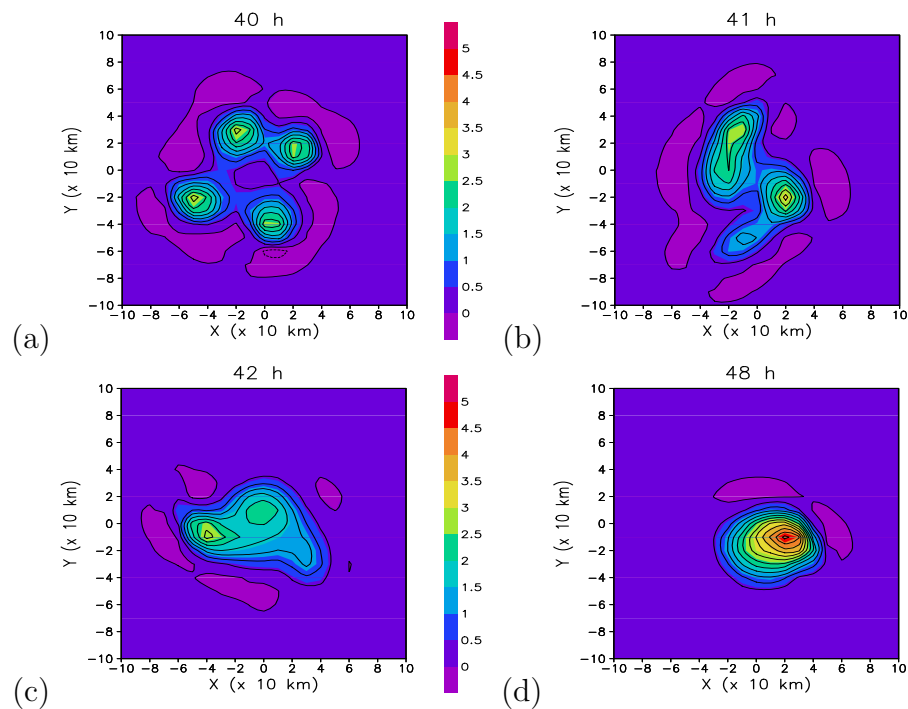


Figure 4.15: Vertical vorticity field at  $\sigma = 0.95$  at (a) 40 h, (b) 41 h, (c) 42 h, and (d) 48 h in the calculation E01<sub>2</sub>. The contour interval is  $0.1 \text{ s}^{-1}$ .

close to that in the calculation E01<sub>0</sub> ( $40.3 \text{ m s}^{-1}$ ). The standard deviation of the intensity of ensemble is  $\pm 4.9 \text{ m s}^{-1}$  during the mature stage. The deviation is within the range of the intensity fluctuations in the control run. The results of the ensemble calculations show that the vortex intensification is highly sensitive to the moisture perturbation in the boundary layer, but intensity of the mature cyclone is only weakly sensitive to the perturbation.

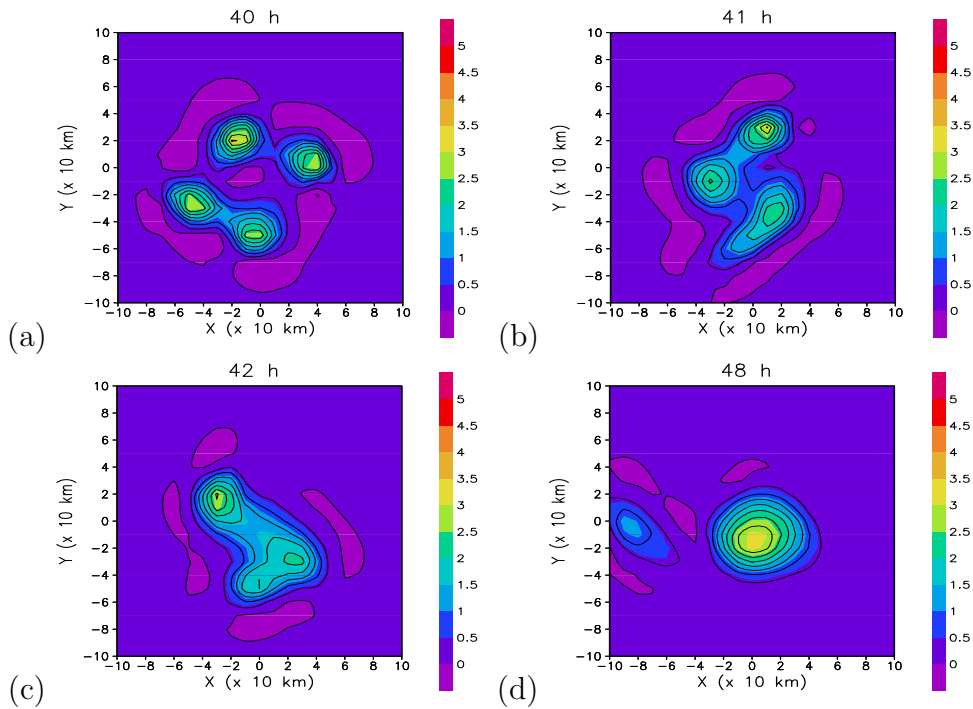


Figure 4.16: Vertical vorticity field at  $\sigma = 0.95$  at (a) 40 h, (b) 41 h, (c) 42 h, and (d) 48 h in the calculation E01<sub>1</sub>. The contour interval is 0.1  $\text{s}^{-1}$ .

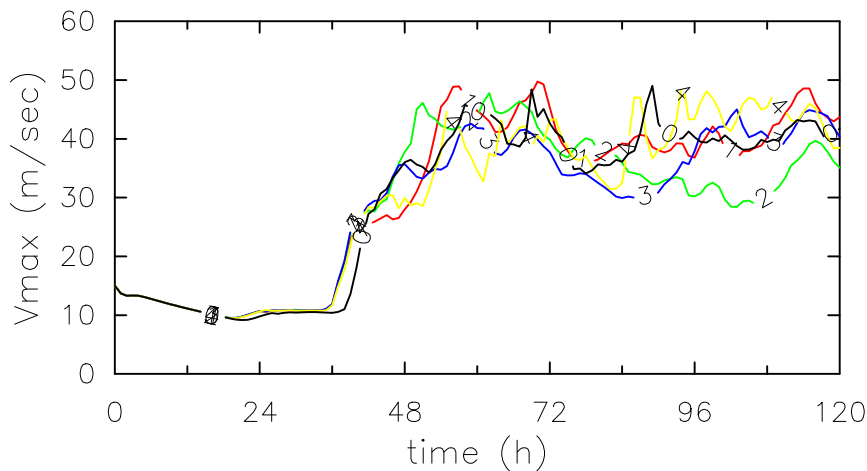


Figure 4.17: Time-series of azimuthally-averaged total wind speed maximum ( $V_{max}$ ) at  $\sigma = 0.95$  in the ensemble calculations E01<sub>0,1,2,3,4</sub>.

## 4.5 Dependence on surface fluxes

The energy required for the intensification of a tropical cyclone is obtained through surface moisture fluxes that transfer latent heat from the ocean to the boundary layer. The surface moisture flux is dependent on wind speed and a difference of moisture content between the air and the saturation mixing ratio at the sea surface temperature. The latent-heat flux

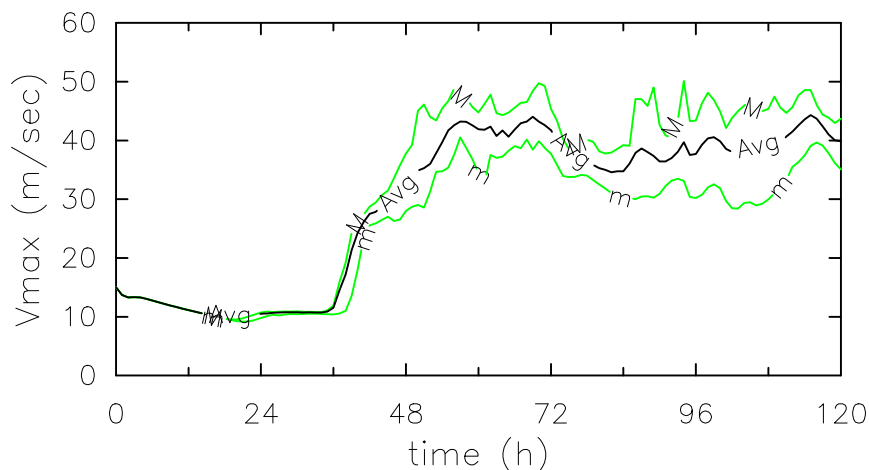


Figure 4.18: Time-series of the upper bound (M), lower bound (m) and mean (Avg) of  $V_{max}$  at  $\sigma = 0.95$  in the ensemble calculations of control experiment E01.

increases dramatically with increasing surface wind speed and this is essential for the intensification of an axisymmetric vortex to a severe tropical cyclone. The feedback mechanism of the wind-evaporation in the intensification of an axisymmetric vortex has been called Wind-Induced Surface Heat Exchange (WISHE) by Yano and Emanuel (1991). In the control calculation E01<sub>0</sub> it is shown that the meso-vortices form in the region of large boundary-layer mixing ratio after the onset of grid-scale saturation. The meso-vortices have no axisymmetric counterpart so that it is of special interest to enquire whether the WISHE mechanism is essential also in the intensification in three-dimensions. In this section, I assess the extent to which the intensification process is captured in the calculations with a capped wind speed in the surface flux terms. The wind speed in the surface flux terms<sup>3</sup> is fixed to be  $5 \text{ m s}^{-1}$  in experiment E01<sub>5</sub> and  $3 \text{ m s}^{-1}$  in E01<sub>6</sub>. The calculations E01<sub>5</sub> and E01<sub>6</sub> attempt to re-examine the role of WISHE process that has been suggested to be the primary mechanism for the amplification of a finite amplitude axisymmetric vortex, but was recently questioned (Nguyen *et al.* 2007, personal communication).

Figure 4.19 shows time-series of the mean of azimuthally-averaged surface fluxes within a radius of 80 km in experiments E01<sub>5</sub> and E01<sub>6</sub>. Shortly after the onset of the integrations, the net upward surface heat flux is about  $60 \text{ W m}^{-2}$  in E01<sub>5</sub> and  $35 \text{ W m}^{-2}$  in E01<sub>6</sub>, while it is  $100 \text{ W m}^{-2}$  in the control run. In the control calculation E01<sub>0</sub>, the flux becomes nearly zero after 10 h as the boundary-layer mixing ratio approaches the saturation mixing ratio at the sea surface. In contrast, the surface flux become nearly zero after 20 h in E01<sub>5</sub> and 30 h in E01<sub>6</sub>. This difference indicates that the net upward surface flux supply the moisture into the boundary layer at a reduced rate when the wind speed is capped in the flux term.

The meso-vortices emerge at about 42 h in E01<sub>5</sub> and 48 h in E01<sub>6</sub>, compared with 38 h in the control calculation. This result indicates that the formation of the meso-vortices is delayed with the reduction of the rate at which the surface moisture fluxes provide the

<sup>3</sup>See Appendix B for the term of surface moisture fluxes in thermodynamic equation.

moisture in the boundary layer. After the onset of the grid-scale saturation, the buoyancy of air parcels in ascent is influenced by the CAPE that depends on the boundary-layer mixing ratio. Figure 4.20 shows that the spatial distribution of the CAPE at 42 h in E01<sub>5</sub> is similar to that at 38 h in the control run, while the distribution in E01<sub>6</sub> resembles that at 21 h, showing the lower rate-of-increase of the CAPE in the calculations with the capped wind speed in the surface flux terms.

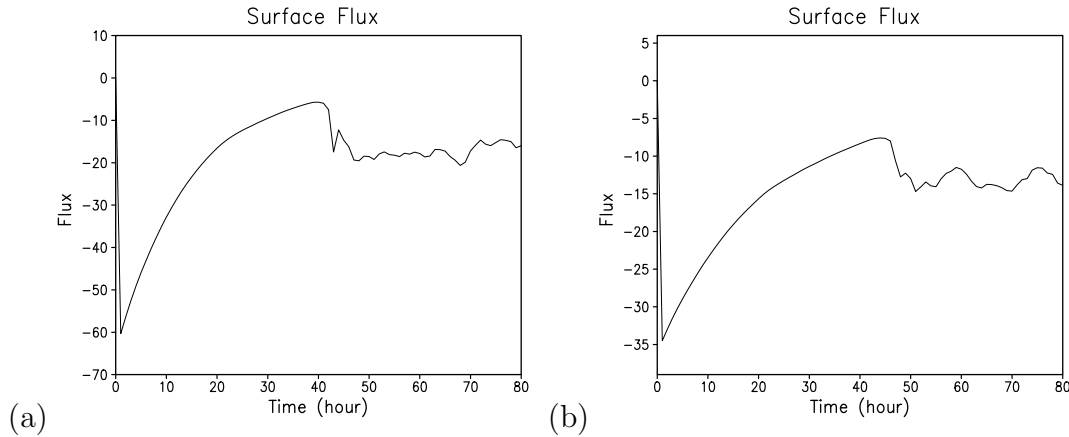


Figure 4.19: Time-series of the surface latent and sensible heat fluxes ( $\text{W m}^{-2}$ ), which are azimuthally-averaged within a radius of 80 km in the calculations (a) E01<sub>5</sub> and (b) E01<sub>6</sub>. The ordinate ranges between  $-70$  and  $10 \text{ W m}^{-2}$  in the left panel and between  $-35$  and  $5 \text{ W m}^{-2}$  in the right panel.

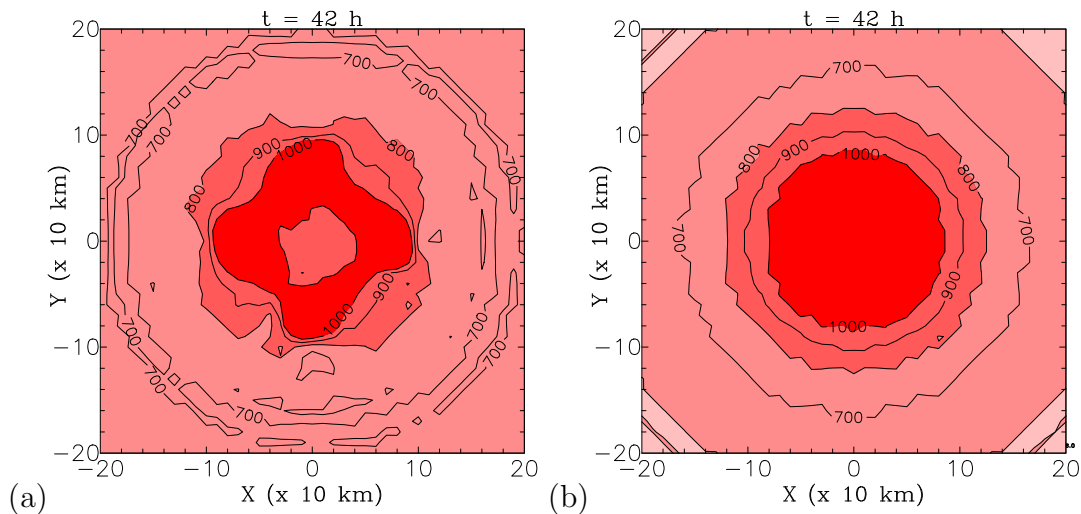


Figure 4.20: CAPE values at 42 h in the calculations (a) E01<sub>2</sub> and (b) E01<sub>6</sub>. The CAPE is calculated for parcels lifted from the 500 m-level assuming the reversible process. The shading starts from  $200 \text{ J kg}^{-1}$  and increases in intervals of  $200 \text{ J kg}^{-1}$ .

Time-series of vortex intensity during the mature stage are within the deviation envelope of intensity in the ensemble calculations (Fig. 4.21). The incipient vortex manages to amplify into the severe cyclone despite the significant reduction of the surface fluxes, since the radial gradient of buoyancy is produced with the formation of a monopole of intense vorticity

through the merger of the meso-vortices. The results for these calculations show that the feedback mechanism of wind-evaporation (WISHE) is not necessary for the intensification of a severe tropical cyclone in three-dimensions since the local CAPE within the meso-vortices is enough for the development of the secondary circulation.

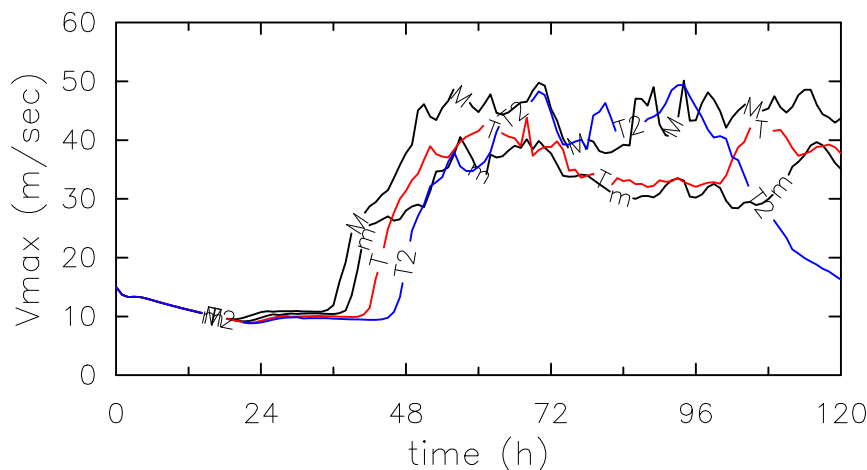


Figure 4.21: Time-series of azimuthally-averaged total wind speed maximum ( $V_{max}$ ) at  $\sigma = 0.95$  in the calculations E01<sub>5</sub> (denoted by T) and E01<sub>6</sub> (T2) in comparison to the deviation envelop of ensemble calculations (upper bound denoted by M and lower bound by m).

## 4.6 Summary

The evolution of a tropical cyclone-like vortex is investigated using a simple tropical-cyclone model. The pattern of intensification of the vortex is largely similar to the behaviour of a cyclone observed by reconnaissance aircraft. During the gestation period, the boundary-layer moisture content and thereby CAPE increase due to the net upward surface moisture flux. The increase is largest at the early stage of the gestation period and becomes small as the air-sea moisture disequilibrium diminishes. After the onset of the grid-scale saturation, meso-vortices form earlier if the CAPE increases more rapidly and *vice versa*, since the secondary circulation strengthens with the buoyancy of air parcels lifted from the boundary layer. As the meso-vortices rotate cyclonically and move inwards with the secondary circulation associated with the parent vortex, neighbouring vortices merge and eventually a monopole of intense vorticity forms. The formation of the monopole accompanies the contraction of the radius of the maximum wind and the increase of the radial gradient of buoyancy. These results for the control experiment show that the vortex intensification is an intrinsically non-axisymmetric process.

I have investigated the sensitivity of vortex intensification to perturbations in the moisture content in the boundary layer with ensemble calculations. The formation and subsequent merger of the meso-vortices are found to be sensitive to the moisture perturbation. However, the intensity of the mature cyclone is weakly sensitive to the perturbation. The ensemble-mean intensity is similar to that in the control run E01<sub>0</sub> and the deviation of

ensemble intensity is within the range of the intensity fluctuations in the control run.

In addition, I have examined the role of surface fluxes in the amplification of the incipient vortex into the tropical cyclone-like vortex by placing a cap on the wind speed in the surface flux terms. The formation of the meso-vortices is delayed due to the reduction of the surface moisture flux, since the boundary-layer moisture content increases at a reduced rate compared with that in the control run. However, a significant finding is that the pattern of the vortex intensification after the formation of the meso-vortices is independent of the magnitude of the surface fluxes. It is shown that an incipient vortex intensifies to a severe tropical cyclone in three-dimensions even when the surface moisture flux does not increase appreciably with increasing surface wind speed.

In the next chapter I examine the effects of radiative cooling rate, the middle-tropospheric humidity, and an upper-level, anticyclonic, horizontal shear flow on vortex intensification.

# Chapter 5

## Some factors affecting vortex intensification

### 5.1 Introduction

In chapter 4, it was shown that the formation and subsequent merger of the meso-vortices are sensitive to the moisture perturbation in the boundary layer. Here, the effects of three factors on the evolutionary process are investigated: these include a radiative cooling rate, the low humidity of the middle-troposphere, and the presence of an upper-level, anticyclonic, horizontal shear flow. The motivations for this investigation and discussion of results are given in following sections. Ensemble calculations are carried out to find robust features of vortex intensification in each experiment. Another point of interest is the predictability of the vortex intensity.

I discuss the effect an enhanced rate of the radiative cooling on the formation and subsequent merger of the meso-vortices in section 5.2. The vortex intensification in the environment of the low middle-tropospheric humidity is examined in section 5.3. The influence of an upper-level, anticyclonic, horizontal shear flow on the rate of vortex intensification is discussed in section 5.4. Finally, summary and conclusions are given in section 5.5.

## 5.2 Radiative cooling

The addition of a Newtonian cooling term in the thermodynamic equation is normally implemented to compensate the heat input from the ocean in tropical cyclone models (e.g. Rotunno and Emanuel 1987; Emanuel 1989; Zhu *et al.* 2001). The cooling term is added to the right-hand-side of the thermodynamic equation to represent radiative cooling in the model (see Appendix B). The radiative cooling term is defined by

$$-(\theta - \bar{\theta})/\tau_R, \quad (5.1)$$

where  $\theta$ ,  $\bar{\theta}$ , and  $\tau_R$  are the potential temperature, domain-mean potential temperature, and radiative cooling rate, respectively. Rotunno and Emanuel (1987) selected a value of 12 h for  $\tau_R$ . They noted that the radiative cooling becomes unrealistically large in the eye where  $\theta - \bar{\theta}$  becomes large (Rotunno and Emanuel 1987). To represent the radiative cooling more realistically, Emanuel (1989) placed a cap on the radiative cooling so that it does not exceed  $2 \text{ K day}^{-1}$ . In addition, the cooling was turned off in the cloudy regions. Zhu *et al.* (2001) applied the radiative cooling in the same way as Emanuel (1989).

Mapes and Zuidema (1996) suggested that the Newtonian cooling approximation with the time scale  $\tau_R = 10$  days was close to the actual mean time scale of radiative cooling in the Tropics. In the control experiments discussed in chapter 4, I use this time scale for the radiative cooling term. This cooling rate is small compared to that used in the axisymmetric calculations by Rotunno and Emanuel (1987), Emanuel (1989), and Persing and Montgomery (2005) in which the time-scale is 12 h. In experiment set E02 I use the strong radiative cooling used by those authors to examine the consequence of the enhanced rate of the radiative cooling on vortex intensification. The radiative cooling is turned on only in regions where the relative humidity at  $\sigma = 0.6$  is less than 90 percent. This treatment is intended to turn off the cooling in cloudy region as in Emanuel (1989). The cooling in the cloud-free regions does not exceed  $2 \text{ K day}^{-1}$ . The temperature relaxation represented by the radiative cooling term is imposed at every model-level. In addition, experiments (E03) without the radiative cooling are carried out to compare the vortex intensification with that in E02.

Ensemble calculations are carried out using the same sequences of random numbers as in the control experiment. Robust features of the intensification with the strong radiative cooling and the predictability of vortex intensity are examined with the ensemble calculations.

The calculations E02<sub>0</sub> and E03<sub>0</sub> are the ensemble members of the experiment sets E02 (with the enhanced cooling rate) and E03 (without radiative cooling), without the random perturbation in the boundary-layer mixing ratio. The vortex intensification in E02<sub>0</sub> and E03<sub>0</sub> is compared with that in the control calculation E01<sub>0</sub> first. Figure 5.1 compares time-series of the maximum, azimuthally-averaged, total wind speed in the calculations E02<sub>0</sub> and E03<sub>0</sub> with those in the control run. This wind speed is azimuthally-averaged around the weighted vorticity centre. Without the radiative cooling (E03<sub>0</sub>) the pattern of vortex intensification is similar to that in the control calculation. However, with strong radiative

cooling (E02<sub>0</sub>) the pattern is considerably different from that in the other calculations. The main difference is the delayed onset time of the rapid intensification, which is about 36 h later than that in the calculation without the radiative cooling. The reason for the delay is the later onset of grid-scale saturation.

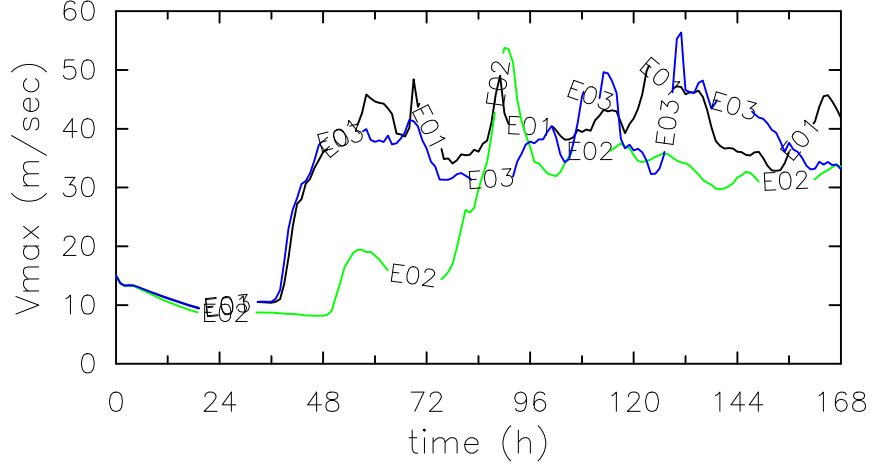


Figure 5.1: Time-series of azimuthally-averaged maximum total wind speed ( $V_{max}$ ) at  $\sigma = 0.95$  in the calculations (a) E02<sub>0</sub> (denoted by E02) and (b) E03<sub>0</sub> (E03). The time-series of  $V_{max}$  in the calculation E01<sub>0</sub> is denoted by E01.

It takes longer for grid-scale saturation to occur if the ascending motion within the radius of the maximum wind is weaker. The question is: how does the strong radiative cooling affects the ascending motion. The radiative cooling rate is proportional to the potential temperature perturbation (see Equation (5.1), which increases inwards since the core of a tropical cyclone is warm. Accordingly, the buoyancy in the core region is weaker than that in the calculation without radiative cooling. Figure 5.2 shows the distribution of buoyancy of air parcels at 1 km (near  $\sigma = 0.9$ ) at 17 h. The buoyancy is weaker within a radius of 80 km in the calculation with the strong radiative cooling (E02<sub>0</sub>) than in E03<sub>0</sub> without the cooling.

On the basis of the *Sawyer-Eliassen equation*, a reduction in the secondary circulation is hypothesized to be a plausible consequence of the weakening of warm core due to the strong radiative cooling. This equation is an approximate form of the local time derivative of the equation for the toroidal vorticity,  $\eta = \partial u / \partial z - \partial w / \partial r$ . This component of vorticity characterizes the secondary circulation of an axisymmetric tropical cyclone-like vortex (Smith *et al.* 2005). The stream function  $\psi$  for the toroidal circulation is related to the radial and vertical wind component ( $u, w$ ) by:  $u = (-1/r\rho)(\partial\psi/\partial z)$ ,  $w = (1/r\rho)(\partial\psi/\partial r)$ . The Sawyer-Eliassen equation is an equation for the streamfunction  $\psi$ . It may be written (Smith *et al.* 2005):

$$\begin{aligned} \frac{\partial}{\partial r} \left[ -g \frac{\partial \chi}{\partial z} \frac{1}{\rho r} \frac{\partial \psi}{\partial r} - \frac{\partial}{\partial z} (\chi C) \frac{1}{\rho r} \frac{\partial \psi}{\partial z} \right] + \frac{\partial}{\partial z} \left[ (\xi \chi (\zeta + f) + C \frac{\partial \chi}{\partial r}) \frac{1}{\rho r} \frac{\partial \psi}{\partial z} - \frac{\partial}{\partial z} (\chi C) \frac{1}{\rho r} \frac{\partial \psi}{\partial r} \right] \\ = g \frac{\partial}{\partial r} (\chi^2 \dot{\theta}) + \frac{\partial}{\partial z} (C \chi^2 \dot{\theta}) - \frac{\partial}{\partial z} (\chi \xi \dot{v}), \quad (5.2) \end{aligned}$$

where  $\chi = 1/\theta$ ,  $\dot{v}$  is the time derivative of tangential wind component,  $\xi = 2v/r + f$ ,  $\zeta = (1/r)(\partial(rv)/\partial r)$ , and  $C = v^2/r + fv$  is the sum of the centrifugal and Coriolis forces per unit mass. The term  $\dot{\theta}$  is diabatic heating rate, which is negative if there is radiative cooling. Equation (5.2) shows that the toroidal circulation is determined by the radial and vertical gradients of diabatic heating rate, and to the vertical gradient of the momentum source. This equation is an elliptic partial differential equation provided that the discriminant,  $D = -g\partial\chi/\partial z[\xi\chi(\zeta + f) + C\partial\chi/\partial z] - [\partial(\chi C)/\partial z]^2$ , is positive (Shapiro and Willoughby 1982; Smith *et al.* 2005). The first term on the right-hand side of Equation (5.2) is positive due to the radiative cooling and acts to reduce the frictionally-induced secondary circulation.

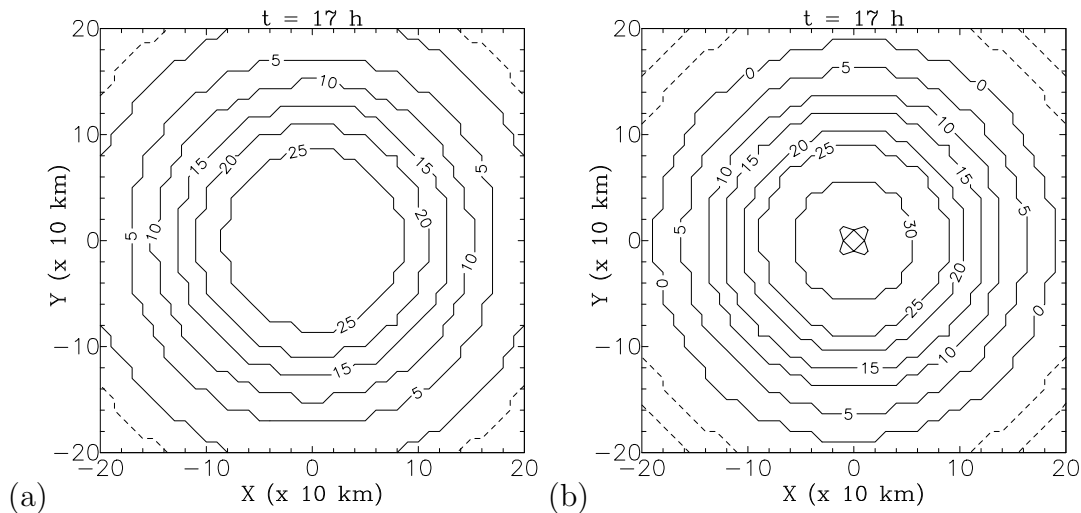


Figure 5.2: Distribution of buoyancy relative to the environment at 1 km at 17 h in the calculations (a) E02<sub>0</sub>, and (b) E03<sub>0</sub>. The contour interval is  $10^{-3} \text{ m s}^{-2}$ .

The reduction in the strength of the secondary circulation is shown by the weaker ascent and weaker radial inflow in the calculation with strong radiative cooling than in E03<sub>0</sub> (without the cooling). Figure 5.3 shows the distribution of the vertical velocity ( $\dot{\sigma}$ ) at  $\sigma = 0.9$  in the calculations with strong radiative cooling (E02<sub>0</sub>) and without radiative cooling (E03<sub>0</sub>). At 17 h, the ascent is smaller in E02<sub>0</sub> than in E03<sub>0</sub> (Fig. 5.3a, b). Also the ascent in E02<sub>0</sub> diminishes in the next four hours (Fig. 5.3c). Consistent with this behaviour, the radial inflow at  $\sigma = 0.95$  in E02<sub>0</sub> is lower than that in E03<sub>0</sub> (Fig. 5.4a, b) and diminishes also during that period (Fig. 5.4c). On the other hand, the ascent and radial inflow increase between 17 and 21 h in E03<sub>0</sub> as the grid-scale saturation occurs at about 20 h (Fig. 5.3d and Fig. 5.4d). In the calculation with strong radiative cooling, E02<sub>0</sub>, the reduced strength of the secondary circulation delays the onset of the grid-scale saturation and thereby the formation of the meso-vortices. The grid-scale saturation at  $\sigma = 0.9$  occurs at about 23 h, and the meso-vortices emerge at about 45 h in E02<sub>0</sub> about 9 hours later than in E03<sub>0</sub>.

Snapshots of the vertical component of relative vorticity fields at  $\sigma = 0.95$  (Fig. 5.5) show the delayed formation and subsequent mergers of the meso-vortices in the calculation with strong radiative cooling (E02<sub>0</sub>), compared with that in the calculation without the cooling (E03<sub>0</sub>). In the calculation E02<sub>0</sub>, four meso-vortices have formed at a radius of about 60 km at 54 h (Fig. 5.5a), while their counterparts in E03<sub>0</sub> are already at a radius of about

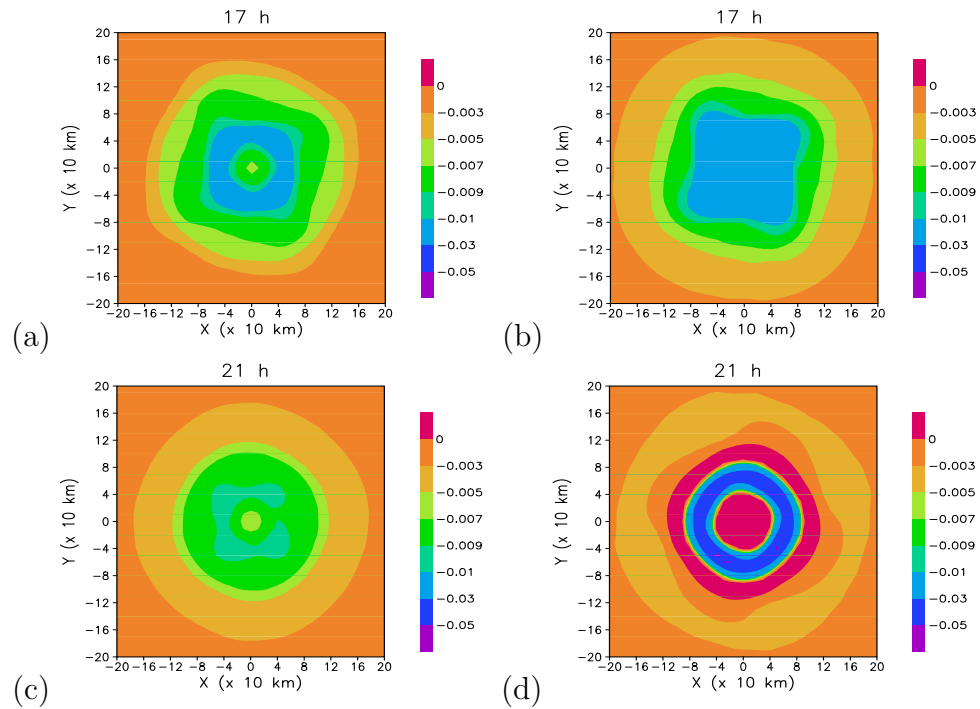


Figure 5.3: Distribution of the vertical velocity  $\dot{\sigma}$  ( $10^{-1} s^{-1}$ ) at  $\sigma = 0.9$  at 17 h (upper panels) and at 21 h (lower panels) in the calculations E02<sub>0</sub> and E03<sub>0</sub>.

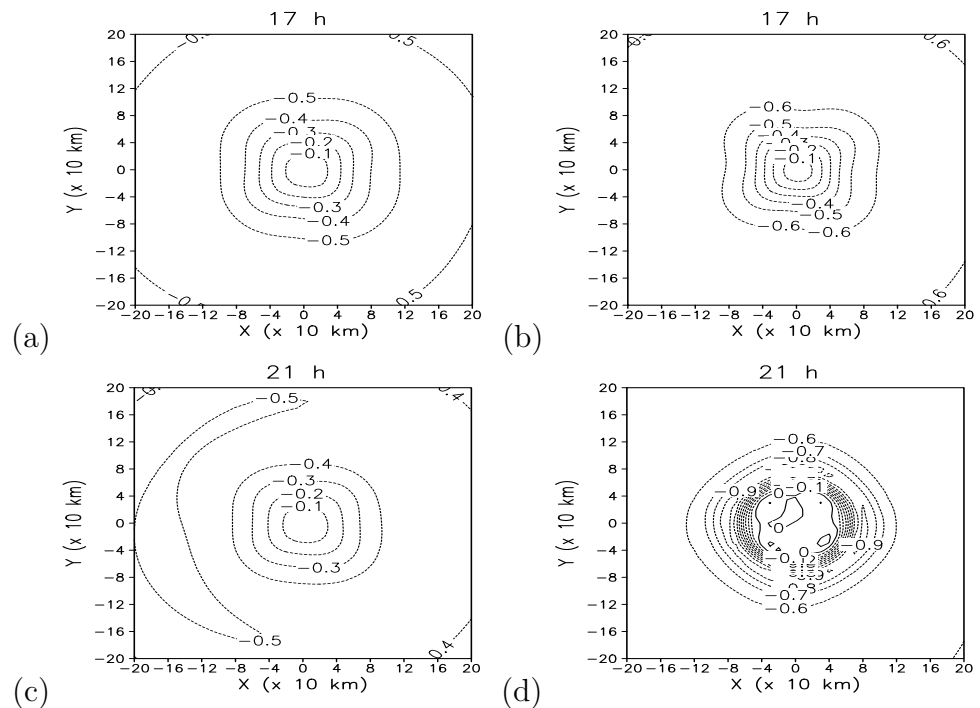


Figure 5.4: The same as Figure 5.3 except radial flow at  $\sigma = 0.95$ .

40 km at 42 h as they had formed already at about 36 h (Fig. 5.5c). The meso-vortices in the calculation E03<sub>0</sub> merge to form an approximate monopole of intense vorticity at 48

h (Fig. 5.5d), but at about 80 h in E02<sub>0</sub> (Fig. 5.5d). This comparison shows that the formation of the monopole is delayed also by strong radiative cooling.

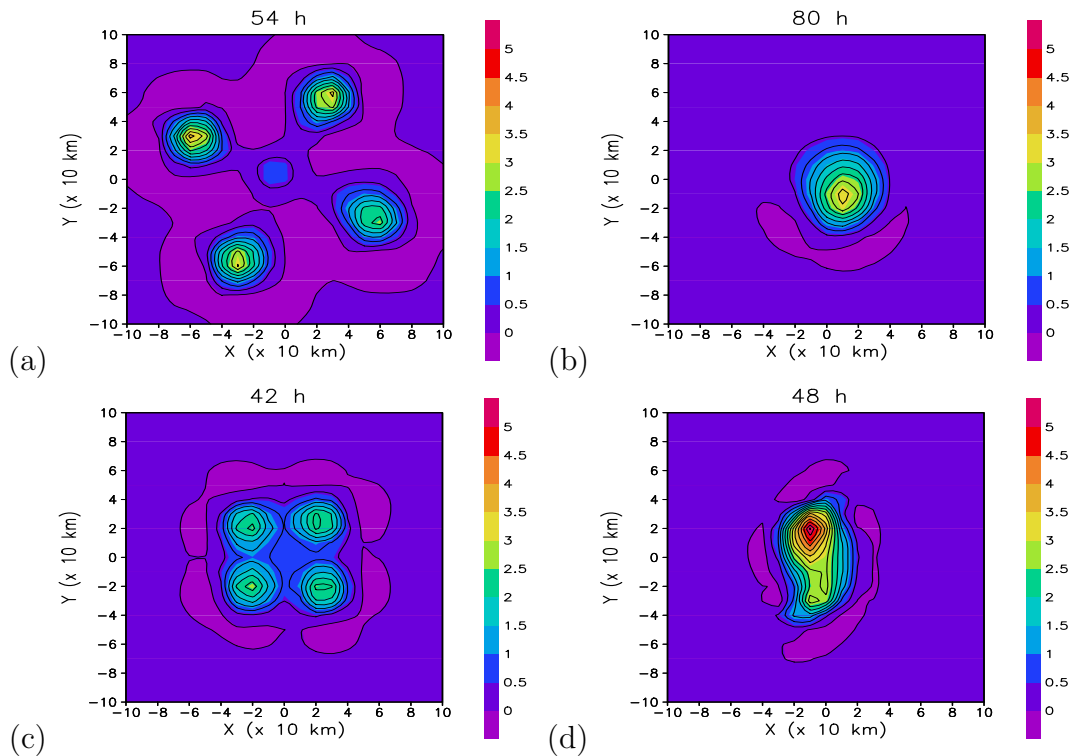


Figure 5.5: Vertical vorticity field at  $\sigma = 0.95$  in the calculations E02<sub>0</sub> at: (a) 54 h and (b) 80 h, and in E03<sub>0</sub> at: (c) 42 h and (d) 45 h. The contour interval is  $0.4 \text{ s}^{-1}$ .

Figure 5.6 shows the time-radius plot of the azimuthally-averaged absolute angular momentum at  $\sigma = 0.75$  in the calculations with strong radiative cooling (E02<sub>0</sub>) and without cooling (E03<sub>0</sub>). The angular momentum in the calculation E03<sub>0</sub> increases rapidly within a radius of 100 km after the meso-vortices begin to merge (Fig. 5.6b). However, the momentum increases rapidly only after about 66 h in E02<sub>0</sub>, which is consistent with the delayed onset of rapid intensification due to the reduced strength of the secondary circulation.

Ensemble integrations, E02<sub>1,2,3,4</sub> and E03<sub>1,2,3,4</sub> are carried out to seek the robust features of the calculation with strong radiative cooling. Moreover, the sensitivity of vortex intensification to the moisture perturbation in the boundary layer is investigated when the rate of radiative cooling is enhanced. Figure 5.7 shows time-series of the maximum, azimuthally-averaged, total wind speed in the ensemble calculations E02 and E03. The vortices in ensemble members of E02 begin to intensify 20-30 h later than in E03, displaying a similar intensification pattern to that in the calculation E02<sub>0</sub>.

A time-radius plot of the ensemble-mean, azimuthally-averaged vertical velocity shows that the reduced secondary circulation due to strong radiative cooling is a robust feature in E02. This reduced circulation is associated with the delayed onset of the rapid intensification in all ensemble members of E02 (Fig. 5.8). The ascent is weaker in the calculations with the strong radiative cooling (E02) than in the calculations without radiative cooling (E03). In

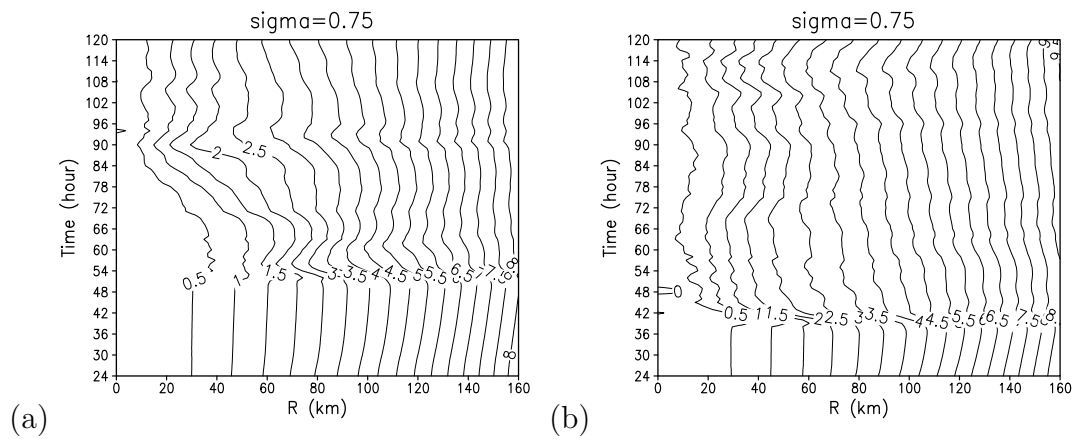


Figure 5.6: Time-radius plot of the azimuthally-averaged angular momentum per unit mass ( $10^7 \text{ m}^2 \text{ s}^{-2}$ ) at  $\sigma = 0.95$  between 24 and 120 h in the calculations (a) E02<sub>0</sub> and (b) E03<sub>0</sub>.

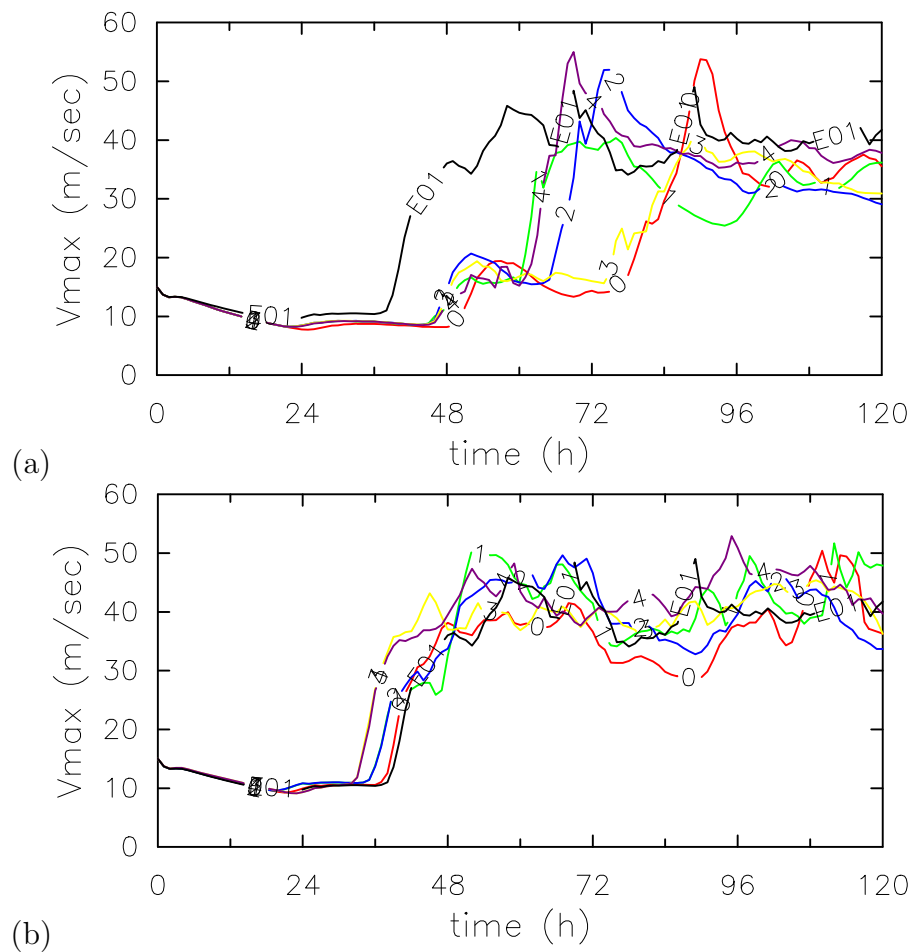


Figure 5.7: Time-series of azimuthally-averaged total wind speed maximum ( $V_{max}$ ) at  $\sigma = 0.95$  in the calculations (a) E02<sub>0,1,2,3,4</sub> and (b) E03<sub>0,1,2,3,4</sub>. The time-series of  $V_{max}$  in the calculation E01<sub>0</sub> is denoted by E01 in each panel.

E02 the ascent increases after about 72 h when the radial gradient of buoyancy in the core begins to increase, while in E03 the ascent increases rapidly after 36 h.

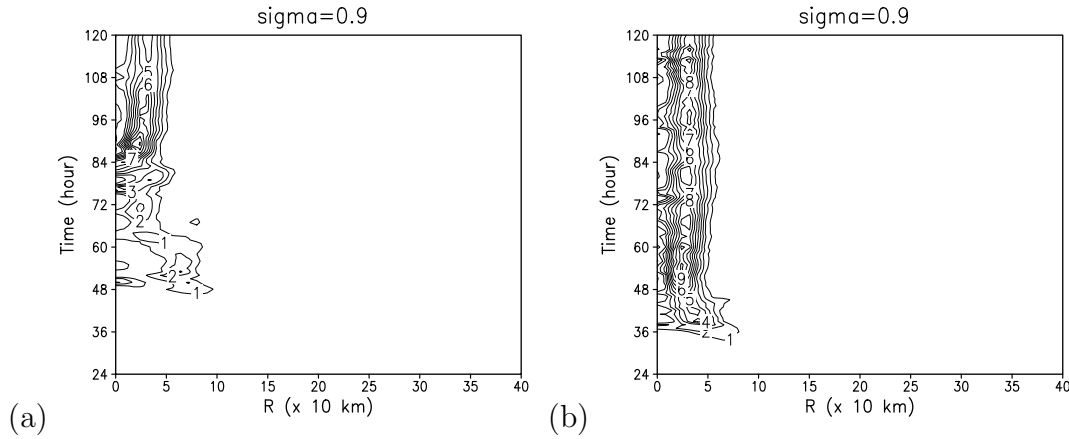


Figure 5.8: Time-radius plot of ensemble-mean, azimuthally-averaged the vertical velocity  $\bar{\sigma}$  at  $\sigma = 0.9$  between 24 h and 120 h in the experiment sets (a) E02 and (b) E03. Only the magnitude of ascent is plotted. The contour interval is  $1 \times 10^{-5} \text{ s}^{-1}$ .

If the ensemble members at a given time are more coherent (small ensemble spread in intensity) the vortex intensity is more predictable than if the members diverge (large ensemble spread). In both experiment sets E02 and E03 the ensemble spread in intensity arises during the period of rapid intensification (Fig. 5.8). The ensemble spread during the intensification phase in E02 is larger than that in E03 and in the control experiment (E01). In this sense the predictability of vortex intensity is lower in the calculations with the enhanced rate of radiative cooling than in other experiment sets. The large ensemble spread in E02 indicates that the intensity prediction in a single calculation is not reliable during the period of intensification. On the other hand, the intensity of the mature cyclone is more predictable. The ensemble spread in intensity diminishes during the mature stage in the both experiment sets E02 and E03. The ensemble spread does not exceed  $10 \text{ m s}^{-1}$  during this stage, similar to the fluctuations of intensity in the control run. The results for the ensemble calculations indicate that vortex intensification is highly sensitive to the boundary-layer moisture content, but the mature intensity is only weakly sensitive.

Figure 5.10 compares time-series of the upper and lower bounds of the maximum, azimuthally-averaged, total wind speed in the ensemble experiment sets E02 and E03 with those in E01. The area surrounded by the two bounds represents a deviation envelope for each experiment. The deviation envelope of E01 and E03 match nearly exactly except between 32 and 48 h, during the rapid intensification phase. The deviation envelope E02 bears little resemblance to that of E01 during the intensification period, but largely overlaps that of E01 after 84 h, during the mature stage. The comparison of the deviation envelopes shows that vortex intensification becomes more sensitive to the moisture perturbation when the radiative cooling is strong (E02). Moreover, the large deviation in E02 shows that the predictability of vortex intensity is lower than in other experiment sets.

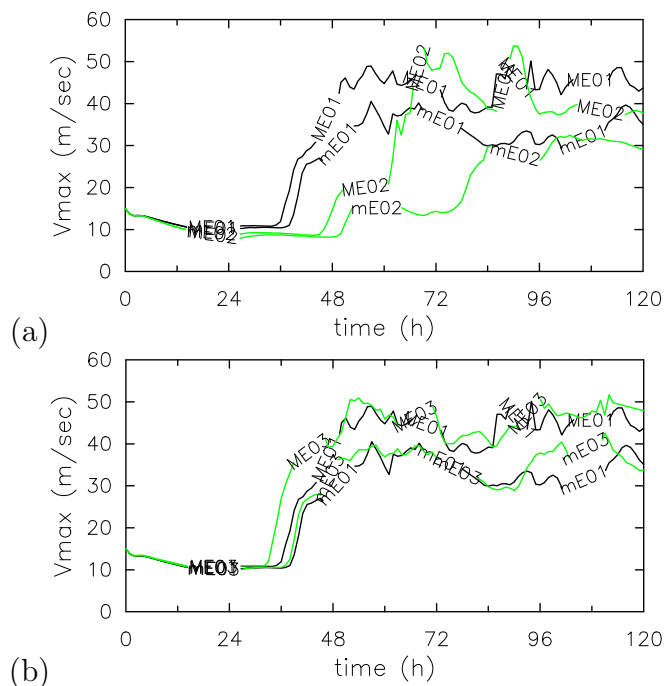


Figure 5.9: Time-series of the upper bounds (ME02, ME03) and lower bounds (mE02, mE03) of  $V_{max}$  at  $\sigma = 0.95$  in the experiment sets: (a) E02, and (b) E03, in comparison to those in E01 (ME01, mE01).

### 5.3 Dryness in the middle-troposphere

Strong variability of tropospheric humidity above the boundary layer has been observed over the Pacific Ocean during the Tropical Ocean Global Atmosphere Coupled Ocean-Atmosphere Response Experiment (TOGA COARE) campaign (Mapes and Zuidema 1996). Some studies have noted that extremely dry layers were found often in the Tropics (e.g. Roca *et al.* 2005). The dry layers were shown to originate from the extra-tropical upper-troposphere when an upper-level trough turns anticyclonically and extends equatorwards, bringing stratospheric dry air that had subsided to the middle-troposphere (Yoneyama and Parsons 1999). A similar drying was observed also in the Theodore and Rewa cases as discussed in Chapter 3.

It has been suggested that middle-tropospheric dry air inhibits deep convection (e.g. Yoneyama and Parsons 1999). The onset time of vortex intensification increased with the decrease of the initial low-tropospheric humidity in an axisymmetric calculation (Emanuel 1989). The large relative humidity in the lower and middle troposphere has been suggested to be conducive to tropical cyclogenesis (Gray 1968). Raymond (1998) showed on the basis of the aircraft observations that the middle-tropospheric dry air penetrated into the core region of tropical storm Fefa (1991) ( $\sim 17 \text{ m s}^{-1}$ ). This penetration coincided with the decrease of the boundary layer equivalent potential temperature. This decrease was followed in a few hours by the collapse of the warm core of Fefa and a significant decrease of the vertical mass flux. Raymond (1998) speculated that the decrease of the upward mass flux was caused by the decrease of the boundary-layer mixing ratio, but he recognized also

that more evidence was required to conclude the relationship between the dry air intrusion and the weakening of the warm core. The deep convection was suppressed in the region of dry advection in the cases of Rewa and Theodore, which is consistent with the scarcity of clouds in satellite images (see Chapter 3). However, the intensity of the severe tropical cyclones Rewa and Theodore remained unchanged for about a day when the dry ambient air was advected close to their eye-wall region. According to the ECMWF re-analysis there was no evident decrease in the boundary-layer mixing ratio around the cyclone centre in these cases. Two questions then arise: how is an intensifying storm influenced by the decrease of the middle-tropospheric mixing ratio and does a mature cyclone maintain its intensity despite the low middle-tropospheric humidity?

Two sets of experiment are carried out to examine these questions by decreasing the mixing ratio above  $\sigma = 0.6$ . In experiment E04<sub>0</sub>, the initial mixing ratio is 50 % of that in the control experiment and in E05<sub>0</sub> it is only 20 %. Figure 5.10 shows a vertical cross-section of the initial relative humidity that results from the reduction of the mixing ratio. The relative humidity is about 10 % between  $\sigma = 0.3$  and 0.1 in E04<sub>0</sub> and above  $\sigma = 0.5$  in E05<sub>0</sub>, showing the extremely dryness in the middle-troposphere. The vertical distribution of the humidity in E04<sub>0</sub> is similar to that observed to the west of Rewa and Theodore in Chapter 4. In this section, I investigate whether the decrease of the middle-tropospheric mixing ratio influences the strength of the secondary circulation and thereby the merging process of the meso-vortices.

Figure 5.11 compares time-series of the maximum, azimuthally-averaged, total wind speed in E04<sub>0</sub> and E05<sub>0</sub> with those in the control run E01<sub>0</sub>. In the former calculations the wind speed increases rapidly as soon as the grid-scale saturation occurs at about 20 h, while it increases more slowly until about 38 h in the control run. The increase of the maximum wind speed after the onset of the grid-scale saturation enhances the surface moisture fluxes which increase the boundary layer mixing ratio and thereby CAPE. Figure 5.12 shows the distribution of CAPE at 21 h, after the onset of the grid-scale saturation, in the calculations with the low middle-tropospheric mixing ratio (E04<sub>0</sub> and E05<sub>0</sub>). The mean value of the CAPE over the square area of 200 km  $\times$  200 km is 873 J kg<sup>-1</sup> in E04<sub>0</sub> and 929 J kg<sup>-1</sup> in E05<sub>0</sub>, while it is 784 J kg<sup>-1</sup> in the control run. The higher CAPE results in a stronger ascent in the eye-wall region in E04<sub>0</sub> and E05<sub>0</sub>. Figure 5.13 shows the relative humidity and vertical velocity field at 21 h, after the onset of the grid-scale saturation, in the calculation E04<sub>0</sub> and in the control run E01<sub>0</sub>. In both calculations, the grid-boxes are saturated at  $\sigma = 0.9$  within a radius of 80 km. The ascent is stronger in E04<sub>0</sub> than in the control run, which is consistent with the larger CAPE in E04<sub>0</sub> at this time. Accordingly, the meso-vortices develop and the vortex begins to intensify earlier than in the control run. The meso-vortices form at about 24 h in E04<sub>0</sub> and about 21 h in E05<sub>0</sub>, about 12 h earlier than in the control run. However, Fig. 5.11 shows that the azimuthally-averaged total wind speed maximum decreases after 36 h in the calculation E04<sub>0</sub> and 34 h in E05<sub>0</sub>. The decay of vortex intensity indicates that the secondary circulation weakens before the vortex reaches the intensity of a severe tropical cyclone ( $> 33 \text{ m s}^{-1}$ ) in these calculations.

The reason for the reduced strength of the secondary circulation is examined. The strength of the secondary circulation is associated with the buoyancy of air parcels in deep clouds. Since the buoyancy is dependent on the boundary-layer mixing ratio, it is examined whether

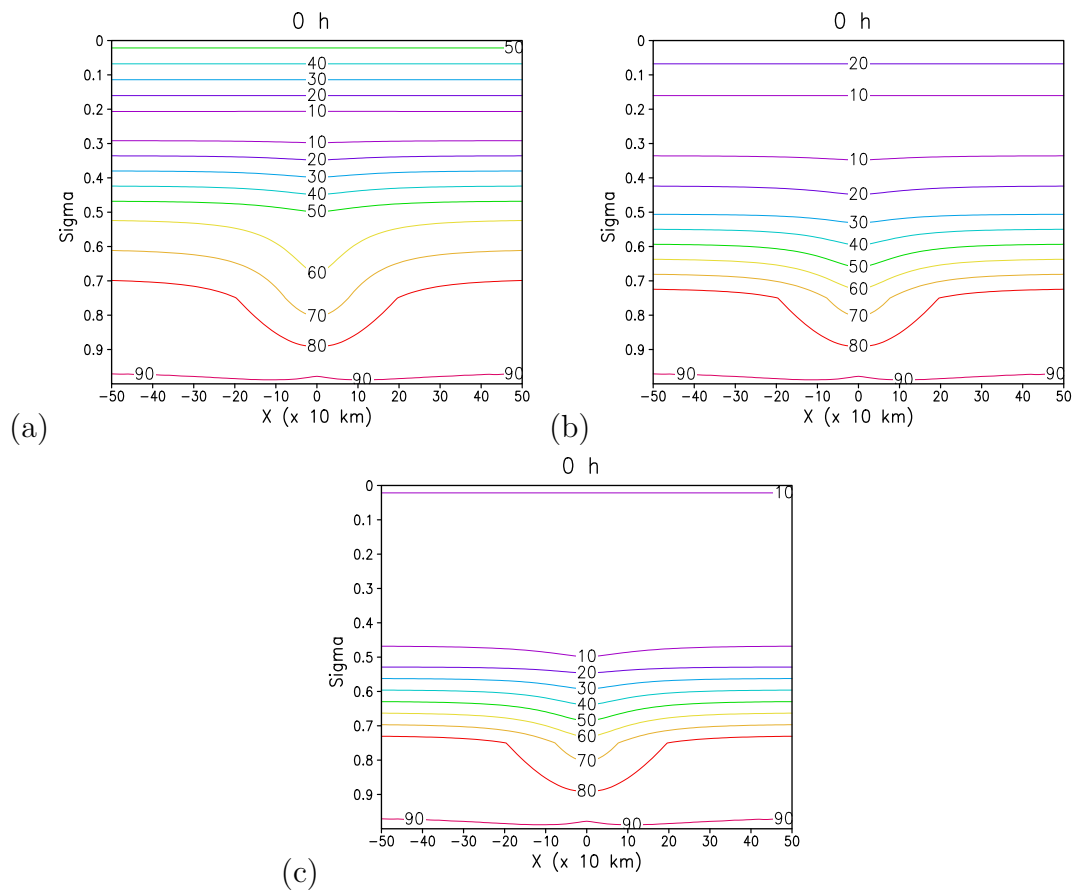


Figure 5.10: Height-radius plot of the initial relative humidity (%) in the calculations: (a) E01<sub>0</sub>, (b) E04<sub>0</sub> and (c) E05<sub>0</sub>.

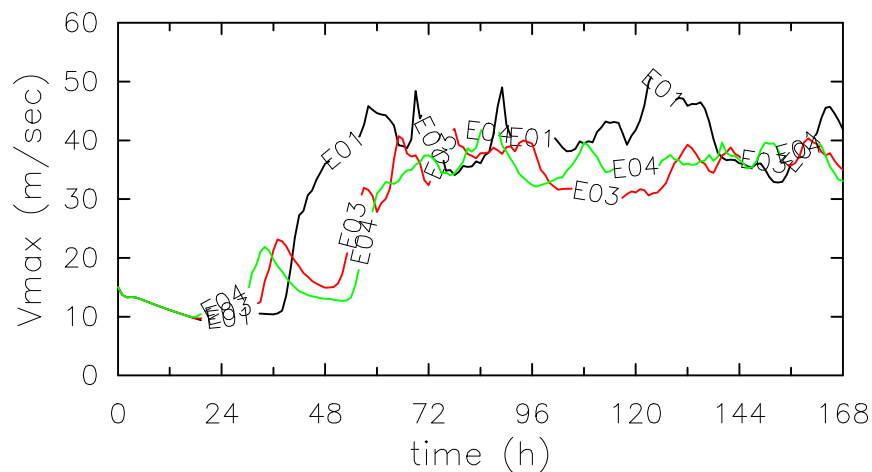


Figure 5.11: Time-series of azimuthally-averaged wind speed maximum ( $V_{max}$ ) at  $\sigma = 0.95$  in the calculations E04<sub>0</sub> and E05<sub>0</sub>. The label E01 indicates the time-series in the control run E01<sub>0</sub>.

the reduced secondary circulation is related to a decrease of the mixing ratio in the boundary layer. Figure 5.14 compares the mixing ratio at  $\sigma = 0.9$ , averaged during the period

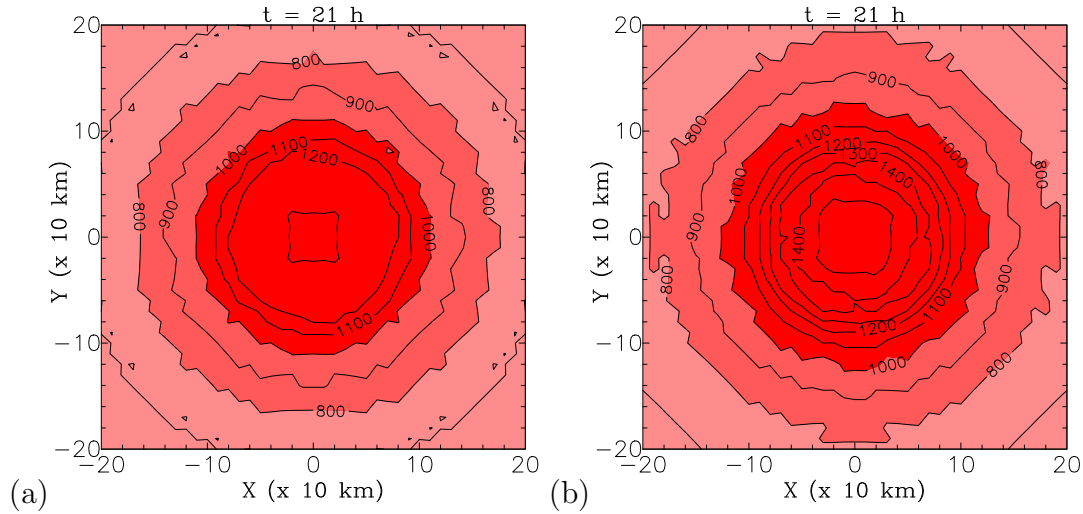


Figure 5.12: Initial CAPE values in the calculations (a) E04<sub>0</sub> and (b) E05<sub>0</sub>. The CAPE is calculated for parcels lifted from the 500 m level assuming the reversible process. The shading starts from 200 J kg<sup>-1</sup> and increases in intervals of 200 J kg<sup>-1</sup>.

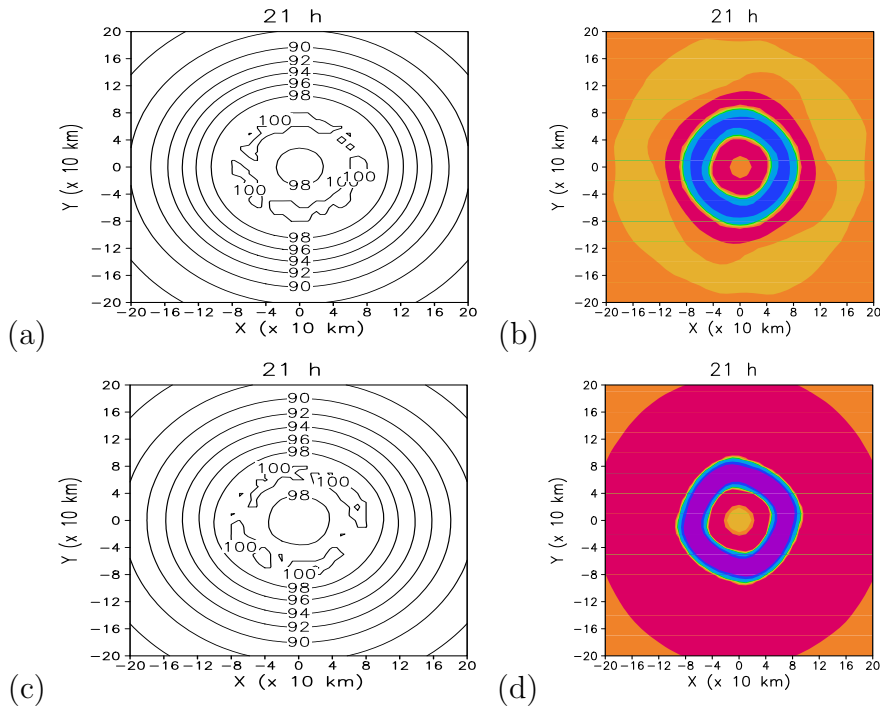


Figure 5.13: Distribution of the relative humidity (%) and the vertical velocity  $\dot{\sigma}$  ( $1 \times 10^{-1} \text{ s}^{-1}$ ) at  $\sigma = 0.9$  at 21 h in the calculations E01<sub>0</sub> (upper panels) and E04<sub>0</sub> (lower panels).

35-40 h, in the calculation with the low middle-tropospheric humidity (E04<sub>0</sub>) with that in the control run. The mixing ratio is about 1.5 g kg<sup>-1</sup> lower at radii between 40 and 80 km, in the region of ascent, than that in the control calculation. The difference in the mixing ratio between the two calculations is greater at outer radii. The mixing ratio is about 3.0 g kg<sup>-1</sup> lower in E04<sub>0</sub>. This large difference results from the subsidence of the dry

middle-tropospheric air into the boundary layer. The subsidence in a broad annular area outside the region of ascent at the earlier stage of intensification is shown in Fig. 5.13d. The dry air is advected with the radial inflow and reduces the boundary-layer mixing ratio in the region of ascent. Subsequently, the buoyancy in deep clouds in E04<sub>0</sub> is weaker than that in the control run.

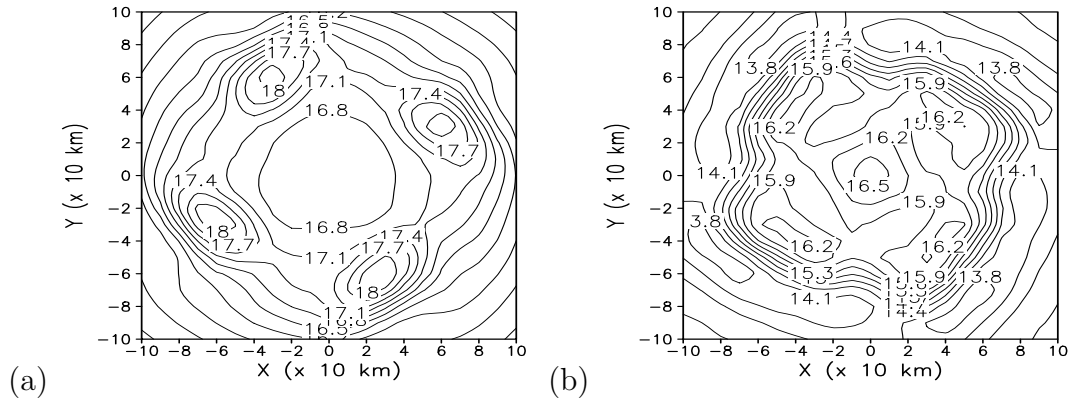


Figure 5.14: The mixing ratio at  $\sigma = 0.9$  averaged during the period 35-40 h in the calculations (a) E01<sub>0</sub> and (b) E04<sub>0</sub>. The contour interval is  $0.3 \text{ g kg}^{-1}$ .

The reduction of the buoyancy is consistent with the weaker radial inflow in the calculations with the dry middle-tropospheric atmosphere (E04<sub>0</sub> and E05<sub>0</sub>), compared with that in the control run E01<sub>0</sub>. Figure 5.15 compares the azimuthally-averaged radial wind in E04<sub>0</sub> and E05<sub>0</sub> at  $\sigma = 0.95$ , averaged at radii between 40 and 80 km with that in E01<sub>0</sub>. The inflow increases rapidly after 38 h, when the meso-vortices appear in the control run E01<sub>0</sub> (Fig. 5.15a). On the other hand, the rapid increase of the inflow occurs after 50 h in the calculations with the low middle-tropospheric mixing ratio (E04<sub>0</sub> and E05<sub>0</sub>) although there is an increase of the radial flow for a short period after the formation of the meso-vortices (Fig. 5.15b, c). The pattern of the inflow-speed changes is similar to that of the evolution of vortex intensity. The weaker buoyancy and radial inflow represent a reduced secondary circulation that results in the vortex intensification at a lower rate in E04<sub>0</sub> and E05<sub>0</sub> than in the control calculation. During the mature stage, vortex intensity is similar to that in the control run.

Ensemble calculations are carried out to examine the robustness of the results in the calculations with the middle-tropospheric dryness (E4<sub>0</sub> and E05<sub>0</sub>). Figure 5.16 compares time-series of the maximum, azimuthally-averaged, total wind speed in the ensemble calculations E04<sub>0,1,2,3,4</sub> and E05<sub>0,1,2,3,4</sub> with those in the control run E01<sub>0</sub>. The pattern of the vortex intensification in the four ensemble calculations in each set of experiments is similar to those in E04<sub>0</sub> and E05<sub>0</sub>. The delayed onset of rapid intensification due to the low middle-tropospheric mixing ratio is common in all ensemble calculations of E04 and E05.

The buoyancy of air parcels in deep clouds is shown to be reduced due to the decrease of the boundary-layer mixing ratio in the region of ascent in the calculations E04<sub>0</sub> and E05<sub>0</sub>. The decrease of the mixing ratio is a robust feature that survives the ensemble-mean. Figure 5.17 compares the ensemble-mean of the azimuthally-averaged mixing ratio at  $\sigma =$

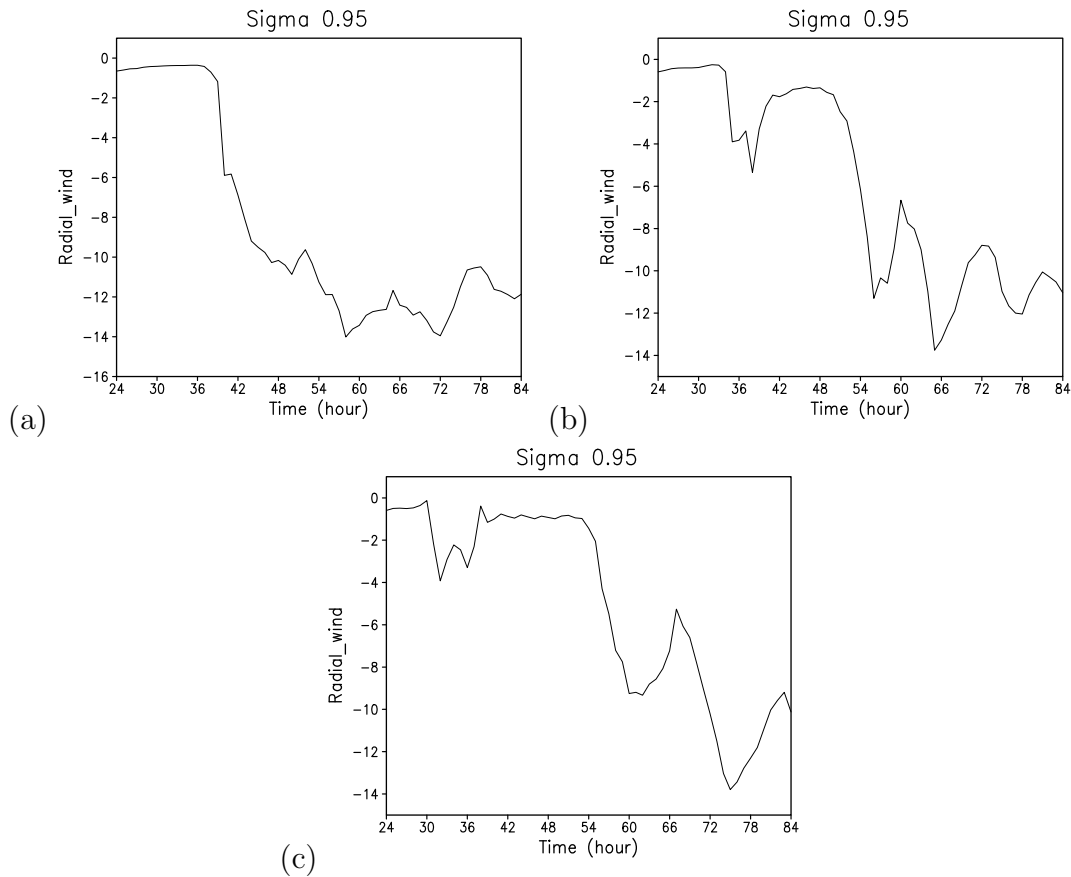


Figure 5.15: Time-series of the azimuthally-averaged radial wind ( $\text{m s}^{-1}$ ) at  $\sigma = 0.95$  between 24 h and 84 h in the calculations (a) E01<sub>0</sub>, (b) E04<sub>0</sub>, and (c) E05<sub>0</sub>. The radial wind is averaged at radii between 40 km and 80 km.

0.9 (near the top of the boundary layer) in the experiment sets E04 and E05 with that in the control experiment E01. In E04 and E05, the mixing ratio in the boundary layer increases rapidly in the region of strong updraft at radii between 50 and 100 km after the onset of the grid-scale saturation (about 20 h). However, it begins to decrease after about 30 h when the drier air is advected inwards from the region of subsidence. In contrast, in the control experiment, the mixing ratio increases rapidly within a radius of 50 km as the meso-vortices merge. Subsequently, the radial gradient of the boundary-layer mixing ratio increases steeply when the monopole of intense vorticity forms. However, it takes longer for the radial gradient of the mixing ratio to increase in E04 and E05 because the formation of the monopole is delayed due to the reduced strength of the secondary circulation.

The decrease of the boundary-layer mixing ratio in the region of ascent is consistent with the weaker ascending motion in the eye-wall region in E04 and E05 than in the control experiment. Figure 5.18 compares the ensemble-mean of the azimuthally-averaged vertical velocity in the experiment sets E04 and E05 with that in the control experiment. The ascending motion begins to increase earlier in the calculations with the dry middle-tropospheric environment (E04 and E05) after the onset of the grid-scale saturation than in the control experiment. However, the ascending motion weakens after 36 h, when

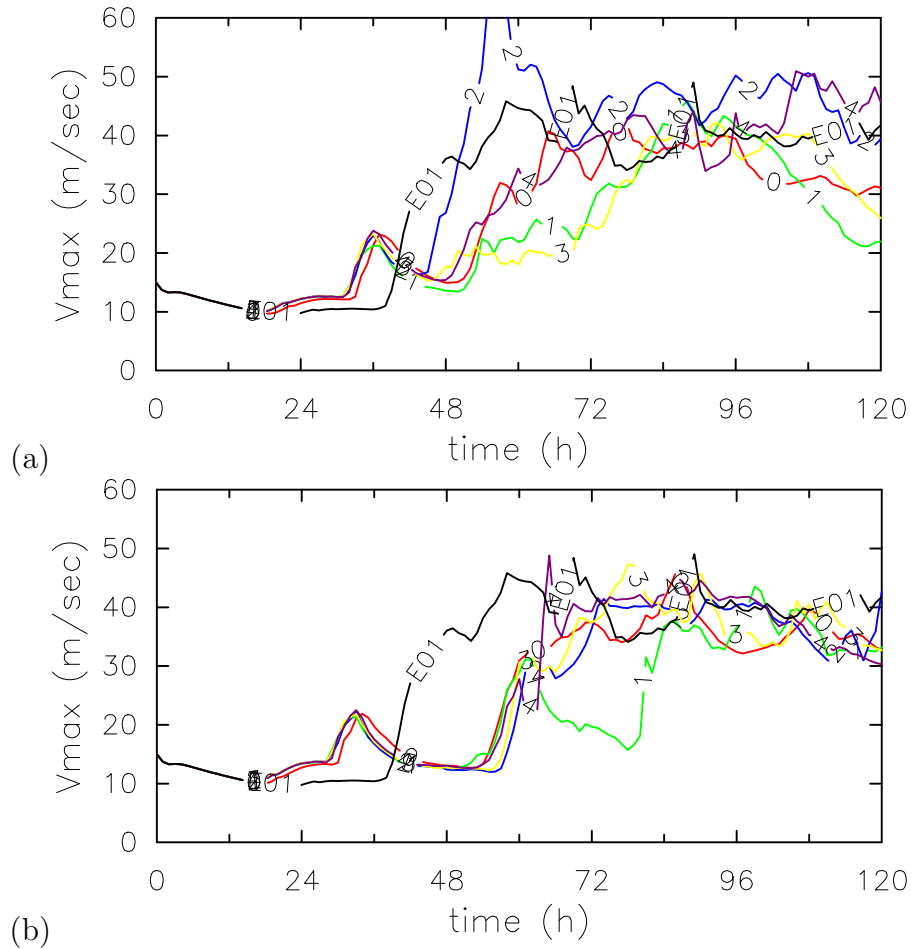


Figure 5.16: Time-series of azimuthally-averaged wind speed maximum ( $V_{max}$ ) at  $\sigma = 0.95$  in the calculations (a)  $E04_{0,1,2,3,4}$  and (b)  $E5_{0,1,2,3,4}$ . The numbers indicate each ensemble calculation in the experiment sets E04 and E05. The time-series of  $V_{max}$  in  $E01_0$  is denoted by E01.

the boundary-layer mixing ratio within a radius of 80 km decreases. The ascent strengthens again as the radial gradient of the mixing ratio within a radius of 50 km becomes as large as that in the control experiment. The onset of rapid intensification coincides with the sharp increase of the ascending motion and of the radial gradient of the mixing ratio.

The vortex intensification in the calculations with the low middle-tropospheric humidity is found to be more sensitive to the boundary-layer moisture perturbation than in the control experiment (see Fig. 5.16). Subsequently, the predictability of the intensity of the vortex is lower than in the control experiment. Figure 5.19 compares time-series of the upper and lower bounds of the azimuthally-averaged total wind speed maximum in the ensemble experiment sets E04 and E05 with those in E01. The area surrounded by the two bounds characterizes a deviation envelope for each experiment. The width of this envelope remains small until the vortex begins to intensify in all experiments. As the ensemble spread in intensity arises during the intensification phase, the deviation envelope of E04 and E05 bears little resemblance to that of E01. The width of the envelope in experiment E04 is found to be four times as large as that in E01 between 48 and 72 h. The width

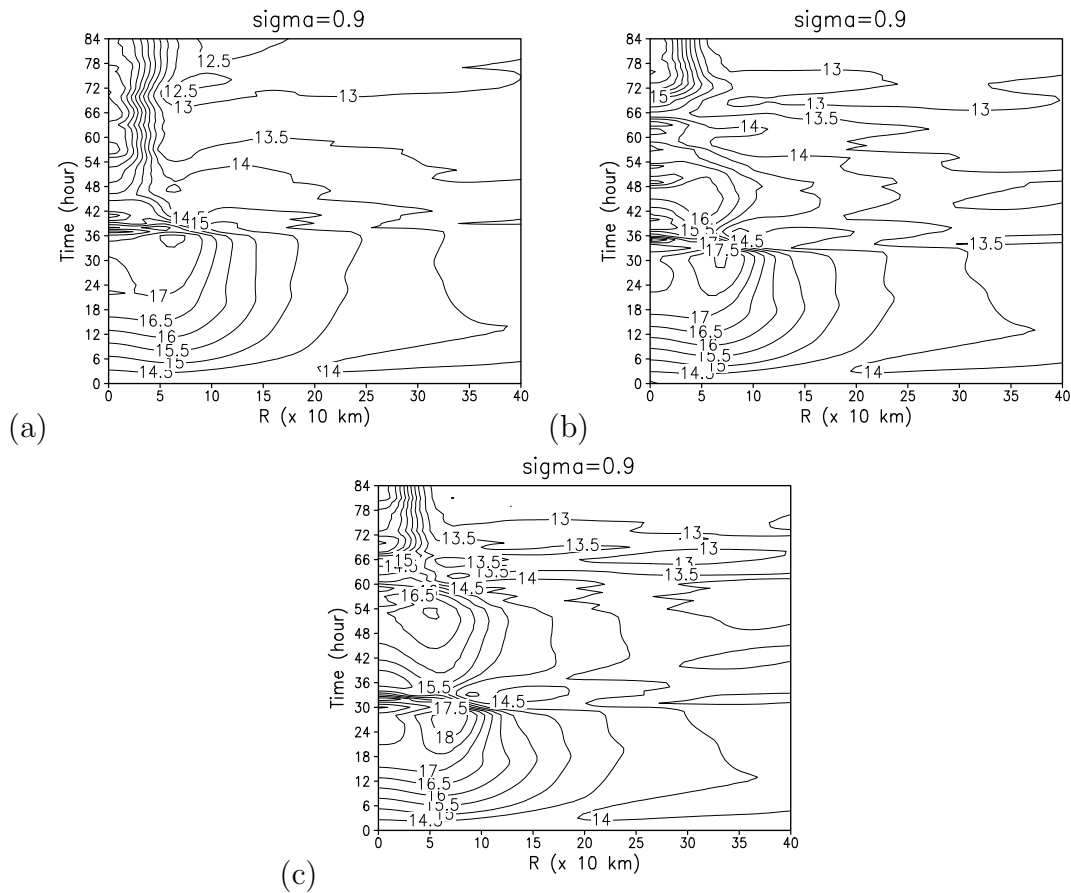


Figure 5.17: Time-radius plot of the ensemble-mean, azimuthally-averaged mixing ratio ( $\text{kg}^{-1}$ ) at  $\sigma = 0.9$  between 0 and 84 h in the experiment sets (a) E01, (b) E04 and (c) E05.

in E05 is three times as large as that in E01 between 60 and 78 h. The large deviation during the intensification phase demonstrates that the evolution of vortex intensity is less predictable than in the control experiment. The significant ensemble spread is related to the different rates-of-increase of the radial gradient of the boundary-layer mixing ratio between ensemble members. Figure 5.20 compares the azimuthally-averaged mixing ratio at  $\sigma = 0.9$  in E04<sub>0,2,4</sub> with that in E04<sub>1,3</sub>. The vortex intensifies more rapidly in the first group than in the second (E04<sub>1,3</sub>). The lower intensification rate in E04<sub>1,3</sub> coincides with the lower rate-of-increase of the radial gradient of boundary-layer mixing ratio (Fig. 5.20b). The gradient begins to rapidly increase only after 70 h in E04<sub>1,3</sub>, while it increases after 60 h in the other ensemble members. Moreover, the radial gradient of the mixing ratio decreases after 100 h in the two ensemble members E04<sub>1,3</sub>, which coincides with the decay of the vortex in these calculations. However, the gradient and the intensity remain nearly steady in other members (Fig. 5.20a) so that the ensemble spread arises at the later stage of integration (Fig. 5.19a). This result shows the limitations of inferring differences in vortex intensification from a comparison of two single calculations.

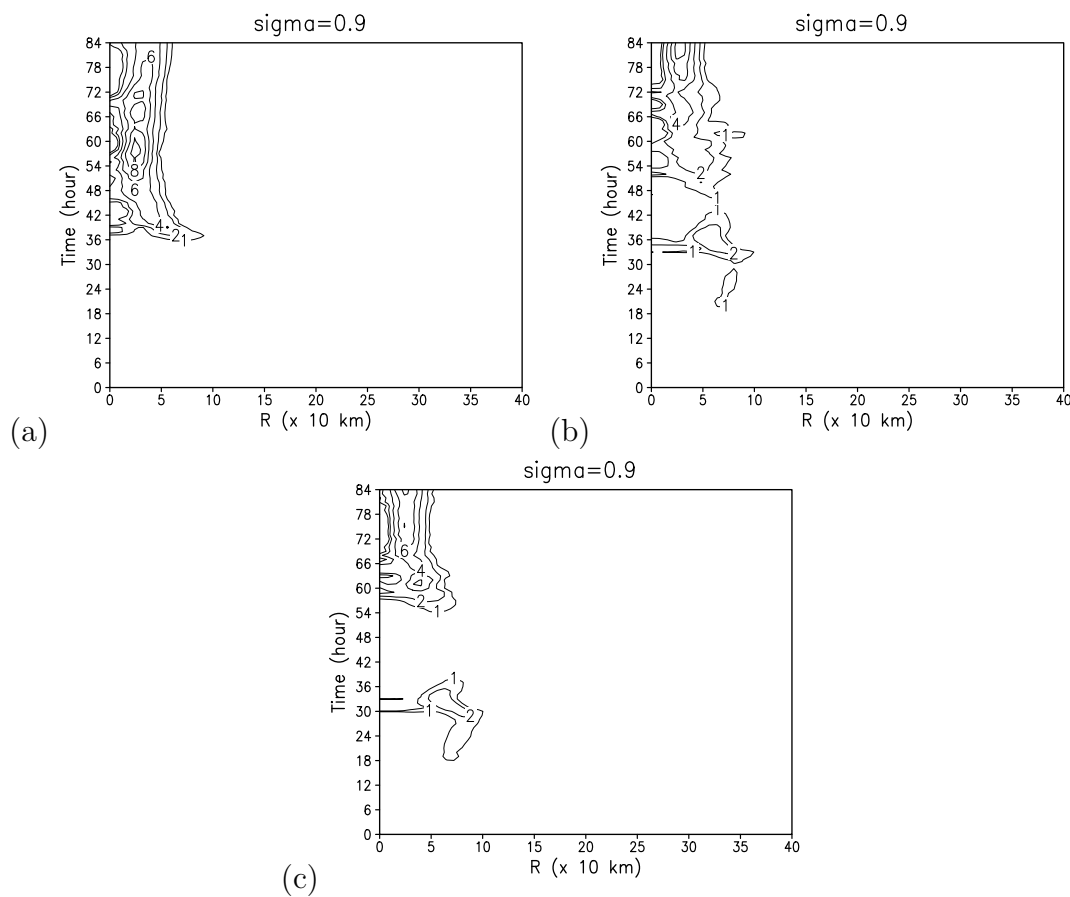


Figure 5.18: Time-radius plot of the azimuthally-averaged vertical velocity ( $\bar{\sigma}$ ) at  $\sigma = 0.9$  between 0 h and 84 h in the experiment sets (a) E01, (b) E04, and (c) E05. Only the magnitude of ascent is plotted. The contour interval is  $1 \times 10^{-5} \text{ s}^{-1}$ .

## 5.4 Anticyclonic upper-level shear flow

Tropical cyclone outflow is the branch of the secondary circulation in the upper-troposphere. Merrill (1988) examined composite data sets of hurricanes in the Atlantic basin and noted that they have outflows that are organized into jets during their intensification phase. In contrast, storms that are not intensifying tend to have unidirectional upper-level flow across the cyclone centre. The outflow of a tropical cyclone is asymmetric, forming one or two anticyclonically curved outflow jets with various preferential patterns (Merrill 1988; Wu and Emanuel 1994). The organization of outflow jets occurs commonly through the interaction with a synoptic-scale flow (Sadler 1976). The outflow jets provide a so-called *outflow channel*, in which air of high potential temperature from the convective core spreads outwards to the far environment (Wu and Emanuel 1994). Sadler (1976) showed that a pair of outflow channel equatorward and poleward commonly coincided with the rapid intensification of typhoons in the north-west Pacific region. Ooyama (1987) suggested that the asymmetric outflow patterns with double outflow channels could be generated in the presence of an upper-level, anticyclonic, horizontal shear. However, the effect of the horizontal shear flow on the intensification of a tropical cyclone has been unexplored. Some

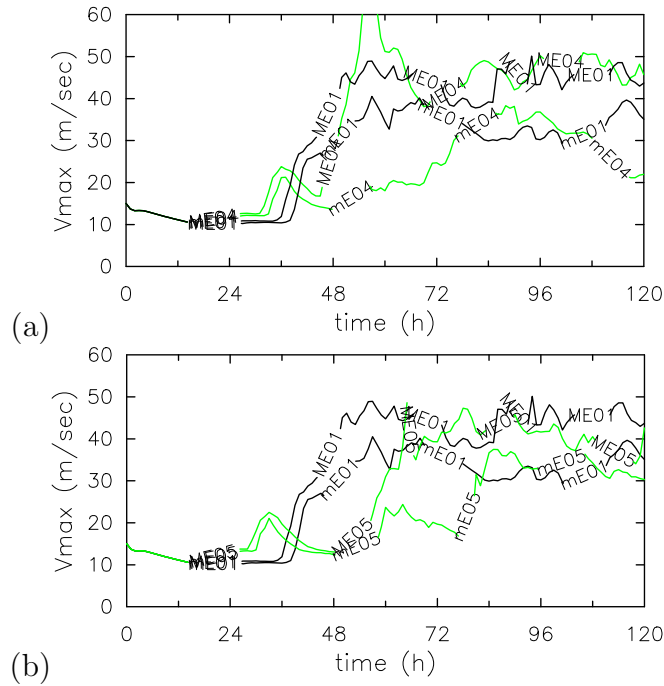


Figure 5.19: Time-series of the upper bounds (ME04, ME05) and lower (mE04, mE05) bounds of  $V_{max}$  at  $\sigma = 0.95$  in the experiment sets: (a) E04, and (b) E05, in comparison to those in E01.

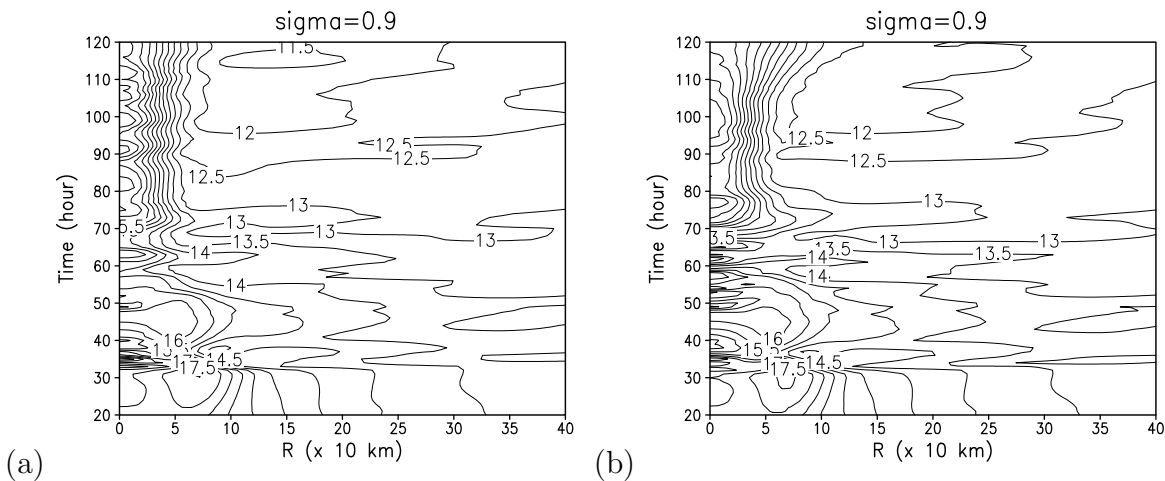


Figure 5.20: Time-radius plot of the azimuthally-averaged mixing ratio ( $\text{g kg}^{-1}$ ) at  $\sigma = 0.9$  between 20 and 120 h in the calculations (a)  $E04_{0,2,4}$  and (b)  $E04_{1,3}$ . The value of the mixing ratio is the mean of each group of ensemble members. The contour interval is  $0.5 \text{ g kg}^{-1}$ .

forecasters insist that such double outflow channels act to intensify a tropical cyclone by triggering convection through a *suction* mechanism (Smith 2006, personal communication). It is of special interest to examine whether the intensification rate of the vortex increases when there is an anticyclonic horizontal upper-level shear flow.

The influence of an upper-level anticyclonic shear flow on vortex intensification is investigated in three integrations by varying zonal shear strength as described in Table 5.1. The anticyclonic shear flow is imposed at the model-level  $\sigma = 0.15$  ( $k = 1$ ), where there is initially no motion in the previous experiments. Figure 5.21 shows the spatial distribution of the initial wind field at  $\sigma = 0.15$  in the calculations E06<sub>0</sub>, E07, and E08. The wind speed is 10 m s<sup>-1</sup> at  $y = \pm 1000$  km in the calculation E06<sub>0</sub>, 20 m s<sup>-1</sup> in E07, and 40 m s<sup>-1</sup> in E08.

Table 5.1: Description of experiments.

Experiment	Description
E06 <sub>0</sub>	$\frac{du}{dy} = 2.5 \times 10^{-6} \text{ s}^{-1} \text{sech}^2 \frac{y}{400000}$ .
E07	$\frac{du}{dy} = 5.0 \times 10^{-6} \text{ s}^{-1} \text{sech}^2 \frac{y}{400000}$ .
E08	$\frac{du}{dy} = 1.0 \times 10^{-5} \text{ s}^{-1} \text{sech}^2 \frac{y}{400000}$ .

Figure 5.22 shows the height-radius plot of the perturbation potential temperature at the initial time in the calculations E06<sub>0</sub>, E07 and E08. The positive perturbation aloft increases and the corresponding initial CAPE decreases with the strength of the upper-level anticyclonic shear, since the enhanced warm anomaly aloft stabilizes the atmosphere (Fig. 5.23). The mean value of the initial CAPE over the square area of 200 km  $\times$  200 km in E06<sub>0</sub> is 53 J kg<sup>-1</sup> (Fig. 5.23a), which is less than a quarter of that in the control run E01<sub>0</sub> (251 J kg<sup>-1</sup>). The mean of the initial CAPE in E07 is nearly zero (0.24 J kg<sup>-1</sup>) (Fig. 5.23b) and the atmosphere is initially stable to deep convection in E08.

As in the control calculation, the onset time of the grid-scale saturation is about 20 h. The values of CAPE increase during the gestation period due to the surface moisture fluxes in all calculations (Fig. 5.24). The mean value of the CAPE at 21 h over the square area of 200 km  $\times$  200 km is 525 J kg<sup>-1</sup> in the calculation with a weak shear flow (E06<sub>0</sub>), 342 J kg<sup>-1</sup> in E07 and 185 J kg<sup>-1</sup> in E08, compared with 530 J kg<sup>-1</sup> in the control run E01<sub>0</sub>. The increase of the mean CAPE during the gestation period decreases with the increasing strength of the upper-level shear flow. Although the boundary-layer mixing ratio is nearly the same as that in the control run (see Fig. 4.10), the CAPE is small due to the stabilization by the warm anomaly aloft in those calculations. The low convective instability is associated with a reduced strength of the secondary circulation, compared with that in the control run. Accordingly, the formation of the meso-vortices is delayed as the shear strength increases. The vortex intensifies at a reduced rate in the calculations with the upper-level shear flow.

The vortex reaches the intensity of a severe tropical cyclone ( $> 33 \text{ m s}^{-1}$ ) at about 58 h in the calculation with the weak shear flow (E06<sub>0</sub>), a half day later than in the control calculation E01<sub>0</sub> (Fig. 5.25). However, the intensity of vortices in E07 and E08 never exceeds 33 m s<sup>-1</sup> over the 7-day integration time. The height-radius plot of the azimuthally-averaged potential temperature perturbation (the mean between 72 and 120 h) shows that the warm core in the calculations E07 and E08 is less compact and weaker through the troposphere than in E06<sub>0</sub> and E01<sub>0</sub> (Fig. 5.26). There is a sharp radial gradient of the

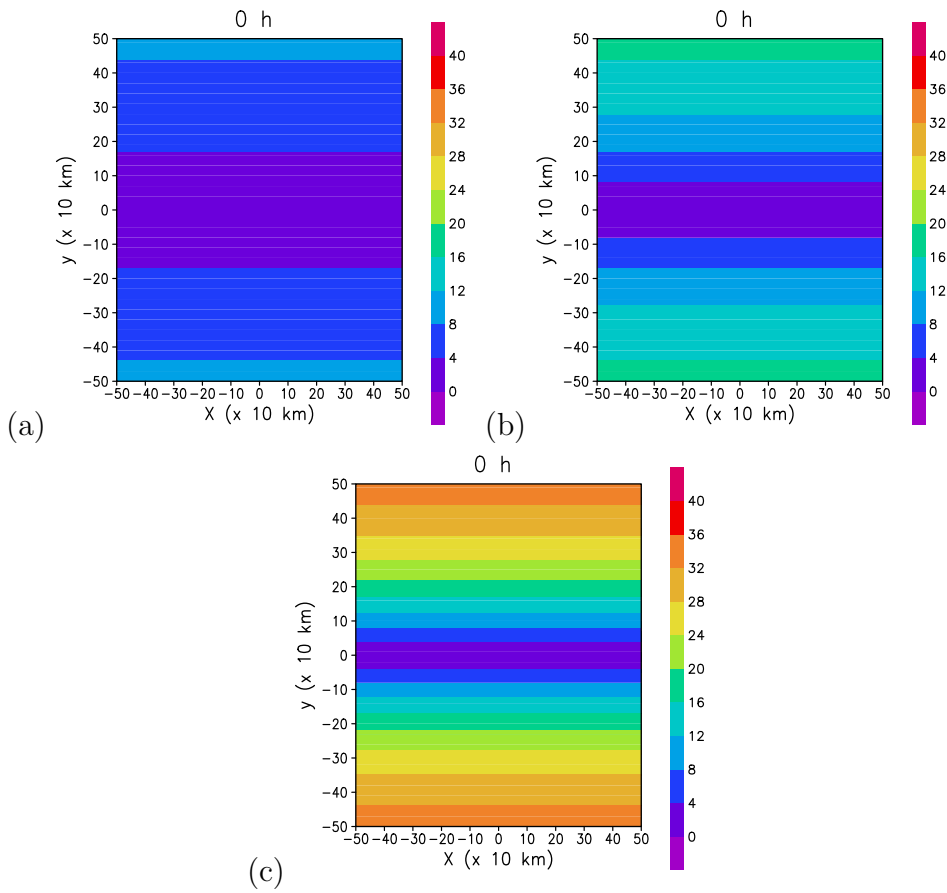


Figure 5.21: The initial total wind speed ( $\text{m s}^{-1}$ ) at  $\sigma = 0.15$  in the calculations: (a) E06<sub>0</sub>, (b) E07, and (c) E08. The color shading increases in intervals of  $4 \text{ m s}^{-1}$ .

azimuthally-averaged temperature perturbation within a radius of 50 km and the gradient increases with height in the calculations E06<sub>0</sub> and E01<sub>0</sub> (Fig. 5.26a, b). On the other hand, in the calculations E07 and E08 the radial gradient below  $\sigma = 0.7$  is relative small and the gradient at upper-levels is smaller compared with those in the previous calculations (Fig. 5.26c, d). The small increase of the radial gradient of buoyancy is consistent with the weaker intensity of the vortex.

Table 5.2 compares the mean intensity during the mature stage in the calculations E06<sub>0</sub>, E07, and E08 with that in E01<sub>0</sub>. It shows that maximum intensity decreases with the strength of the shear. However, the difference between the maximum intensity in E06<sub>0</sub> and E01<sub>0</sub> is only about  $4.9 \text{ m s}^{-1}$ , which is close to the standard deviation of the intensity in the ensemble integrations of the control experiment set E01. To determine whether intensity of the mature cyclone is unaffected by the weak anticyclonic shear flow, it is necessary to examine the intensity evolution in ensemble calculations.

Time-series of the maximum, azimuthally-averaged, total wind at  $\sigma = 0.95$  show that the wind speed in E06<sub>1,2,3,4</sub> begins to increase at about 38 h, which is the same time as in E01<sub>0</sub> (Fig. 5.27). As in the other ensemble calculations E01-E05, the random moisture perturbation in the boundary layer leads to a slight reduction of the time for the meso-

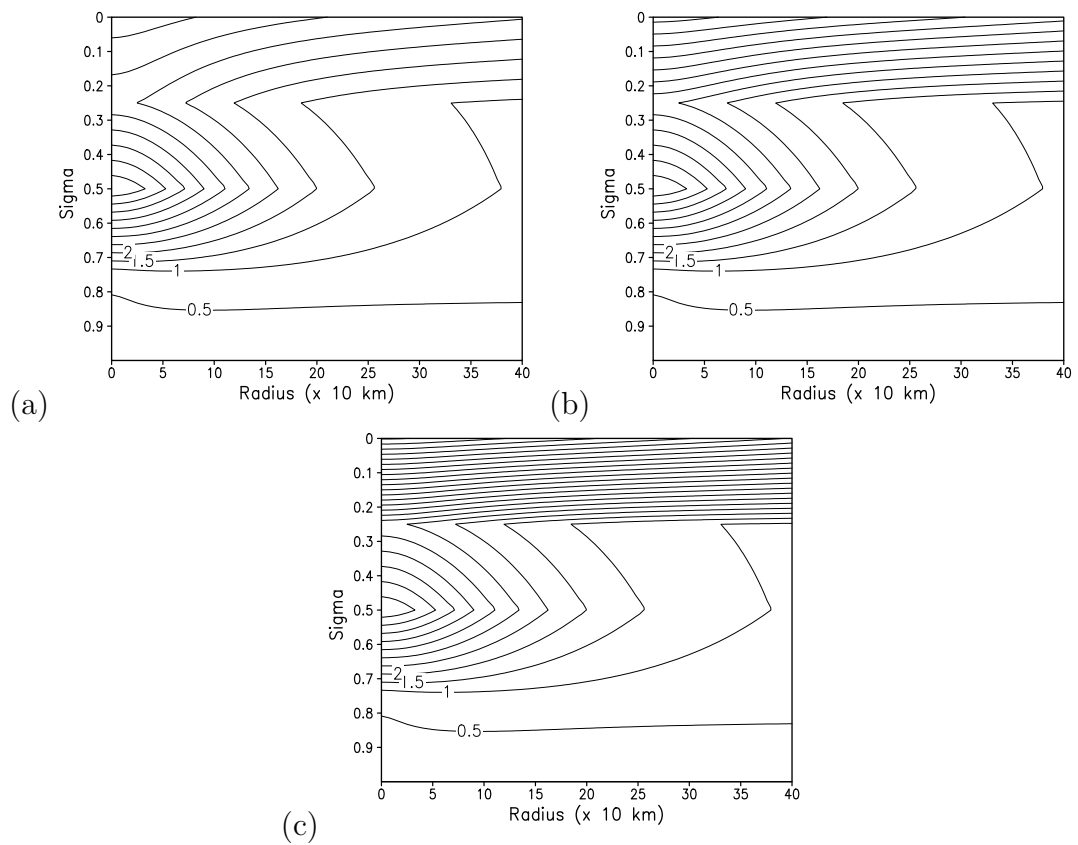


Figure 5.22: Height-radius plot of the initial azimuthally-averaged perturbation of potential temperature (K) in the calculations: (a) E06<sub>0</sub>, (b) E07, and (c) E08. The contour interval is 0.5 K.

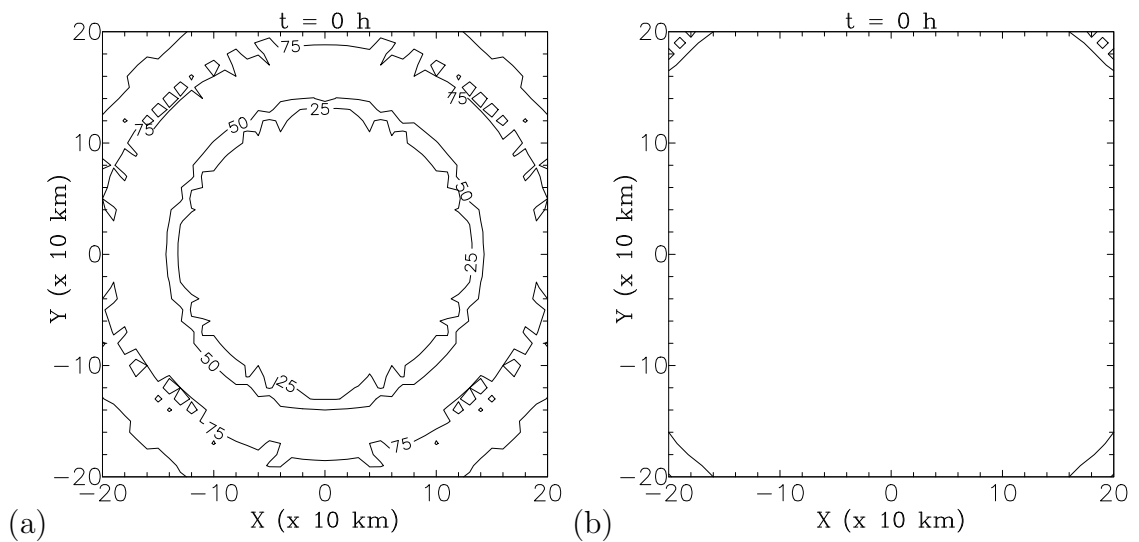


Figure 5.23: Initial CAPE values in the calculations (a) E06<sub>0</sub> and (b) E07. The CAPE is calculated for parcels lifted from the 500 m-level assuming the reversible process. The contour interval is 25 J kg<sup>-1</sup>.

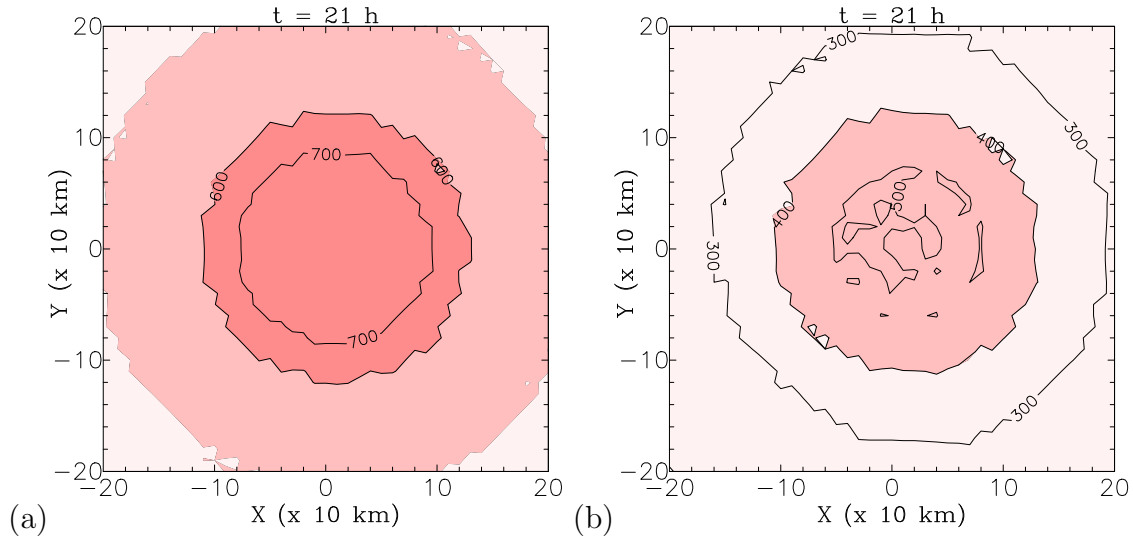


Figure 5.24: CAPE values at 21 h in the calculations (a) E06<sub>0</sub> and (b) E07. The CAPE is calculated for parcels lifted from the 500 m-level assuming a reversible adiabatic process. The shading starts from 200 J kg<sup>-1</sup> and increases in intervals of 200 J kg<sup>-1</sup>.

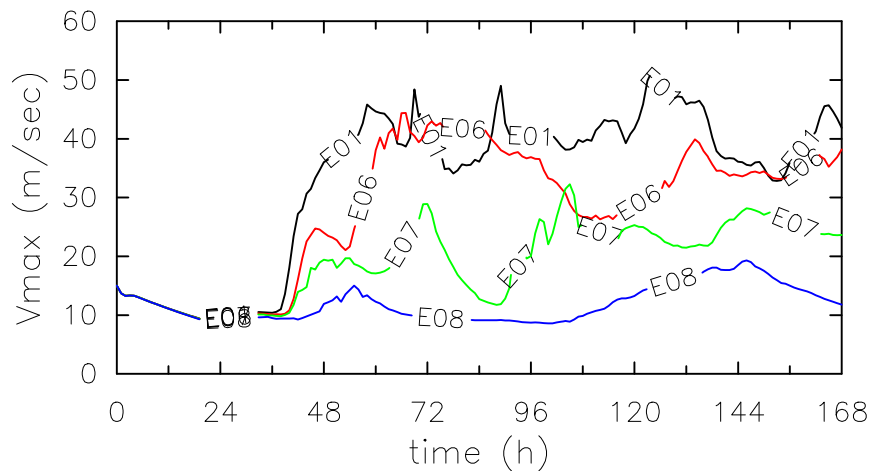


Figure 5.25: Time-series of the azimuthally-averaged wind speed maximum ( $V_{max}$ ) at  $\sigma = 0.95$  around the centre of the weighted vorticity in the calculations of E06, E07, E08 and control calculation of E01<sub>0</sub> (denoted by E01).

vortices to form. The vortices in the ensemble members of E06 reach hurricane intensity ( $33 \text{ m s}^{-1}$ ) 1-2 days later than that in the control run, indicating that a reduction in the rate of vortex intensification is a robust feature of the calculation with an upper-level shear flow. The results of the ensemble calculations show that the presence of the anticyclonic shear flow does not enhance the intensification rate, but actually reduces it. The stabilization due to the enhanced warm anomaly aloft reduces the strength of the secondary circulation and thereby delays the onset of rapid intensification.

The vertical velocity at the early stage of the merging process is examined to find a reduction of the secondary circulation in the experiment with the upper-level shear flow. Figure

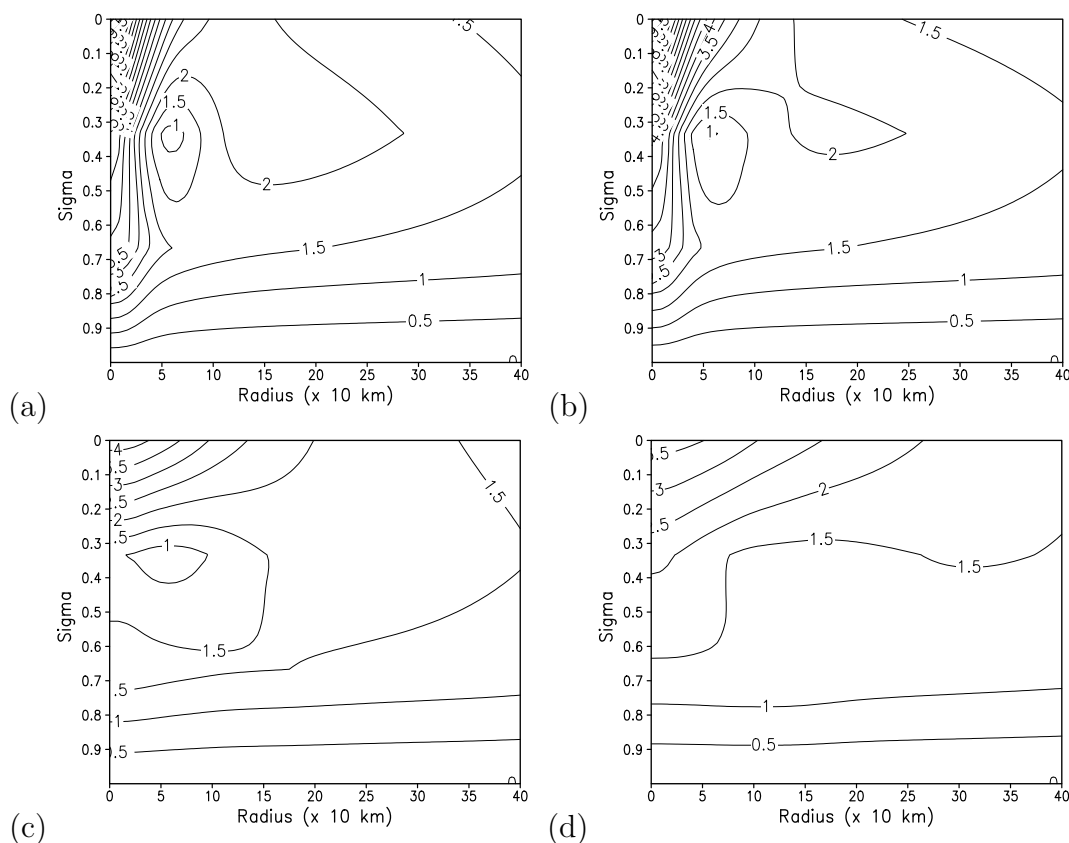


Figure 5.26: Height-radius plot of the azimuthally-averaged potential temperature perturbation, which is averaged over the period 72 - 120 h in the calculations: (a) E01<sub>0</sub>, (b) E06<sub>0</sub>, (c) E07, and (d) E08. The contour interval is 0.5 K.

Table 5.2: A summary of results from the calculations with an anticyclonic horizontal shear flow at  $\sigma = 0.15$ .

Experiment	Averaged wind speed maximum during the mature stage
E01 <sub>0</sub>	40.3 m s <sup>-1</sup> from t = 46 to t = 168
E06 <sub>0</sub>	35.4 m s <sup>-1</sup> from t = 59 to t = 168
E07	24.5 m s <sup>-1</sup> from t = 92 to t = 168
E08	15.9 m s <sup>-1</sup> from t = 125 to t = 168

5.28 shows a time-radius plot of the ensemble-mean, azimuthally-averaged upward vertical velocity ( $\dot{\sigma}$ ) which is averaged between 36 h and 48 h in the experiment sets E01 and E06. The vertical velocity at a radius about 50 km is lower through the troposphere in E06 than in the control experiment E01. The vertical velocity at upper-levels is much weaker in the experiment with the shear flow (Fig. 5.28b). The weaker ascent in E06 reflects the reduced strength of the secondary circulation due to the stabilization by the enhanced warm anomaly aloft.

The time-series of the azimuthally-averaged total wind maximum (Fig. 5.27) show that the

ensemble spread in intensity arises during the intensification phase as in other ensemble experiments in the previous sections. The largest fluctuation amongst ensemble members is about  $30 \text{ m s}^{-1}$  at 72 h, which is larger than that in the control experiment. The significant ensemble spread shows that vortex intensification is highly sensitive to the moisture perturbation in the calculations with the upper-level shear flow. However, the ensemble spread in intensity diminishes during the mature stage, indicating that the mature cyclone is only weakly sensitive to the moisture perturbation.

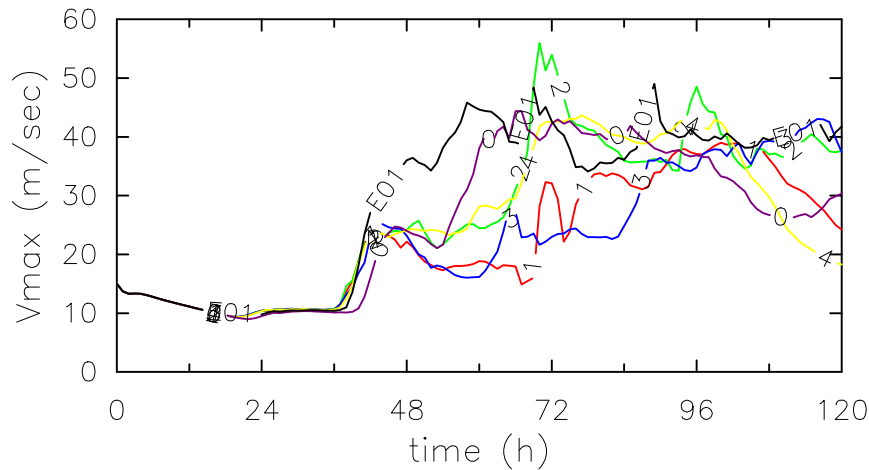


Figure 5.27: Time-series of azimuthally-averaged wind speed maximum ( $V_{max}$ ) at  $\sigma = 0.95$  in the calculations E06<sub>0,1,2,3,4</sub> and E01<sub>0</sub>. The time-series of wind speed maximum in E01<sub>0</sub> is denoted by E01.

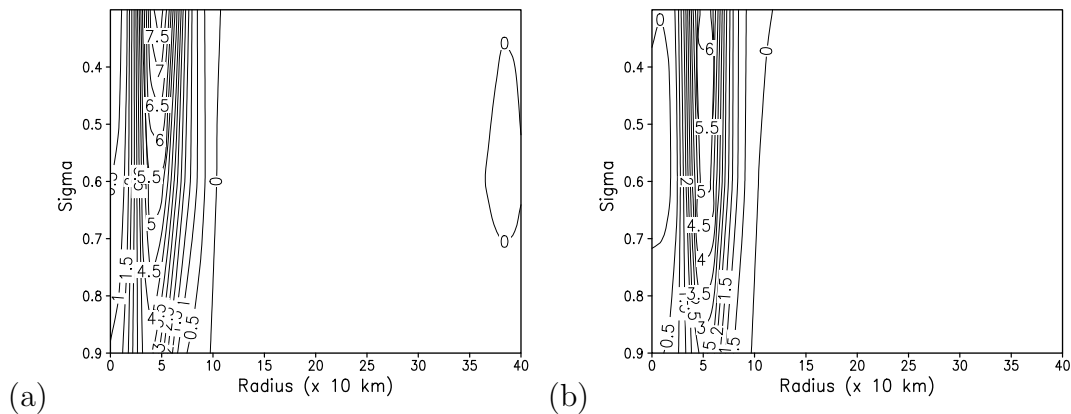


Figure 5.28: Height-radius plot of the ensemble-mean, azimuthally-averaged upward vertical velocity ( $\dot{\sigma}$ ), which is averaged between 36 h and 48 h in the experiment sets: (a) E01 and (b) E06. Only the magnitude of ascent is plotted. The contour interval is  $1 \times 10^{-5} \text{ s}^{-1}$ .

Figure 5.29 compares time-series of the upper and lower bounds of the azimuthally-averaged total wind speed maximum in the ensemble experiment sets E06 and E01. The area surrounded by the two bounds represents a deviation envelope for each experiment. The deviation envelope of E06 remains small and overlaps that of E01 during the gestation period. However, it bears little resemblance to that in E01 between 60 and 72 h and its width

is found to be three times as large, indicating that the predictability of vortex intensity is lower in the calculations with the upper-level shear flow. The deviation envelope in E06 overlaps that in E01 between 72 h and 96 h, which shows that the intensity of mature cyclone in E06 is more predictable than during the period of intensification. However, the width of the envelope in E06 enlarges and does not overlap that of E01 after about 108 h, since the vortices in three ensemble members E04<sub>0,1,4</sub> decay, while those in other members maintain a quasi-steady intensity. The enlarged deviation envelope at the later integration time highlights the lack of predictability of vortex intensity in a single deterministic calculation.

Time-series of the ensemble-mean of the azimuthally-averaged total wind speed maximum in experiments E01-E06 show vortex evolution in each experiment (Fig. 5.30). The vortex intensifies at a reduced rate in experiment sets E02, E04, E05 and E06, compared with the intensification rate in E01. The rate is lowest in the experiment set E02, implying that the reduction of secondary circulation due to the strong radiative cooling is most significant among those experiment sets.

During the intensification phase, there is significant spread in ensemble intensity in Figure 5.30. This spread indicates that the vortex intensification is highly variable, depending on the cooling rate, the humidity in the middle-troposphere, and on an upper-level anticyclonic shear flow. On the other hand, the spread in ensemble intensity diminishes during the mature stage. The intensity of a mature cyclone is less variable and less sensitive to these factors than during the period of intensification.

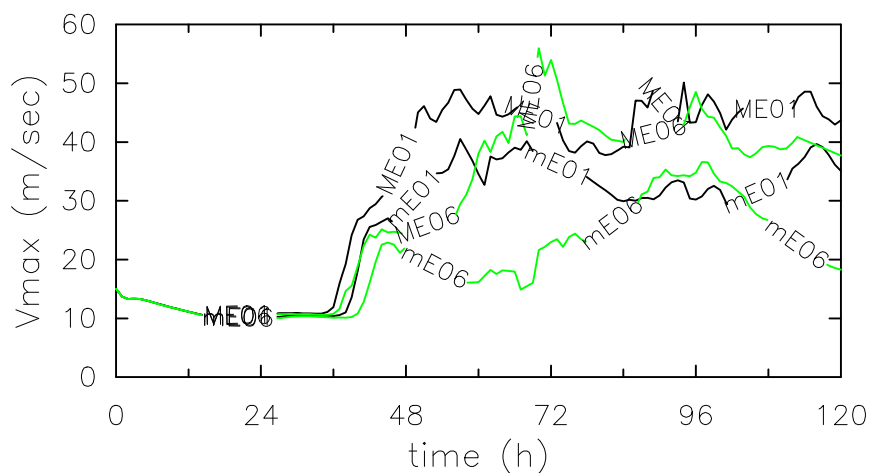


Figure 5.29: Time-series of the upper bounds (ME01, ME06) and lower (mE01, mE06) bounds of  $V_{max}$  at  $\sigma = 0.95$  in experiments E01 and E06.

Table 5.3 compares the ensemble-mean, azimuthally-averaged total wind speed maximum between 72 and 120 h in the experiment sets E01- E06. The mean intensity is  $39.9 \text{ m s}^{-1}$  in E01, while it is only  $29.6 \text{ m s}^{-1}$  in E06. The standard deviation of the intensity in the ensemble integrations of E06 is large ( $8.7 \text{ m s}^{-1}$ ) so that there is significant uncertainty in deciding whether the mature intensity is affected by the weak upper-level anticyclonic shear flow in E06 or not. The large deviation is associated with the fact that the vortices decay in some ensemble members of E06, while they maintain a quasi-steady intensity in

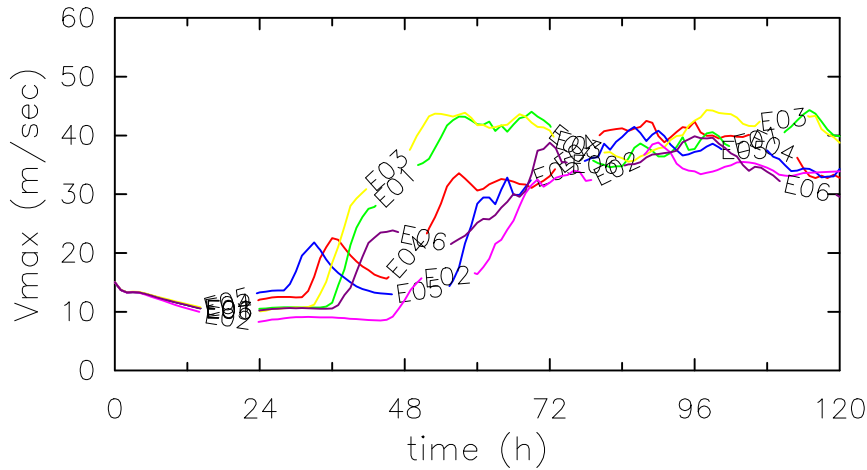


Figure 5.30: Time-series of the ensemble means of  $V_{max}$  at  $\sigma = 0.95$  in the experiment sets E01-E06.

other members. This situation is similar to that in the ensemble integrations of E04, in which the standard deviation is also high ( $\pm 8.9 \text{ m s}^{-1}$ ) due to the ensemble spread in intensity that develops at the later integration time. The significant uncertainty in vortex intensity calls for caution in the interpretation of results for a single calculation.

Table 5.3: A summary of results from the ensemble experiments.

Experiment	Averaged wind speed maximum	standard deviation
E01	$39.9 \text{ m s}^{-1}$	$\pm 4.9 \text{ m s}^{-1}$
E02	$33.9 \text{ m s}^{-1}$	$\pm 6.9 \text{ m s}^{-1}$
E03	$38.8 \text{ m s}^{-1}$	$\pm 5.3 \text{ m s}^{-1}$
E04	$32.8 \text{ m s}^{-1}$	$\pm 8.9 \text{ m s}^{-1}$
E05	$34.3 \text{ m s}^{-1}$	$\pm 5.8 \text{ m s}^{-1}$
E06	$29.6 \text{ m s}^{-1}$	$\pm 8.7 \text{ m s}^{-1}$

## 5.5 Summary

In this chapter, I investigated the effects of strong radiative cooling, low middle-tropospheric humidity, and the presence of an upper-level, anticyclonic, shear flow on the evolution of vortex intensity. Ensemble calculations were carried out to identify also robust features of the vortex intensification in each experiment set. Another point of interest is the predictability of the vortex intensity.

Strong radiative cooling in section 5.2 weakens warm core leading to a reduction in the strength of secondary circulation. The reduction is shown by the weaker ascent and of radial flow than in the calculation without the radiative cooling. Accordingly, the onset of grid-scale saturation and the formation of the meso-vortices are delayed. The results for

the ensemble calculations show that the vortex intensification at a reduced rate due to the strong cooling is a robust feature.

The onset of rapid intensification is delayed in the calculations with the low middle-tropospheric humidity in section 5.3. The dry middle-tropospheric air subsides and enters into the boundary layer, decreasing the mixing ratio in that layer. The air of the reduced mixing ratio is advected inwards along with the radial inflow, decreasing the boundary-layer mixing ratio in the region of ascent. Subsequently, the buoyancy of air parcels in deep clouds and thereby the strength of the secondary circulation are reduced. The decrease of the boundary-layer mixing ratio in the region of ascent and the reduced strength of the secondary circulation are robust features since they survive the ensemble-average.

The presence of an upper-level, anticyclonic, horizontal shear flow leads to an enhancement of the warm anomaly aloft, which reduces convective instability and weakens the secondary circulation. Although the onset time of grid-scale saturation is the same as in the control experiment, the vortex intensifies at a reduced rate due to the weakening of the secondary circulation. The rate of vortex intensification and the radial gradient of buoyancy decrease with the increasing strength of the shear. The delayed onset of rapid intensification is found also in the ensemble-mean of the experiment with a weak anticyclonic shear flow.

The ensemble spread in intensity arises during the intensification phase in all experiments and the spread is larger than in the control experiment. The larger ensemble spread represents a lower predictability of vortex intensity when the rate of radiative cooling is enhanced, the humidity of the middle-troposphere decreases, and when an upper-level, anticyclonic, horizontal shear flow is present. However, the intensity of the mature cyclone is more predictable since the ensemble spread in intensity diminishes during the mature stage. The intensity of the mature cyclone is only weakly sensitive to the moisture perturbation in all ensemble experiments. However, the vortex decays close to the end of integration in some ensemble calculations, while it maintains a quasi-steady intensity in other members. This ensemble spread indicates the significant uncertainty in vortex intensity in a single integration. Only those features that survive in the ensemble-average may be regarded as robust. The results of this idealized study have important implications for intensity forecasts. They highlight the deficiencies in deterministic forecasts of intensity and point to the need for ensemble forecasts.



# Chapter 6

## Summary and conclusions

The initial focus of my study was an observational study of the influence of an approaching upper-level trough on deep convection. The convective instability was measured by the Convective Available Potential Energy (CAPE), which was hypothesized to increase with the approach of the trough in theoretical study. The observational studies used data from the European Centre for Medium-Range Weather Forecasts (ECMWF). In the case of the Burdekin thunderstorm system (2001) that developed in northeastern Australia, it was shown that the CAPE in pre-storm environment was influenced by the cooling that accompanied the trough. However, convective destabilization by the approach of the trough is found to be minimal in the cases of Tropical Cyclones Theodore and Rewa. The difference between the thunderstorm and the cyclone cases is that the cooling associated with the approaching trough is weaker in the cyclone environments than in the thunderstorm environment.

Motivated by the foregoing results I carried out a series of numerical experiments using a simple three-dimensional model. All experiments aimed to examine the details of the intensification of a tropical-cyclone-like vortex and to investigate the influence of the boundary-layer moisture content on the intensification. Vortex intensification is found to be an intrinsically non-axisymmetric process. Deep convection first occurs near the radius of the maximum wind speed of the initial vortex. At an early stage of development there are four convective cells. These cells have enhanced rotation and I refer to them as meso-vortices. The boundary-layer moisture content (and thereby CAPE) is large in the region where these meso-vortices form. The meso-vortices merge to form a monopole of intense vorticity, which is accompanied by the contraction of the radius of the maximum wind. I carried out ensemble calculations by adding random perturbations to the initial boundary-layer moisture field to examine the sensitivity of vortex intensification to the moisture perturbation. The magnitude of the perturbation is below the accuracy with which moisture is normally measured in observations. The formation and subsequent merger of the meso-vortices are sensitive to the moisture perturbation, but the intensity of the mature cyclone is only weakly sensitive. I placed a cap on the wind speed in the surface flux terms to examine the role of the wind-evaporation feedback mechanism in the intensification of the vortex in three-dimensions. The suppressed surface fluxes reduce the

rate-of-increase of the boundary-layer mixing ratio so that the onset time of rapid intensification is prolonged. However, the incipient vortex manages to intensify into a severe tropical cyclone despite the significant reduction of the surface fluxes.

Vortex intensification is found to be highly sensitive to the rate of radiative cooling, the middle-tropospheric mixing ratio, and to the strength of an upper-level, anticyclonic, shear flow. The onset of grid-scale saturation and further intensification are delayed due to the strong radiative cooling that leads to the reduction of the secondary circulation. The dry middle-tropospheric air subsides and enters into the boundary layer, decreasing the mixing ratio in the layer. The dry air is advected inwards to decrease the boundary-layer mixing ratio in the region of ascent. Subsequently, the buoyancy of air parcels in deep clouds is reduced and thereby the vortex intensifies at a reduced rate. An upper-level anticyclonic shear flow enhances the warm anomaly aloft that stabilizes the atmosphere and reduces the strength of the secondary circulation. Accordingly, the onset time of rapid intensification is prolonged as the strength of the shear increases. These features survive in the ensemble average in each experiment and may be regarded as robust. The ensemble spread in intensity during the intensification phase is larger in these sets of ensemble experiment than in the control experiment. The larger ensemble spread shows that the vortex intensity is less predictable. The significant ensemble spread is an indication of the limitations of inferring difference in vortex behaviour from a comparison of two single deterministic calculations. The results for the ensemble integrations point out the uncertainties in vortex intensity of individual ensemble member, but also provide a measure of the degree of predictability of vortex intensification.

My results indicate that an ensemble approach is necessary for improving the skill of intensity forecasts. Future work should consider in more detail the design of ensembles to take account of a different range of perturbations including initial conditions and physical-parametrization uncertainties in numerical models, and an optimal number of ensemble members.

# Appendix A

## The ECMWF model and ERA-40

The description is based on the report of ERA-40 project by Kållberg *et al.* (2004) and the user guide to ECMWF forecast products by Persson (2003).

ERA-40 is a global re-analyses of meteorological observations to describe the state of the atmosphere and information of land and ocean conditions between September 1957 to August 2002. The re-analysis is produced by the ECMWF in collaboration with many institutions with the goal of producing the best possible set of analyses, given observing systems and available computational sources (Uppala *et al.* 2005). The observing system changed over that re-analysis period so that data are provided by satellite-borne instruments from the 1970 onwards with supplements by observations from aircraft, ocean-buoys, and other surface platforms, and radiosonde (Fig. A.1). The number of radiosonde ascents has declined since the late 1980s. Each measurement has its own accuracy and distribution. Observations provide an incomplete picture owing to their variable characteristics and irregular distribution in space and time.

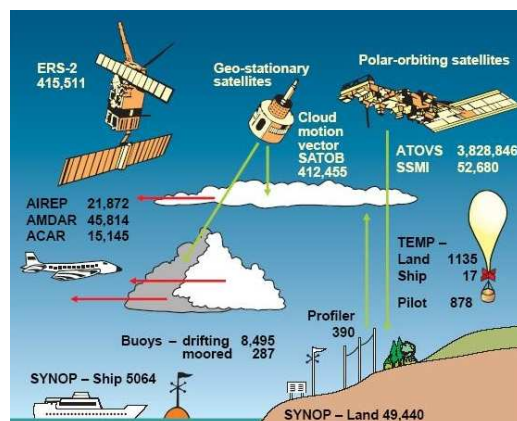


Figure A.1: Data sources for the ECMWF meteorological operating system. Numbers refers to all data items received over a 24 hour period in March 2000 (Image courtesy of ECMWF).

The observations are combined with a short range of forecast which is initiated from the most recent previous analysis to obtain initial conditions with a complete description of the atmospheric state for weather forecasts. This process is so called *data assimilation*. The ERA-40 has 1) four analyses per day, for 00, 06, 12, 18 UTC; 2) two forecasts per day to 6 hours ahead, from 06 and 18 UTC; 3) two forecasts per day to 36 hours ahead, from 00 and 12 UTC. Forecasted data have been archived at 3- and 6-hour range from 00, 06, 12 and 18 UTC and also at 9-, 12-, 15-, 18-, 21-, 24-, 30-, and 36-hour range from 00 and 12 UTC.

The present ECMWF model uses a temporal resolution of 15 minutes. The computational time step has to be chosen with care in order to avoid numerical instabilities and to ensure enough accuracy. The atmosphere is divided into 60 layers up to 0.1 hPa with vertical resolution highest in the planetary boundary-layer in the troposphere and lowest in the stratosphere and lower mesosphere. The vertical coordinate in the model is defined to be proportional to pressure normalized by the surface pressure, whose levels follow the earth's surface in lower and mid-troposphere. This type of vertical coordinate is called a  $\sigma$ -coordinate (Fig. A.2). However, the vertical levels are surfaces of constant pressure in the upper stratosphere and mesosphere. The  $\sigma$  model-level fields are interpolated to 23 pressure-levels. Model "half-level" pressures  $p_{k-\frac{1}{2}}$  are defined by,

$$p_{k-\frac{1}{2}} = A_{k-\frac{1}{2}} + B_{k-\frac{1}{2}}p_s, \quad (\text{A.1})$$

where  $p_s$  is surface pressure and  $k=1,2,3,\dots,61$ .  $A_{k-\frac{1}{2}}$  and  $B_{k-\frac{1}{2}}$  are constants which are recorded in the grid description section of GRIB (Gridded record information block) file for model-level data. The "full-level" pressures  $p_k$  are defined by,

$$p_k = \frac{1}{2}(p_{k-\frac{1}{2}} + p_{k+\frac{1}{2}}). \quad (\text{A.2})$$

Fields on the model  $\sigma$ -levels have also been interpolated to 15 isentropic surfaces, from 265 K to 850 K.

For the horizontal resolution the ECMWF model uses two different numerical representation: 1) T159 spectral resolution, 2) *Gaussian grid point* resolution. The spectral resolution is based on a spherical harmonic expansion, truncated at total wave number 159, for the representation of upper air fields and the computation of the horizontal derivatives. For the representation at the surface and for the model physics a grid point system is necessary instead of a spectral resolution. A latitude-longitude grid point system is not adequate, since the east-west distance between the grid points decreases rapidly with increasing latitude. With this grid point system numerical instabilities near the poles occur. This problem is alleviated in a so-called Gaussian grid point system. In this system, the east-west distance between the grid points decreases poleward so that the grid spacing along a particular latitude is uniform. The Gaussian resolution is symmetric about the equator, with a north-south separation which is close to uniform in latitude with a spacing about a 1.125°. There are 80 grid points aligned along the Greenwich Meridian from equator to pole. The model data archived on the spectral grid or the Gaussian grid points can be also interpolated to a particular latitude-longitude grid points with regular spacing.

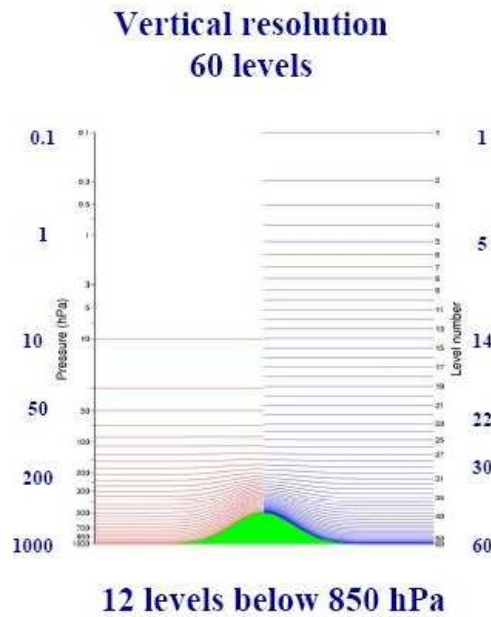


Figure A.2: Vertical resolution of the ECMWF model (Image courtesy of ECMWF).

A *semi-Lagrangian* scheme is used for the numerical formulation in the ECMWF model. A Lagrangian formulation, for example, in a one-dimensional space is,

$$\frac{dQ}{dt} = \frac{\partial Q}{\partial t} + U \frac{\partial Q}{\partial x} = 0. \quad (\text{A.3})$$

For a given parcel,  $Q$  is conserved in the Lagrangian way. A Lagrangian formulation has the advantage of smaller temporal resolution to save computer time than an Eulerian formulation where the local changes in  $Q$  are due to the advection of  $Q$  by the wind  $U$ . However, shear and stretching deformations tend to concentrate parcels inhomogeneously so that it is difficult to maintain uniform resolution in a pure Lagrangian scheme. The *semi-Lagrangian* scheme of the ECMWF model is introduced to maintain uniform resolution by following a marked fluid parcel. At each time step the scheme computes a backward trajectories from every grid point. A position where the air parcel arrived during the time step is the position where the parcel was at the beginning of the time step. The interpolated value of the variable in that position is then carried forward to the grid point, applying physical processes.

The different time scales and feed-back mechanism between various physical processes make the computations in the model extremely complex (Fig. A.3). Physical processes related to small-scale disturbances in space and time, smaller than the scales explicitly resolved by the ECMWF model are computed by parametrization that is formulated in terms of known grid scale variables. The physical processes treated by parametrization in the ECMWF model are radiation, turbulent diffusion, orographic drag, convection, cloud, surface exchanges.

In the ECMWF model, the influence of subgrid-scale orography on the momentum of the atmosphere is represented by a combination of lower-troposphere drag created by the orography and vertical profiles of drag due to the absorption and/or reflection of vertically propagating gravity waves generated by stably stratified flow over the orography (Lott and Miller 1996). This scheme allows a realistic representation of the orographic drag.

The surface exchanges of momentum, heat and moisture are critically important to the whole atmosphere-earth system. The ECMWF model estimates the surface exchanges with the larger scale variables such as wind, temperature and specific humidity by assuming that the transports are proportional to the vertical gradients. Even with the fairly high vertical resolution near the surface, the vertical gradients of temperature, wind, moisture are difficult to describe accurately in a model.

The radiation scheme is designed to take the consideration of the cloud-radiation interactions (Persson 1995), since the interaction is important in long and short term processes. About 15 percent of the overall computational time is used for the radiation scheme.

The cloud scheme in the model is to provide input to the radiation computations and for the calculation of precipitation. The clouds are generated by large-scale ascent, cumulus convection, boundary-layer turbulence and radiative cooling. They are dissipated through evaporation due to large-scale descent, cumulus-induced subsidence, radiative heating and turbulence at both cloud tops and sides, and precipitation processes. Thus, in the cloud scheme the cloud processes are strongly coupled to other parameterized processes.

The convective scheme coupled with the cloud scheme computes the cloud amount and cloud water/ice, convective precipitation, vertical transports of moisture, vertical momentum fluxes, and temperature changes in the atmosphere due to release of latent heat through condensation or cooling in connection with evaporation. Sub-grid vertical fluxes of mass, heat, water vapour and momentum are computed at each model-level with a mass flux scheme interacting with its environment. Deep convection occurs in the model if there is a deep layer of conditional instability. The downdraft mass flux is then assumed proportional to the updraft mass flux. Shallow convection is created in the model if there is moisture supply from surface evaporation in the absence of large scale convergence. No precipitation is produced by the presence of shallow convection in the model. Mid-level convection occurs when convective cells originate at levels above the boundary layer. Evaporation processes describe large-scale and cumulus-induced subsidence and radiative heating evaporation at the cloud sides due to turbulent processes and turbulent motion at the cloud tops.

Production of the ERA-40 re-analysis was monitored both by ECMWF and collaborative institutions. This has enabled some problems to be detected and corrected. Uppala *et al.* (2005) noted that the ERA-40 provides better products, in most respects, than those from the first generation 15-year ECMWF re-analysis (ERA-15) and the National Centers for Environmental Prediction/National Center for Atmospheric Research (NCEP/NCAR) re-analysis.

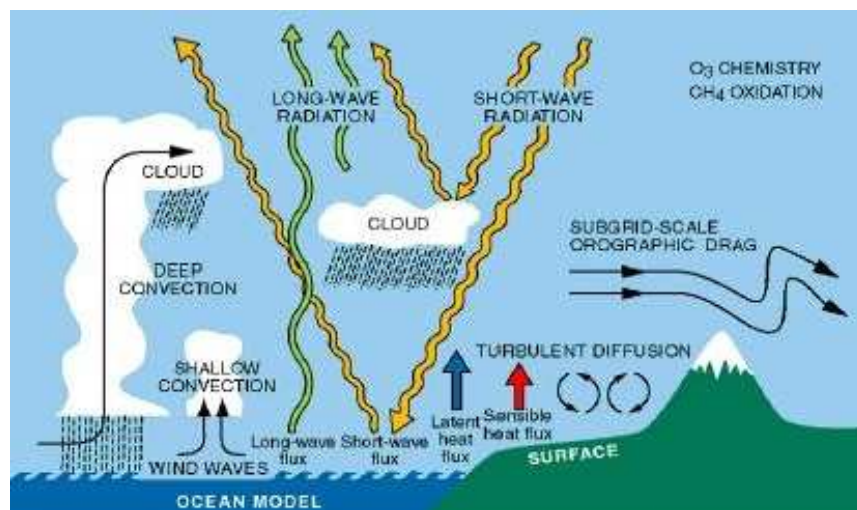


Figure A.3: Physical processes contained in the ECMWF model (Image courtesy of ECMWF).



# Appendix B

## The minimal 3-D tropical cyclone model

The model is three-dimensional hydrostatic model with primitive equations in sigma-coordinates  $(x, y, \sigma)$ , where  $x$  and  $y$  are in the zonal and meridional directions, respectively. The vertical coordinate,  $\sigma$  is defined by

$$\sigma = \frac{p - p_{top}}{p_s - p_{top}} = \frac{p - p_{top}}{p^*}, \quad (\text{B.1})$$

where  $p^* = p_s - p_{top}$ ,  $p_s$  and  $p_{top}$  are pressures at the surface and top of the model, respectively. The following descriptions of the model are based on the study by Zhu *et al.* (2001) and Zhu and Smith (2003).

### Governing equations

The momentum equations in the x- and y- directions are

$$\begin{aligned} \frac{\partial u}{\partial t} = & - \left( u \frac{\partial u}{\partial x} + v \frac{\partial u}{\partial y} \right) - \dot{\sigma} \frac{\partial u}{\partial \sigma} + fv - \\ & \frac{R\theta\sigma(p^*\sigma + p_{top})^{\kappa-1}}{p_o^\kappa} \frac{\partial p^*}{\partial x} - \frac{\partial \Phi}{\partial x} + D_u, \end{aligned} \quad (\text{B.2})$$

and

$$\frac{\partial v}{\partial t} = - \left( u \frac{\partial v}{\partial x} + v \frac{\partial v}{\partial y} \right) - \dot{\sigma} \frac{\partial v}{\partial \sigma} - f u - \frac{R \theta \sigma (p^* \sigma + p_{top})^{\kappa-1}}{p_o^\kappa} \frac{\partial p^*}{\partial y} - \frac{\partial \Phi}{\partial y} + D_v. \quad (\text{B.3})$$

The hydrostatic equation is

$$\frac{\partial \Phi}{\partial \sigma} = - \frac{R p^* (p^* \sigma + p_{top})^{\kappa-1} p_o^\kappa}{\theta}. \quad (\text{B.4})$$

In the above equations,  $u$  and  $v$  are the velocity components in the x- and y-directions,  $f = f_o + \beta y$  is the Coriolis parameter,  $f_o$  and  $\beta = df/dy$  are constants,  $R$  is the specific gas constant for dry air,  $\kappa = R/c_p$ ,  $c_p$  is the specific heat of dry air,  $\theta$  is the potential temperature,  $\Phi$  is the geopotential,  $D_u$  and  $D_v$  represent the frictional drag in the x- and y- directions, respectively and  $p_o = 1000$  mb.

The surface pressure tendency equation, derived from the continuity equation<sup>1</sup> and boundary conditions is

$$\frac{\partial p^*}{\partial t} = - \int_0^1 \left( \frac{\partial(p^*u)}{\partial x} + \frac{\partial(p^*v)}{\partial y} \right) d\sigma \quad (\text{B.5})$$

and  $\dot{\sigma}$  is given by

$$\dot{\sigma} = - \frac{1}{p^*} \int_0^\sigma \left( \frac{\partial(p^*u)}{\partial x} + \frac{\partial(p^*v)}{\partial y} \right) d\sigma + \frac{\sigma}{p^*} \int_0^1 \left( \frac{\partial(p^*u)}{\partial x} + \frac{\partial(p^*v)}{\partial y} \right) d\sigma \quad (\text{B.6})$$

The thermodynamic and moisture equations are

$$\frac{\partial \theta}{\partial t} = - \left( u \frac{\partial \theta}{\partial x} + v \frac{\partial \theta}{\partial y} \right) - \dot{\sigma} \frac{\partial \theta}{\partial \sigma} + Q_\theta \quad (\text{B.7})$$

and

$$\frac{\partial q}{\partial t} = - \left( u \frac{\partial q}{\partial x} + v \frac{\partial q}{\partial y} \right) - \dot{\sigma} \frac{\partial q}{\partial \sigma} + Q_q, \quad (\text{B.8})$$

where  $q$  is the specific humidity,  $Q_\theta$  is the diabatic heat source and  $Q_q$  is the moisture source, the last two of which include contributions from surface fluxes that are described

<sup>1</sup>In  $\sigma$ -coordinates, the continuity equation takes the differential form:  $\frac{\partial p^*}{\partial t} + \frac{\partial(p^*u)}{\partial x} + \frac{\partial(p^*v)}{\partial y} + \frac{\partial(p^*\dot{\sigma})}{\partial \sigma} = 0$

in details in the section of surface turbulent flux terms. The temperature  $T$  is related to  $\theta$  by

$$T = \left(\frac{p}{p_o}\right)^\kappa \theta = \frac{(p^* \sigma + p_{top})^\kappa}{p_o^\kappa} \theta. \quad (\text{B.9})$$

### Surface turbulent flux terms

The turbulent flux of momentum to the sea surface and the fluxes of sensible heat and water vapour at the surface are represented by bulk aerodynamic formulae in the form

$$\begin{aligned} p^*(F_u, F_v) &= -\frac{g\rho^*C_d|\mathbf{v}_4|(u_4, v_4)}{\delta\sigma_4}, \\ p^*F_q &= \frac{g\rho^*C_E|\mathbf{v}_4|(q_{sea}^* - q_{4\frac{1}{2}})}{0.5\delta\sigma_4}, \\ p^*F_{SH} &= \frac{gc_p\rho^*C_E|\mathbf{v}_4|(T_{sea}^* - T_{4\frac{1}{2}})}{0.5\delta\sigma_4}, \end{aligned} \quad (\text{B.10})$$

where the surface wind speed is approximated by the magnitude of the wind vector at level-4,  $\mathbf{v}_4 = (u_4, v_4)$  and  $\delta\sigma_4$ ,  $T_{sea}^*$  and  $q_{sea}^*$  are the sea surface temperature and saturated specific humidity at this temperature, respectively;  $\rho^*$  is the near-surface air density, set to a standard value of  $1.10 \text{ kg m}^{-3}$ . For the CP-grid,  $F_q$  and  $F_{SH}$  are the latent heat and sensible heat fluxes added per unit mass and time at level  $4\frac{1}{2}$ . The exchange coefficient,  $C_E$  is assumed to be the same as  $C_D$ , the surface drag coefficient defined by

$$C_D = (1.024 + 0.05366R_F|\mathbf{u}_b|) \times 10^{-3}, \quad (\text{B.11})$$

where  $R_F = 0.8$  is used to reduce the boundary-layer wind,  $\mathbf{u}_b$  to the 10-m level.

The frictional drag terms  $D_u$  and  $D_v$  in Eqs. (B.2) and (B.3) are obtained by dividing the corresponding terms  $F_u$  and  $F_v$  in Equation (B.10) by the depth  $z_b$  and the density  $\rho_b$  of the lower layer. Similarly the contributions to the source terms  $Q_\theta$  and  $Q_q$  in Eqs. (B.7) and (B.8) from the terms  $F_{SH}$  and  $F_q$  in Eqs. (B.10) are given by the relations:  $Q_\theta = F_{SH}/(\rho_b c_p \pi_s z_b)$  and  $Q_q = F_q/\rho_b z_b$ , where  $\pi_s = (p_s/p_o)^\kappa$  is the Exner function at the surface.

### Boundary and initial conditions

The upper and lower boundary conditions require that  $\dot{\sigma} = 0$  at  $\sigma = 0$  and  $\sigma = 1$ , where  $\dot{\sigma} = D\sigma/Dt$  is the 'vertical'  $\sigma$ -velocity and  $D/Dt$  is the material derivative. The calculations are carried out in a zonal channel with rigid walls at  $y = \pm Y$  and periodic boundary conditions at  $x = \pm X$ . It is assumed that there is no motion normal to the meridional boundaries (i. e.  $v = 0$  at  $y = \pm Y$ ) and that meridional gradients are zero at these boundaries (i. e.  $\partial(u, \theta, q)/\partial y = 0$  at  $y = \pm Y$ ). Surface pressure and geopotential are initially adjusted geostrophically to satisfy the equation

$$\frac{\sigma}{\rho} \frac{\partial p_s}{\partial y} + \frac{\partial \Phi}{\partial y} = -fu. \quad (\text{B.12})$$

The initial mass and geopotential fields are obtained by solving the inverse balance equation, which takes the form Kurihara and Bender (1980),

$$\nabla^2 \Phi + \nabla \left( \frac{RT\sigma}{p} \nabla p^* \right) = 2J_{u,v} + f\zeta - \beta u, \quad (\text{B.13})$$

where  $J$  is the Jacobian operator. The temperature is obtained from the hydrostatic equation (B.4). At  $\sigma = 1$ , where  $\Phi_s = 0$ , the equation can be written as

$$\nabla (RT_s \nabla \ln p_s) = 2J(u_s, v_s) + f\zeta_s - \beta u_s, \quad (\text{B.14})$$

where the subscript 's' denotes the surface value of the relevant quantity. This equation can be solved for the surface pressure field if the surface temperature is known.

The environment surface pressure is 1015 mb, and the minimum surface pressure at the vortex centre is initially 1008 mb. The sea surface temperature is taken to be 26.3°C, which is nearly equal to the air temperature at the surface.

### Subgrid-scale diffusion

To filter out the energy in high frequency waves, a fourth-order horizontal diffusion term  $D_4 = -k_1 \nabla_h^4 \chi$  is added to all prognostic equations with a diffusion coefficient  $k_1 = 0.001 \Delta^4$ , where  $\nabla_h$  is the horizontal Laplacian operator and  $\Delta$  is the horizontal grid spacing. At the boundaries, a second-order diffusion term  $D_2 = k_2 \nabla_h^2 \chi$  is applied with  $k_2 = 0.001 \Delta^2$ . The values of  $k_1$  and  $k_2$  is slightly increased from those used in Zhu *et al.* (2001) in consideration of the increased horizontal resolution, since the higher resolution evokes stronger high energy waves.

# Appendix C

## List of Acronyms

<b>CAPE</b>	Convective available potential energy
<b>CIN</b>	Convective inhibition
<b>ECMWF</b>	European Centre for Medium-Range Weather Forecasts
<b>ERA40</b>	ECMWF re-analysis data for 40 years
<b>GMS</b>	Geostationary meteorological satellite
<b>GMT</b>	Greenwich mean time
<b>LCL</b>	Lifted condensation level
<b>LFC</b>	Level of free convection
<b>LNB</b>	Level of neutral buoyancy
<b>MCVs</b>	Meso-scale convective vortices
<b>PV</b>	Potential vorticity
<b>PVU</b>	Potential vorticity unit ( $1.0 \times 10^{-6} \text{ s}^{-1}$ )
<b>SST</b>	Sea surface temperature
<b>UTC</b>	Universal time coordinates = GMT
<b>WISHE</b>	Wind-induced surface heat exchange



# Bibliography

- Anthes, R. D., 1972: Development of asymmetries in a three-dimensional numerical model of the tropical cyclone. *Mon. Wea. Rev.*, **100**, 461-467.
- Bolton, D., 1980: The computation of equivalent potential temperature. *Mon. Wea. Rev.*, **108**, 1046-1053.
- Bluestein, H. B., 1993: Synoptic-dynamic meteorology in midlatitudes. volume II. Observations and theory of weather systems. Oxford University Press, New York, 594 pp.
- Bluestein, H. B., and M. L. Jain, 1985: Formation of mesoscale lines of precipitation: Severe squall lines in Oklahoma during the spring. *J. Atmos. Sci.*, **42**, 1711-1732.
- Bracken W. E., and L. F. Bosart, 2000: The role of synoptic-scale flow during tropical cyclogenesis over the north Atlantic ocean. *Mon. Wea. Rev.*, **128**, 353-376.
- Colby, F. P., 1984: Convective inhibition as a predictor of convection during AVE-SESAME II. *Mon. Wea. Rev.*, **112**, 2239-2252.
- Colón, J. A., and W. R. Nightingale, 1963: Development of tropical cyclones in relation to circulation patterns at the 200 mb level. *Mon. Wea. Rev.*, **91**, 329-336.
- Davidson, N. E., G. J. Holland, J. L. McBride, and T.D. Keenan, 1990: On the formation of AMEX tropical cyclones Irma and Jason. *Mon. Wea. Rev.*, **118**, 1181-1200.
- DeMaria M. and J. Kaplan, 1999: An updated Statistical Hurricane Intensity Prediction Scheme (SHIPS) for the Atlantic and eastern North Pacific basins. *Wea. Forecasting.*, **14**, 326-337.
- Emanuel, K. A., 1989: The finite-amplitude nature of tropical cyclogenesis. *J. Atmos. Sci.*, **46**, 3431-3456.
- Emanuel, K. A., 1994: Atmospheric Convection. Oxford University Press, New York, 580 pp.
- Emanuel, K. A., J. D. Neelin, and C. S. Bretherton, 1994: On large-scale circulations in convecting atmospheres. *Q. J. R. Meteorol. Soc.*, **120**, 1111-1143.

- Emanuel, K. A., 1995: The behavior of a simple hurricane model using a convective scheme based on subcloud-layer entropy equilibrium *J. Atmos. Sci.*, **52**, 3960-3968.
- Emanuel, K. A., C. Desautels, C. Holloway, and R. Korty, 2004: Environmental control of tropical cyclone intensity *J. Atmos. Sci.*, **61**, 843-858.
- Emanuel, K. A., 2005: Increasing destructiveness of tropical cyclones over the past 30 years *Nature*, **436**, 686-688.
- Erickson, C. O., 1963: An incipient hurricane near the West African coast. *Mon. Wea. Rev.*, **91**, 61-68.
- Fritsch, J. M., and D. J. Chappell, 1980: Numerical prediction of convectively driven mesoscale pressure systems. Part I: Convective parametrization. *J. Atmos. Sci.*, **37**, 1722-1733.
- P. Kallberg, S. Uppala, A. Hernandez, A. Nomura, and E. Serrano, 2004: ERA description. ECMWF Reanalysis Project Report Series No. 17, 72pp.
- Gregory, D., J.-J. Morcrette, C. Jacob, A. C. M. Beljaars, and T. Stockdale, 2000: Revision of convection, radiation and cloud schemes in the ECMWF integrated forecasting system. *Q. J. R. Meteorol. Soc.*, **126**, 1685-1710.
- Gray, W. M., 1968: Global view of the origin of tropical disturbances and storms. *Mon. Wea. Rev.*, **96**, 669-700.
- Hanley, D., J. Molinari, and D. Keyser, 2001: A composite study of the interactions between tropical cyclones and upper-tropospheric troughs. *Mon. Wea. Rev.*, **129**, 2570-2584.
- Hanstrum, B. N., P. W. Bate, and K. J. Smith, 1996: The South Pacific and southeast Indian Ocean tropical cyclone season 1993-94. *Aust. Meteor. Mag.*, **45**, 137-147.
- Hendricks, E. A., M. T. Montgomery, and C. A. Davis, 2004: The role of "vortical" hot towers in the formation of Tropical Cyclone Diana (1984). *J. Atmos. Sci.*, **61**, 1209-1232.
- Hoskins, B. J., M. E. McIntyre, and A. W. Robertson, 1985: On the use and significance of isentropic potential vorticity maps. *Q. J. R. Meteorol. Soc.*, **111**, 877-946.
- Jordan, C. L., 1957: Mean soundings for the West Indies area. *J. Meteor.*, **15**, 91-97.
- Jones, S. C., 2004: On the ability of dry tropical-cyclone-like vortices to withstand vertical shear. *J. Atm. Sci.*, **61**, 114-119.
- Jukes, M., and R. K. Smith, 2000: Convective destabilization by upper-level troughs. *Q. J. R. Meteorol. Soc.*, **126**, 111-123.

- Kållberg, P., A. Simmons, S. Uppala, and M. Fuentes, 2004: The ERA-40 Archive. ECMWF Re-analysis Project Report Series No. 17, 35 pp. [Available from ECMWF, Shinfield Park, Reading, RG2 9AX, United Kingdom.].
- Knaff, J. A., and R. M. Zehr, 2001: Reexamination of tropical cyclone wind-pressure relationships. *Wea. forecasting.*, **22**, 71-88.
- Lott, F., and M. J. Miller, 1996: A new subgrid-scale orographic drag parametrization: Its formulation and testing. *Q. J. R. Meteorol. Soc.*, **123**, 101-127.
- Kossin, J. P., and W. H. Schubert, 2001: Mesovortices, polygonal flow patterns, and rapid pressure falls in hurricane-like vortices. *J. Atmos. Sci.*, **58**, 2196-2209.
- Mapes, B. E., and P. Zuidema, 1996: Radiative-dynamical consequences of dry tongues in the tropical troposphere. *J. Atmos. Sci.*, **53**, 620-628.
- Mapes, B. E., and R. A. Houze, 1992a: An integrated view of the 1987 Australian monsoon and its mesoscale systems. I: Horizontal structure. *Q. J. R. Meteorol. Soc.*, **118**, 927-963.
- Mapes, B. E., and R. A. Houze, 1992b: An integrated view of the 1987 Australian monsoon and its mesoscale systems. II: Vertical structure. *Q. J. R. Meteorol. Soc.*, **119**, 733-754.
- Merrill, R. T., 1988: Environmental influences on hurricane intensification. *J. Atmos. Sci.*, **45**, 1678-1687.
- Molinari, J., and D. Volaro, 1989: External influences on hurricane intensity. Part I: Outflow layer eddy angular momentum fluxes. *J. Atmos. Sci.*, **46**, 1093-1105.
- Molinari, J., S. Skubis, and D. Volaro, 1995: External influences on hurricane intensity. Part III: Potential vorticity structure. *J. Atmos. Sci.*, **52**, 3593-3606.
- Montgomery, M. T., and B. F. Farrell, 1993: Tropical cyclone formation. *J. Atmos. Sci.*, **50**, 285-310.
- Montgomery, M. T., M. E. Nicholls, T. A. Cram, and A. B. Saunders, 2006: A vortical hot towers route to tropical cyclogenesis. *J. Atmos. Sci.*, **63**, 355-386.
- Ooyama, K. V., 1969: Numerical simulation of the life cycle of tropical cyclones. *J. Atmos. Sci.*, **26**, 3-40.
- Ooyama, K. V., 1982: A theory on parametrization of cumulus convection. *J. Meteor. Soc. Japan*, **49**, 744-756.
- Ooyama, K. V., 1987: Numerical experiments of study and transient jets with a simple model of the hurricane outflow layer. Preprints, *17th Conf. on Hurricanes and Tropical Meteorology*, Miami, FL, Amer. Meteor. Soc., 318-320.

- Parker, D. J., 2002: The response of CAPE and CIN to tropospheric thermal variations. *Q. J. R. Meteorol. Soc.*, **128**, 119-130.
- Persing, J., and M. T. Montgomery, 2005: Is environmental CAPE important in the determination of maximum possible hurricane intensity. *J. Atmos. Sci.*, **62**, 542-550.
- Persing, J., M. T. Montgomery, and R. E. Tuleya, 2002: Environmental interactions in the GFDL hurricane model for Hurricane Opal. *Mon. Wea. Rev.*, **130**, 298-317.
- Persson, A., 2003: User guide to ECMWF forecast products. Meteorological Bulletin M3.2, 123 pp. [Available from ECMWF, Shinfield Park, Reading, Berkshire R92 9AX, United Kingdom.].
- Pfeffer, R. L., and M. Challa, 1981: A numerical study of the role of eddy fluxes of momentum in the development of Atlantic hurricanes. *J. Atmos. Sci.*, **38**, 2393-2398.
- Protat, A., and Y. Lemaître, 2001: Scale Interactions involved in the initiation, structure, and evolution of the 15 December 1992 MCS observed during TOGA COARE. Part I: Synoptic-scale Processes. *Mon. Wea. Rev.*, **129**, 1757-1778.
- Raymond, D. J., C. L. Corrillo and L. L. Cavazos, 1998: Case studies of developing east Pacific easterly waves. *Q. J. R. Meteorol. Soc.*, **124**, 2005-2034.
- Reeder, M. J., and R. K. Smith, 1998: Mesoscale Meteorology. In *Meteorology of the Southern Hemisphere*. (Eds. D. Vincent and D. J. Karoly). American Meteorological Society, Boston, Mass. USA, 201-241.
- Riehl, H., and J. S. Malkus, 1958: On the heat balance in the equatorial trough zone. *Geophysica*, **6**, 503-538.
- Roka, M. J., J.-P. Lafore, C. Piriou, and J.-L. Redelsperger, 2005: Extratropical dry-air intrusions into the westAfrican monsoon midtroposphere: An important factor for the convective activity over the Sahel. *J. Atmos. Sci.*, **62**, 390-407.
- Rotunno, R., and K. A. Emanuel, 1987: An air-sea interaction theory for tropical cyclones. Part II: Evolutionary study using a nonhydrostatic axisymmetric numerical model. *J. Atmos. Sci.*, **44**, 542-561.
- Sadler, J. C., 1976: A role of the tropical upper tropospheric trough in early season typhoon development. *Mon. Wea. Rev.*, **104**, 1266-1278.
- Shapiro, L. J., and H. E. Willoughby, 1982: The response of balanced hurricanes to local sources of heat and momentum. *J. Atmos. Sci.*, **39**, 378-394.
- Shapiro, L. J., and J. D. Möller, 2003: Influence of atmospheric asymmetries on the intensification of Hurricane Opal: Piecewise PV inversion diagnosis of a GFDL model forecast. *Mon. Wea. Rev.*, **131**, 1637-1649.

- Shin, S. E., R. K. Smith and J. Callaghan, 2005: Severe Thunderstorms over northeastern Queensland on 19 January 2001: The influence of an upper-level trough on the convective destabilization of the atmosphere. *Aust. Meteo. Mag.*, **54**, 333-346.
- Simpson, R. H., and H. Riehl, 1981: *The Hurricane and Its Impact*. Louisiana State University Press, 398 pp.
- Smith, G. B., II, and M. T. Montgomery 1995: Vortex axisymmetrization: Dependence on azimuthal wave-number or asymmetric radial structure changes. *Q. J. R. Meteorol. Soc.*, **121**, 1615-1650.
- Smith, R. K., 1980: Tropical cyclone eye dynamics. *J. Atmos. Sci.*, **37**, 1227-1232.
- Smith, R. K., 2006: Accurate determination of a balanced axisymmetric vortex. *Tellus*, **58A**, 98-103.
- Smith, R. K., M. T. Montgomery, and H. Zhu, 2005: Buoyancy in tropical cyclone and other rapidly rotating atmospheric vortices. *Dyn. Atmos. Oceans*, **40**, 189-208.
- Smith, R. K. and W. Ulrich, and G. Dietachmayer, 1990: A numerical study of tropical cyclone motion using a barotropic model. Part I. The role of vortex asymmetries. *Q. J. R. Meteorol. Soc.*, **116**, 337-362.
- Spengler, T., M. J. Reeder, and R. K. Smith, 2005: The dynamics of heat lows in simple background flows. *Q. J. R. Meteorol. Soc.*, **131** 3147-3165.
- Steenburgh, W., J. Mass, and F. Clifford, 1996: Interaction of an intense extra-tropical cyclone with coastal orography. *Mon. Wea. Rev.*, **124**, 1329-1352.
- Thorncroft, C. D., B. J. Hoskins and M. E. McIntyre, 1993: Two paradigms of baroclinic-wave life-cycle behaviour. *Q. J. R. Meteorol. Soc.*, **119**, 17-55.
- Waugh D. W., and L. M. Polvani, 2000: Intrusions into the tropical upper troposphere. *Geophys. Res. Lett.*, **27**, 3857-3860.
- Webster P. J., G. J. Holland, J. A. Curry, and H.-R. Chang, 2005: Changes in tropical cyclone number, duration, and intensity in a warm environment. *Science*, **309**, 1844-1846.
- Weckwerth, T. M., 2000: The effect of small-scale moisture variability on thunderstorm initiation *Mon. Wea. Rev.*, **128**, 4017-4030.
- Weisman, M. L., and J. B. Klemp, 1982: The dependence of numerically simulated convective storms on vertical wind shear and buoyancy. *Mon. Wea. Rev.*, **110**, 505-520.
- Weisman, M. L., and J. B. Klemp, 1984: The structure and classification of numerically simulated convective storms in directionally varying wind shears. *Mon. Wea. Rev.*, **112**, 2479-2498.

- Weisman, M. L., and J. B. Klemp, 1986: Characteristics of isolated convective storms. In *Mesoscale Meteorology and Forecasting* (Ed. P. S. Ray), American Meteorological Society, Boston, Mass. USA, 331-358.
- Weisman, M. L., and R. Rotunno, 2004: "A theory for strong, long-lived squall lines" Revisited. *J. Atmos. Sci.*, **61**, 361-382.
- Wilks, D. S., 2006: *Statistical methods in the atmospheric sciences*. Elsevier, Oxford, 627 pp.
- Williams E. R., and N. Renno, 1993: An analysis of the conditional instability of the tropical atmosphere. *Mon. Wea. Rev.*, **121**, 21-36.
- Willoughby, H. E., 1988: The dynamics of the cyclone core. *Aust. Meteo. Mag.*, **36**, 183-191.
- Willoughby, H. E., and P. G Black, 1996: Hurricane Andrew in Florida: Dynamics of a disaster. *Bull. Amer. Meteor. Soc.*, **77**, 543-549.
- Wu, C.-C. and K. A. Emanuel, 1994: On hurricane outflow structure. *J. Atmos. Sci.*, **51**, 1995-2003.
- Xu, K.-M., K. A. Emanuel, 1989: Is the tropical atmosphere conditionally unstable? *Mon. Wea. Rev.*, **117**, 1471-1479.
- Yano, J.-I., and K. Emanuel, 1991: An improved model of the equatorial troposphere and its coupling with the stratosphere. *J. Atmos. Sci.*, **48**, 377-389.
- Yoneyama, K., and D. B. Parsons, 1999: A proposed mechanism for the intrusion of dry air into the tropical western pacific region. *J. Atmos. Sci.*, **56**, 1524-1546.
- Zehr, R. M., 1992: Tropical cyclogenesis in the western North Pacific. NOAA Tech Rep. NESDIS 61, 181pp.
- Zhu, H., R. K. Smith, and W. Ulrich, 2001: A minimal three-dimensional tropical cyclone model. *J. Atmos. Sci.*, **58**, 1924-1944.
- Zhu, H., and R. K. Smith, 2003: Effect of vertical differencing in a minimal hurricane model. *Q. J. R. Meteorol. Soc.*, **129**, 1051-1069.

# Acknowledgements

I am very grateful to Prof. Roger Smith for his advice and kind support during my study in Munich.

Special thanks go to to Dr. Hongyan Zhu for the code used for numerical experiments. I thank Drs. Robert Goaler, Maria Peristeri, Dominique Möller, Lloyd Shapiro, Wolfgang Ulrich, Harry Weber for their helpful suggestions and advice. Dr. Gerald Thomsen and Mr. Sang van Nguyen helped me kindly to solve some technical problems for my research. I appreciate the technical assist from Dipl. Met. Heinz Lösslein and Mr. Hilbert Wendt. Mr. Jeff Callaghan of Australian Bureau of Meteorology provided me useful information and data for the case studies.

Monika Pfeifer, Kathrin Goetzfried, Andreas Pfeiffer, Jan Schween have kindly consulted me for the research and life in Germany.

I thank Prof. Olaf Krüger for his interest in my work. Special thanks go to Prof. Jong-Jin Baik for his encouragement.

I am very grateful to Annelie and Lewis Vogl for their loving kindness. My parents and family have my Best Thanks.

My study in Munich has been supported by Deutscher Akadeischer Austauschdienst (DAAD) and University of Munich. I am grateful also to ECMWF for the data used in the case studies and for the training course I attended in 2003.

## Curriculum Vitae

---



---

<b>Name</b>	Shin, Seol Eun
<b>Address</b>	Meteorological Institute, University of Munich Theresienstr. 37, D-80333 Munich
<b>E-Mail</b>	seol@meteo.physik.uni-muenchen.de

---

### Education

---

<b>Ph.D., 2007</b>	<b>University of Munich</b>
Thesis	Convective instability changes and tropical cyclone intensification
<b>M.S., 2001</b>	<b>Gwangju Institute of Science and Technology (GIST), South Korea</b>
Thesis	The interaction of binary tropical cyclones in the non-divergent barotropic atmosphere
<b>B.S., 1999</b>	<b>Seoul National University, South Korea</b>
Thesis	The relationship of the Northwestern Pacific Ocean Ridge with the severe drought event in the Korean Peninsula in the summer of 1994 and 1995.

---

### Work Experiences

---

<b>Researcher</b>	
2002-2007	University of Munich Tropical cyclone intensification ECMWF data analysis and Numerical modelling
<b>Research assistant</b>	
1999-2001	GIST Tropical cyclone motion and intensification Numerical modelling, Multiple-regression, Neural network
<b>Teaching assistant</b>	
2001	GIST Lecture on the Atmospheric numerical modelling

---

### Training experiences

Numerical Weather Prediction (NWP) course for the diabatic parametrization at ECMWF, Reading, UK, 2003  
Heraeus Summer school of the environmental physics, Bad Honnef, Germany, 2005

### Publications

Shin, S. E., R. K. Smith and J. Callaghan, 2005: Severe Thunderstorms over northeastern Queensland on 19 January 2001: The influence of an upper-level trough on the convective destabilization of the atmosphere. *Aust. Meteo. Mag.*, **54**, 333-346.

Shin, S. E., J.-Y. Han and J.-J. Baik, 2005: On the critical separation distance of binary vortices in a nondivergent barotropic atmosphere. *J. Meteor. Soc. Japan*, **84**, 853-869.

**Awards**

Korean Government Scholarship for GIST students (March 1999 - February 2001)

Deutscher Akademischer Austauschdienst (DAAD) Scholarship (October 2002 - 2006)